600382007

WAKE OF A BLOCK VEHICLE IN A SHEAR-FREE BOUNDARY FLOW

An Experimental and Theoretical Study

by

Robert E. Eskridge
and
Roger S. Thompson

Meteorology and Assessment Division
Environmental Sciences Research Laboratory
U.S. Environmental Protection Agency
Research Triangle Park, NC 27711

ENVIRONMENTAL SCIENCES RESEARCH LABORATORY
OFFICE OF RESEARCH AND DEVELOPMENT
U.S. ENVIRONMENTAL PROTECTION AGENCY
RESEARCH TRIANGLE PARK, NC 27711

DISCLAIMER

This report has been reviewed by the Environmental Sciences Research Laboratory, U.S. Environmental Protection Agency, and approved for publication. Mention of trade names or commercial products does not constitute endorsement or recommendation for use.

AFFILIATION

Robert E. Eskridge is a research meteorologist in the Meteorology and Assessment Division, Environmental Sciences Research Laboratory, U.S. Environmental Protection Agency, Research Triangle Park, North Carolina. He is on assignment from the National Oceanic and Atmospheric Administration, U.S. Department of Commerce.

ABSTRACT

The wake of a moving vehicle was simulated using a specially-constructed wind tunnel with a moving floor. A "block-shaped" model vehicle was fixed in position over the test-section floor while the floor moved at the freestream air speed to produce a uniform, shear-free, approach flow. This simulates an automobile traveling along a straight highway under calm atmospheric conditions.

Vertical and lateral profiles of mean and fluctuating velocities and Reynolds stresses in the wake of the vehicle were obtained using a hot-film anemometer with an X-probe. Profiles were taken at distances of 10 to 80 model heights downwind.

A momentum type wake was observed behind the block-shaped vehicle. The wake does not have a simple self-preserving form. However, it is possible to collapse the velocity deficit with one length and one velocity scale.

Two new theories for the velocity deficit are compared to the theory of Eskridge and Hunt (1979). A theory which considered a height-dependent eddy viscosity was found to fit the data best.

Length and velocity scales were found for the longitudinal variation of the turbulent kinetic energy. The lateral variation is described by a two-dimensional numerical fit of the crosswind variation of the data.

CONTENTS

ABSTRACT iii

FIGURES. vi

TABLES x

SYMBOLS. xi

ACKNOWLEDGEMENTS xv

1. INTRODUCTION. 1

2. SUMMARY AND CONCLUSIONS 5

3. APPARATUS 7

3.1 The wind tunnel. 7
3.2 Velocity measurement 8
3.3 Model vehicles 8
3.4 Empty wind tunnel flow characteristics 9
3.5 Wind tunnel blockage effects and Reynolds number independence 9

4. WAKE THEORY AND MEASUREMENTS OF VEHICLE WAKES 13

4.1 Review of vehicle wake theory 13
4.2 Verification of the theory 15
4.3 Modified wake theory 16
4.4 Height dependent viscosity wake theory 17
4.5 Turbulent kinetic energy terms in the wake 18
4.6 Reynolds stresses in the wake. 22

REFERENCES 24

APPENDIX A Control volume analysis. 26
APPENDIX B Multi-scale wake theory. 37
B.1 Derivation of the multi-scale wake theory 37
B.2 Longitudinal variation of the wake velocity deficit solution. 41
APPENDIX C Height-dependent viscosity wake theory 43
APPENDIX D Simplified height-dependent viscosity wake theory 46

FIGURES

Number		Page
3.1	The wind tunnel	49
3.2	Scale model vehicles	50
3.3	Empty tunnel, mean velocity profiles for four longitudinal positions on centerline	51
3.4	Empty tunnel, mean velocity profiles for three lateral positions at a distance of 1 m from the test section entrance	52
3.5	Empty tunnel, turbulence intensity profiles for three positions at a distance of 1 m from the test section entrance	53
3.6	Locations of pressure measurements for determining blockage effects	54
3.7	Spanwise variation in C_{p_b} for various blockage ratios, A_M/A_T	55
3.8	C_{p_b} as function of Reynolds number for various A_M/A_T	56
3.9	Variation of C_{p_b} with blockage ratio	57
3.10	Vertical profiles of deficit velocity at x/H = 15, y = 0 for 1/8 and 1/32 scale vehicles	58
3.11	Lateral profiles of deficit velocity at x/H = 15, z/H = 0.5 for 1/8 and 1/32 scale vehicles	59
3.12	Vertical profiles of fluctuating velocity component at x/H = 15, y = 0 for 1/8 and 1/32 scale vehicles	60
4.1	Vertical profile of velocity deficit at x/H = 15, y = 0 for 1/8 scale block vehicle and EH theory	61
4.2	Vertical profiles of velocity deficit for 1/32 scale vehicle y = 0	62

Number		Page

4.3 Decay of maximum velocity deficit with downwind distance..... 63

4.4 Rate of growth of the vertical length scale as determined from velocity profiles 64

4.5 Smoke release showing slow growth of the wake 65

4.6 Measured Reynolds stress divided by velocity shear as a function of downwind distance 66

4.7 Theoretical curves and data for vertical profile of velocity deficit for x/H = 30 and y = 0 67

4.8 Theoretical curves and data for lateral profile of velocity deficit for x/H = 30 and z/H = 0.5 68

4.9 Lateral profile of velocity deficit for three longitudinal positions at constant ζ 69

4.10 Theoretical curve and lateral profiles of velocity deficit at constant ζ using similarity coordinates 70

4.11 Theoretical curve and vertical profiles along centerline of velocity deficit using similarity coordinates 71

4.12 Lateral variation of the correlation of the fluctuating velocity component, v' 72

4.13 Length scale determined from fluctuating velocity component v' 73

4.14 Correlation of the fluctuating velocity component in similarity coordinates 74

4.15 Longitudinal variation of the maximum values of the turbulent kinetic energy components $\overline{u'^2}$ and $\overline{v'^2}$ together with least squares linear fit 75

4.16 Cross section of normalized turbulent kinetic energy component $\overline{u'^2}$ with analyzed isolines of the distribution at x/H = 30 76

4.17 Cross section of normalized turbulent kinetic energy component $\overline{v'^2}$ with analyzed isolines of the distribution at x/H = 30 77

Number		Page
4.18	Cross section of normalized turbulent kinetic energy component $\overline{w'^2}$ with analyzed isolines of the distribution at x/H = 30	78
4.19	Cross section of F_c (x,w) with analyzed isolines of the distribution of F_c	79
4.20a	Measured centerline vertical variation of the turbulent kinetic energy component $\overline{u'^2}$ at various downwind distances	80
4.20b	Measured centerline vertical variation of $\overline{u'^2}$ plotted in TKEC similarity variable compared to eq. 4.21 (solid line)	81
4.21a	Measured centerline vertical variation of the turbulent kinetic energy component $\overline{v'^2}$ at various downwind distances	82
4.21b	Measured centerline vertical variation of $\overline{v'^2}$ plotted in TKEC similarity variables compared to eq. 4.21 (solid line)	83
4.22a	Measured centerline vertical variation of the turbulent kinetic energy component $\overline{w'^2}$ at various downwind distances	84
4.22b	Measured centerline vertical variation of $\overline{w'^2}$ plotted in TKEC similarity variables compared to eq. 4.21 (solid line)	85
4.23a	Measured lateral variation of the turbulent kinetic energy $\overline{u'^2}$ at various downwind distances	86
4.23b	Measured lateral variation of $\overline{u'^2}$ plotted in TKEC similarity variables compared to eq. 4.21 (solid line)	87
4.24a	Measured lateral variation of $\overline{v'^2}$ at various downwind distances	88

Number		Page

4.24b	Measured lateral variation of $\overline{w'^2}$ plotted in TKEC similarity variables compared to eq. 4.21 (solid line).....	89
4.25a	Measured centerline vertical variation of $\overline{u'w'}$ at various downwind distances	90
4.25b	Measured centerline vertical variation of $\overline{u'w'}$ in EH similarity coordinates	91
4.25c	Measured centerline vertical variation of $\overline{u'w'}$ in TKEC similarity coordinates	92
4.26a	Measured lateral variation of $\overline{u'w'}$ at various downwind distances	93
4.26b	Measured lateral variation of $\overline{u'w'}$ in EH similarity coordinates	94
A-1	Control volume for determining the couple	95
B-1	Example of cubic spline fit to velocity profile at x/H = 10, y = 0	96
C-1	Example of velocity spectra at x/H = 15. Spike near 20 Hz is due to a vibration from the moving belt	97
C-2	Vertical variation of the eddy viscosity determined from the spectral data with error estimates	98
C-3	Vertical variation of the eddy viscosity determined from the Reynolds stress $\overline{u'w'}$	99

TABLES

Number		Page
1.1	A Summary of Theoretical and Experimental Determinations of Velocity and Turbulence Characteristics of Wakes behind Two and Three-dimensional Objects. . . .	3
3.1	Drag Coefficient as a Function of Blockage	9
4.1	Polynomial Two-dimensional Fit to Turbulent Kinetic Energy Function F_c	20

SYMBOLS

A	-- constant, determined from the couple, giving the strength of the wake
A_M	-- cross-sectional area of model
A_T	-- cross-sectional area of wind tunnel
a_1, a_2, a_3	-- constants in turbulent kinetic energy equation
C	-- couple on the vehicle
C_D	-- drag coefficient
C_{p_b}	-- pressure coefficient on back face of model
D	-- drag on the vehicle
f	-- function giving vertical and lateral variation of velocity deficit
F	-- function describing lateral and vertical variation of turbulent kinetic energy terms in original (EH) theory
F_c	-- function describing cross-sectional variation of turbulent kinetic energy terms
$\vec{F}$	-- force vector
H	-- height of the vehicle
$\tilde{H}(\zeta)$	-- normalized function describing vertical variation of eddy viscosity
$H^*(x,z)$	-- function describing vertical variation of eddy viscosity

$\vec{i}$	-- unit vector in x or x_1 direction
$\vec{j}$	-- unit vector in y or x_2 direction
$\vec{k}$	-- unit vector in z or x_3 direction
$l(x)$	-- vertical scale length of velocity deficit
$l'(x)$	-- vertical scale length of turbulence wake
ℓ_E	-- Eulerian integral length scale
$M(a,b,z)$	-- functional form of a type of power series
$\vec{n}$	-- outward directed unit normal
p	-- perturbation pressure
P_b	-- static pressure measured on rear of vehicle
P_o	-- total pressure
P_{s_r}	-- free-stream static pressure
p_s	-- static pressure measured with pitot tube
$\vec{q}$	-- three-dimensional velocity vector
R_e	-- Reynolds number
s_{ij}	-- fluctuating rate of strain
S_{ij}	-- mean rate of strain
u	-- velocity deficit behind the vehicle defined so that $u \geq 0$
u_{max}	-- maximum velocity deficit
U	-- local mean speed

U_∞	-- free-stream speed
$\overline{u'^2}$	-- x-component of turbulent kinetic energy
$\overline{u'v'}$, $\overline{u'w'}$, etc.	-- Reynolds stresses
v	-- y-component of perturbation velocity
$\overline{v'^2}$	-- y-component of turbulent kinetic energy
W	-- width of the vehicle
w	-- z-component of perturbation velocity
$\overline{w'^2}$	-- z-component of turbulent kinetic energy
(x, y, z)	-- right handed coordinates, with x-axis or x_1-axis directed along axis of the wake
(x_1, x_2, x_3)	
$\bar{x}, \bar{y}, \bar{z}$	-- similarity coordinates used in velocity deficit solution
X_1, X_2, Y_1, Y_2	-- arbitrary points used in control volume analysis
Z_1	
$(\ )_x$	-- indicates partial derivative with respect to x
α, β	-- constants relating the decay in the wake to the growth of the length scale
γ	-- constant in assumed form of eddy viscosity
δ	-- height of boundary layer in wind tunnel
ζ	-- similarity coordinate, $z/l(x)$
η	-- similarity coordinate, $y/l(x)$ or $y/[\lambda W\ Hl(x)]$
λ	-- constant relating transverse eddy viscosity to the vertical eddy viscosity

Λ_1 -- constant in original velocity deficit theory

σ -- standard deviation of velocity deviations

ν -- kinematic viscosity

ν_T -- eddy viscosity

ρ -- density of dry air

τ_{xy} -- shearing stress acting in x direction along a surface normal to the y direction

χ -- similarity coordinate, $\chi = y/[W\ (x/H)^{0.4}]$

$\Psi_{i,j}$ -- constants in polynomial surface fit

ω -- similarity coordinate, $\omega = z/[H\ (x/H)^{0.4}]$

ACKNOWLEDGEMENTS

The work reported in this paper was greatly influenced by the following people; we thank:

Rex Britter for his help in designing the wind tunnel and discussions concerning the results,

Ian P. Castro for his assistance in the tunnel blockage effect and Reynolds-number-independence work,

Julian C.R. Hunt for his suggestions on alternate theoretical approaches to the original theory and for his review of this paper,

Myron Manning for his assistance in constructing and modifying the moving floor wind tunnel used in this study,

Mike Shipman for generating new and modifying existing computer programs for special purposes associated with the collection and reduction of data, and

The remainder of the staff at the Fluid Modeling Facility for their many comments and suggestions.

Their generous assistance is deeply appreciated by the authors of this report.

1. INTRODUCTION

The dispersion of automobile exhaust near highways is of much current interest. Mathematical models are needed that will accurately predict concentration fields. This study on the structure of the wakes of vehicles was undertaken at the U.S. Environmental Protection Agency's Fluid Modeling Facility to provide information to be used in numerical models of automobile exhaust dispersion.

A wind tunnel with a test-section floor that moves at the freestream air speed was constructed to generate a uniform (constant speed with height) approach flow. Scale model vehicles with rotating wheels were held in position in the test section by guys attached to the test-section walls. A vehicle fixed in a uniform flow over a moving floor is aerodynamically equivalent to a vehicle moving down a straight highway through a calm atmosphere.

Automobiles and scale model vehicles have wakes which can be characterized as momentum wakes which contain an organized vortex pair aligned with the axis of the wake. In this paper we are interested in only the momentum wake and therefore generally discuss only those data and theories applicable to momentum wakes. To create a "pure" (no mean swirl) momentum wake, block-shaped vehicles of appropriate heights and widths have been used. It should be noted that momentum wakes contain vortices, but in time-averaging the flow the vortices disappear.

A momentum wake's character is determined mainly by the flow field in which it is embedded. Important cases are: flows which are free of limiting walls, and flows which are influenced by a boundary. Free flows may be subdivided further into shear flows and shear-free flows. In addition, wakes in the flows can be subdivided into laminar and turbulent wakes. The classical results for unbounded laminar wakes are given by Goldstein (1938) and a recent theory has been developed by Hunt (1971) for surface-mounted objects. Hunt showed that the strength of the wake for surface-mounted objects is determined by the couple rather than the drag.

Hunt's work was extended by Counihan et al. (1974) to describe wakes of two-dimensional objects in a turbulent boundary layer. Castro (1979) has shown that this theory is inapplicable when the wake height approaches that of the boundary layer. However, the wakes of very small two-dimensional objects didn't agree with the theory as well as those behind large two-dimensional blocks. Castro stated that it is unlikely that a constant eddy viscosity model will describe the complex flow in this type of wake.

Theories for wakes behind three-dimensional objects in turbulent boundary layers have been developed by Hunt (1971, 1974), Lemberg (1973) and Hansen and Cermak (1975). Eskridge and Hunt (1979), hereafter referred to as EH, have presented a model of a three-dimensional wake near a moving surface (no shear in the approach flow). Experimental investigations of wakes behind three-dimensional bodies have been carried out recently by Lemberg (1973), Hansen and Cermak (1975), Castro and Robins (1977), Robins and Castro (1977), and Woo et al. (1976), among others.

The finding of these studies are summarized in Table 1.1. This table includes only selected recent results. In wake flows constraints on the exponents of the x-dependence of the velocity deficit and length scale can be derived from the equation of motion and from a control volume analysis, if a self-preserving solution is assumed. Control volume analyses similar to the one in Appendix A can be performed for two-dimensional and three-dimensional objects mounted on a surface or in free flow. If we define a and b as the exponents in: $U_{max}(x) \propto x^{-a}$ and $\ell(x) \propto x^{b}$, the control volume analyses will show that a = b for wakes of two-dimensional objects in free flow, a = 2b for wakes of three-dimensional objects in free flow and two-dimensional objects on a surface, and a = 3b for wakes of three-dimensional objects on a surface. The effects of shear have been ignored for the surface flow. An analysis of the equation of motion, similar to that in Appendix B, using an eddy viscosity that varies as x^{-c}, results in c = 1-2b. For a constant eddy viscosity, c is equal to zero, and thus b = 1/2. In this report, the eddy viscosity was assumed to be proportional to the length scale and the maximum velocity deficit, or c = a-b. Most of the entries in Table 1.1 satisfy these constraints with the only glaring exception being the surface-mounted, three-dimensional object study by Smith, et al. (1977).

There is an additional complexity in wake flows not yet mentioned.

TABLE 1.1 A SUMMARY OF THEORETICAL AND EXPERIMENTAL DETERMINATIONS OF VELOCITY AND TURBULENCE CHARACTERISTICS OF WAKES BEHIND TWO-AND THREE-DIMENSIONAL OBJECTS

Investigator or Reference	Description of the Study					Distance Dependence			
	Laminar Wake	Turbulent Wake	Surface Mounted Object fixed floor	Surface Mounted Object moving floor	Shear Flow	Velocity Deficit Decay Rate	Length Scale	Reynolds Stresses Decay Rate	$\overline{u'^2}$, $\overline{v'^2}$, $\overline{w'^2}$ Decay Rate
Two-Dimensional Objects									
Hunt (1971)	X		X		X	x^{-1}	$x^{1/2}$		
Hunt (1980)	X			X		x^{-1}	$x^{1/2}$		
Goldstein (1938)	X					$x^{-1/2}$	$x^{1/2}$		
Counihan et al. (1974)		X	X		X	x^{-1}		$x^{-3/2}$	$x^{-3/2}$
Castro (1979)		X	X		X	$\sim x^{-1}$		$O(x^{-1})$	$O(x^{-1})$
Schlichting (1960)		X				$x^{-1/2}$	$x^{1/2}$		
Counihan (1971)		X	X			x^{-1}	$x^{.4}$		
Arya & Shipman (1979)		X	X		X	x^{-1}	$x^{1/2}$	x^{-1}	x^{-1}
Three-Dimensional Objects									
Smith, et al. (1977)	X		X		X	$x^{-4/3}$	$x^{1/3}$	$x^{-8/3}$	
Hunt (1974), Woo et al		X	X		X	$\sim x^{-3/2}$	$x^{1/2}$		
Hunt (1980)	X			X		$x^{-3/2}$	$x^{1/2}$		
Hinze (1975)		X				$x^{-2/3}$	$x^{1/3}$	$x^{-1/3}$	
Eskridge & Hunt (1979)		X		X		$x^{-3/4}$	$x^{1/4}$		$x^{-3/2}$
Lemberg (1973)		X	X		X	$x^{-1.58}$	$x^{1/2}$		$x^{-.3}$
This study (1981)		X		X		$x^{-3/4}$	$x^{1/4}$	$x^{-3/2}$	$x^{-1.2}$

Townsend (1976) hypothesized that a wake flow becomes self-preserving (i.e., one length and one velocity scale will be adequate to describe the velocity, stresses and higher turbulence moments) because the turbulence attains an equilibrium state which depends only on the type of flow and momentum integral, or, in the present case, the couple.

However, Bevilaqua and Lykoudis (1978) have shown that wake strength depends not only on the drag (momentum integral) but also on the structure of the dominant eddies. The flow behind a block-shaped vehicle will shed vortices into the wake like the sphere Bevilaqua and Lykoudis studied. The resulting "memory" effect implies that in a block vehicle wake the turbulent kinetic energy terms ($\overline{u'^2}$, $\overline{v'^2}$, $\overline{w'^2}$) will not be self-preserving in the Townsend sense.

SECTION 2

SUMMARY AND CONCLUSIONS

An experimental study of the wake of a moving vehicle was made using a specially-constructed wind tunnel with a moving floor. A block-shaped model vehicle was fixed in position over the test-section floor while the floor moved at the freestream air speed to produce a uniform, shear-free, approach flow. This simulates an automobile traveling along a straight highway under calm atmospheric conditions.

Vertical and lateral profiles of mean and fluctuating velocities and Reynolds stresses in the wake of the vehicle were obtained using a hot-film anemomenter with an X-probe. Profiles were taken at distances of 10 to 80 model heights downwind of the vehicle.

A momentum wake was observed for the block-shaped vehicle. The wake does not have a simple self-preserving form. However, it is possible to collapse the velocity deficit with one length growth rate and one velocity scale, and the turbulence with different length growth rate and velocity scales.

The velocity deficit behind the vehicle was found to decay as $(x/h)^{-3/4}$ and the length scale to grow as $(x/h)^{1/4}$, confirming the predictions of EH. However, the turbulent kinetic energy components decay as $(x/h)^{-1.2}$ and the turbulent length scale grows as $(x/h)^{0.4}$ instead of the self preserving solutions of $(x/h)^{-3/2}$ and $(x/h)^{1/4}$ which were predicted.

Velocity deficit solutions are found to the equations of motion for three cases: first, allowing scale-lengths to differ for the lateral and axial directions with constant viscosity (two scale lengths) second, allowing viscosity to vary continuously in the vertical, and finally, a matched solution where viscosity varied linearly near the surface and then was held constant above a given height.

None of the above solutions matched the data in all respects, but the two-scale-length, variable-viscosity solution was the best.

The turbulence decayed longitudinally as $(x/h)^{-1.2}$. To describe the behavior in the lateral and vertical direction a two-dimensional fit of the data was found by least-squares-fit using "orthogonal" polynomials. Appropriate constants were determined from the data which allow a complete description of the wake turbulence.

Numerical models which predict pollutant concentrations along roadways can be enhanced by including the physical properties of wakes found in this study.

SECTION 3

APPARATUS

3.1 WIND TUNNEL

A wind tunnel was constructed especially for this study (Fig 3.1). A commercially available conveyor-belt assembly was used for the test-section floor and supporting framework for the entrance, test and exit sections of the wind tunnel. The test section was 4.75 m long (4.15 m of which was moving floor) with a cross section 0.82 m wide and 0.71 m high.

The entrance section had the same cross-section dimensions as the test section. A bellmouth (diameter of 0.22 m) around the perimeter of the entrance directed room air into a section of Verticel™ (Verticel Co., Englewood Co.: paper triangular-cell honeycomb; cell length = 0.15 m and hydraulic diameter = 0.01 m). Two fiberglas screens (16 x 18 mesh) were placed downwind of the honeycomb to further lower the freestream turbulence.

The moving portion of the test-section floor was the rubber conveyor belt (0.75 m wide). A notched overlapped joint and large end rollers produced a smoothly running belt. Rails along the tops of the walls were installed to support an instrument-traversing mechanism. The longitudinal position of a probe was set manually; vertical and lateral positions were remotely set and read from an operator's desk.

The exit section contained a section of Verticel and a lateral contraction to a 0.71 m wide by 0.71 m high cross section. A cast aluminum fan with three blades (diameter of 0.61 m) was powered by a two-speed (1140/1725 RPM), 250 W electric motor (115 V, 60 Hz). The fan was mounted in a metal "venturi panel" (i.e., shroud) for efficient operation. Baffle plates of different porosities were inserted into a slot just upwind of the fan to fine tune the air speed or to obtain a variety of air speeds for velocity probe calibrations. The maximum air speed, obtained with no baffle plate and the fan motor on high speed, was 4.0 m/s.

The operating speed of the tunnel during all experiments was 1.9 m/s; the turbulence intensity (root mean square of the velocity fluctuation divided by the mean speed) was less than 1%.

In performing additional tests to determine possible Reynolds number effects and the extent of the blockage effects resulting from the size of the models, two additional wind tunnels of a more conventional nature were used: the Fluid Modeling Facility's Meteorological Wind Tunnel (Snyder, 1979), and the Air Pollution Training Wind Tunnel with test sections of 3.7 m wide x 2.1 m high x 38 m long and 1 m wide x 1 m high x 3 m long, respectively.

3.2 VELOCITY MEASUREMENTS

Velocities were measured with Thermo-Systems (St. Paul, Mn.) hot-film anemometers. X-configured probes (model 1243-20) were used to obtain transverse velocity components as well as the streamwise component. The bridge outputs of the anemometers (model 1054-A) were suppressed with signal conditioners (model 1057), attenuated, and sent to the laboratory's Digital Equipment Corporation PDP 11/40 minicomputer. Software in the computer controlled the analog to digital conversion or sampling rate, linearized the signal, and provided real-time displays of results. The probes were calibrated in position on the instrument traversing mechanism against a pitot tube located nearby for determining mean test section velocities obtained with the various baffle plates. The X-probe was oriented to measure either the streamwise and lateral components or the streamwise and vertical components. Calculated values were mean streamwise speed, fluctuating streamwise and transverse components, and the associated Reynolds stress. Most measurements were made at 100 samples per second for 30 seconds. A few ten-minute samples at 500 samples per second were taken at 30 heights downwind of the vehicle at various vertical positions in order to calculate turbulence spectra. From these, an eddy viscosity formulation was derived for use in a theory presented below.

3.3 MODEL VEHICLES

Simple block-shaped models were constructed of wood; they had proportions of height, width and length of a typical automobile (Fig 3.2). Each model

was mounted on a baseplate with wheels and rubber tires. Approximate scale ratios of 1/32 and 1/8 were used.

The 1/32-scale block-shaped vehicle was patterned on the dimensions of an intermediate size American automobile: height = .043 m, width = .055 m, length = .145 m, ground clearance = .009 m, and wheel diameter = .024 m. The 1/8-scale vehicle was four times as large in all respects.

3.4 EMPTY WIND TUNNEL FLOW CHARACTERISTICS

Homogeneity of the mean flow was checked with the tunnel operating at test condition by measuring vertical profiles at various positions in the test section. Fig. 3.3 shows profiles on the centerline for distances of 1, 2, 3 and 4 m from the front of the test section. Fig. 3.4 displays the lateral homogeneity with profiles at a distance of 1 m from the front of the test section at lateral positions of -.205, 0, and .205 m. The air speed was 1.9 ms^{-1}; there was little scatter down to the belt surface.

Vertical profiles of the turbulence intensity at a distance of 1 m from the front of the test section and lateral positions of ±.205 m are shown in Fig. 3.5. The turbulence intensity is seen to be constant and below 1% except very near the belt, where probe sensitivity near the surface is suspect.

3.5 WIND TUNNEL BLOCKAGE EFFECTS AND REYNOLDS NUMBER INDEPENDENCE

In order to determine if the velocity and turbulence profiles for the large vehicle were affected by blockage in the moving-belt tunnel, several tests were performed with both the small and large vehicles. These experiments were performed in the moving belt tunnel and in two other wind tunnels so that various values of the base pressure coefficient,

$$-C_{P_b} = \frac{P_{s_r} - P_b}{\frac{1}{2}\rho U_\infty^2} \tag{3.1}$$

could be determined as a function of Reynolds number and blockage ratio. In (3.1) P_{s_r} is the free-stream static (reference) pressure upwind of the vehicle

(Fig. 3.6), P_b is the static pressure measured on the rear surface, and $1/2\ \rho U_\infty^2$ is the reference dynamic pressure.

Now (3.1) can be written as

$$C_{P_b} = \left(\frac{P_b - P_s}{P_o - P_s} + \frac{P_s - P_{sr}}{P_o - P_s} \right) \frac{P_o - P_s}{P_o - P_{s_r}}$$

or

$$C_{P_b} = \left[(C_{P_b})_{measured} + \frac{P_s - P_{sr}}{P_o - P_s} \right] \frac{P_o - P_s}{P_o - P_{s_r}} \tag{3.2}$$

where P_s is the local static pressure and P_o is the total pressure given by $P_o = 1/2\ \rho U_\infty^2 + P_{s_r}$. The pressure ratios in (3.2) can be easily determined from measurements.

In Fig. 3.7 the spanwise variation in C_p for various blockages is shown. While the pressure is not constant across the rear as one might expect, the variation is small, and is most likely due to asymmetries in the vehicles and the flow not being exactly normal to the front of the vehicles. Since the pressure variations were small, the pressure at the tap at $y/W = -0.25$ was used in all calculations.

In Fig. 3.8 data are presented showing that while $-C_{p_b}$ is a function of blockage ratio it does not appear to be a function of Reynolds number. However, there was considerable scatter in the data.

The pressure coefficient $-C_{p_b}$ is plotted against blockage ratio in Fig. 3.9. For the experiments performed in the non-moving belt tunnels, the vehicles were placed near the tunnel entrance immediately downwind of the contraction. This insured a small floor boundary layer (thickness δ). The boundary layer was, of course, relatively more important for the small vehicle than for the large vehicle. This may be the reason for the sudden change at small blockage ratios which otherwise is not reasonable.

The drag coefficient, C_D, can be estimated by assuming that the normalized integrated pressure coefficient on the front face is $(0.8)^2$, as reported by

Mason and Beebe (1978), to give

$$C_D = (0.8)^2 + (-C_{p_b}). \tag{3.3}$$

Table 3.1 shows the calculated drag coefficient as a function of blockage where A_M and A_T are the cross-sectional areas of the model and wind tunnel, respectively.

TABLE 3.1. DRAG COEFFICIENT AS FUNCTION OF BLOCKAGE

A_M/A_T (% blockage)	C_D
.51	0.775
3.84	0.876
6.50	0.957

We see that the drag coefficient is about 20% greater for the large car in the moving belt tunnel than for the small car in the same tunnel (Table 3.1).

An empirical formula (Castro and Fackrell, 1978) for estimating the blockage effect on drag has the form

$$C_{D_o} = C_D \left(1 - A_M / A_T\right)^m \tag{3.4}$$

where C_{Do} is the observed drag coefficient. For the block vehicle, m was found to be 3.31. For two-dimensional fence flows, Castro and Fackrell found m varied between 2.6 and 7.5 depending on the ratio δ/H_f, where δ and H_f are the height of boundary layer and fence, respectively.

The control volume analysis presented in Appendix A relates the couple,

C, acting on the vehicle to a surface integral of the velocity deficit, u(x,y,z), assuming that an integral of the surface pressure is small. That is:

$$C = \rho \int_0^{\infty} \int_{-\infty}^{\infty} u U z \, dy \, dz . \tag{3.5}$$

A control volume analysis of the conservation of momentum yields a relationship for the drag, D, on the vehicle:

$$D = \rho \int_0^{\infty} \int_{-\infty}^{\infty} u U \, dy \, dz - \int_{-\infty}^{\infty} \int_{-\infty}^{x} \tau_{zx}(x,y,0) \, dx \, dy \tag{3.6}$$

where $\tau_{zx}(x,y,o)$ is a surface shear stress defined in Appendix A.

A centerline vertical profile of u/U and a lateral profile of u/U at z/H = 0.5 are plotted in Figs. 3.10 and 3.11, respectively, for the small and large vehicle at x/H = 15. These two figures imply that the couple computed from (3.5), scaled by vehicle size, would be approximately equal for both vehicles. Similarly, the first term on the right side of (3.6) would be the same for both vehicles. The previously discussed difference in drag coefficients for the two vehicles can be explained as a difference in the integrated surface shear, the second term on the right side of (3.6).

Reynolds-number independence of the vehicle wakes is further supported by a comparison of velocity fluctuations at x/H = 15 shown in Fig. 3.12. Thus, similar wakes exist for the two sizes of vehicles independent of the somewhat larger coefficient of drag found for the large vehicle.

In summary, wind tunnel blockage is not a problem and the wake flows are independent of Reynolds number.

SECTION 4

WAKE THEORY AND MEASUREMENT OF VEHICLE WAKE

4.1 REVIEW OF VEHICLE WAKE THEORY

A car moving at speed U through a calm atmosphere (windspeed <1 ms^{-1}) is equivalent to a car held fixed in space over the roadway with the road and air moving past the car at speed U. The coordinate system used here has its origin at the rear of the vehicle. Several heights downwind of the vehicle, beyond the recirculation region, the velocity deviations (u,v,w << U) from the undisturbed flow are small enough that a perturbation analysis of the equations of motion can be carried out (details are found in EH). The first equation of motion has the following linear form

$$-\rho U \frac{\partial u}{\partial x} = \frac{\partial p}{\partial x} + \frac{\partial \tau_{xz}}{\partial z} + \frac{\partial \tau_{xy}}{\partial y}, \tag{4.1}$$

where it is assumed that

$$\begin{aligned} \tau_{xz}/\rho &= \nu_T(x) \frac{\partial (U-u)}{\partial z} = -\nu_T(x) \frac{\partial u}{\partial z}, \\ \tau_{xy}/\rho &= -\nu_T(x) \frac{\partial u}{\partial y}, \end{aligned} \tag{4.2}$$

and the eddy viscosity can be estimated as

$$\nu_T(x) \propto \ell(x)\, u_{max}(x), \tag{4.3}$$

where $\ell(x)$ is a vertical scale length in the wake and $u_{max}(x)$ is the maximum velocity deficit in the wake.

In this (EH) theory it is implicit that the vertical and lateral length scales are identical. The pressure gradient term in (4.1) can be neglected;

the solution to the resulting equation is

$$u = UA\left(\frac{x}{H}\right)^{-3/4} \zeta \exp\left[-(\zeta^2+\eta^2)/8\right], \tag{4.4}$$

where

$$\begin{aligned} \zeta &= z/\ell(x), \\ \eta &= y/\ell(x), \\ \ell(x) &= \gamma A H\left(\frac{x}{H}\right)^{1/4}, \end{aligned} \tag{4.5}$$

γ and A are constants, and H is the height of the vehicle. The value of A can be estimated by approximating the couple acting on the vehicle by the drag on the vehicle times one half the height of the vehicle. This results in (see EH):

$$A \cong \left[\frac{W C_D}{32\pi e^{1/2} H \gamma^3}\right]^{1/4}. \tag{4.6}$$

The turbulence is estimated by assuming it has a self-preserving form and that the turbulent kinetic energy is proportional to the eddy shear stresses in the wake. This yields the results:

$$(\overline{u'^2}, \overline{v'^2}, \overline{w'^2}) = (a_1, a_2, a_3)\left(\frac{x}{H}\right)^{-3/2} A^2 F(\zeta, \eta), \tag{4.7}$$

where $F(\zeta,\eta) = 0.5e^{3/2}\left[(1-\zeta^2/4)+\zeta^2\eta^2/16\right]^{1/2}\exp\left[-(\zeta^2+\eta^2)/8\right]$

$$\text{for } (\zeta^2+\eta^2) \geq 12 \; ; \; F(\zeta,\eta) = 1 \text{ otherwise.} \tag{4.8}$$

This theory is reasonable for the velocity field except near the surface, where it is clear that a much stronger shear layer exists than is possible with a constant eddy viscosity. Also, the theory does not allow for obstacles that are wider than they are high. Fig. 4.1 shows a centerline velocity profile taken at x/H = 60 compared with the original theory. It is immediately obvious that the wake contains a very strong shear layer near the surface that is incompatible with a constant eddy viscosity in the vertical direction as proposed in (4.3).

4.2 VERIFICATION OF THE EH THEORY

One of the important predictions of the theory in EH is that the velocity deficit and lateral length scale vary as

$$u \propto \left(\frac{x}{H}\right)^{-3/4} \quad \text{and} \quad \ell(x) \propto \left(\frac{x}{H}\right)^{1/4}. \tag{4.9}$$

To determine if the power laws in (4.9) are satisfied in the wake of the block vehicle, a series of vertical profiles on the centerline at various downwind positions were obtained. The velocity deficit was computed for each profile and these are shown in Fig. 4.2. From these data, the maximum velocity deficit for each distance was determined (Fig. 4.3). A line corresponding to a -3/4 power law is a good fit to the data. A measure of the rate of growth of the length scale of the wake was also determined from the centerline vertical profiles of velocity deficit. According to the original theory and the associated definition of the length scale ℓ, the maximum velocity deficit occurs at a height of $z = 2\ell$. However, a strong shear near the surface in the velocity deficit profiles made it difficult to use this relationship to determine ℓ. As a measure of the length scale, the height at which the velocity deficit falls to one half the maximum value was determined for each vertical profile. The downwind distance, x, was measured from the rear of the vehicle. Fig. 4.4 shows that the data do support the 1/4 power relationship. The slow growth of the wake is shown in Fig. 4.5.

The theory in EH assumes an eddy viscosity dependent upon downwind distance or

$$\tau_{xz}/\rho = -\nu_T(x) , \tag{4.10}$$

where $\nu_T(x) = \gamma \ell(x) u_{max}(x)$.

Now (4.10) can be written as

$$\overline{u'w'} / \left(\frac{\partial u}{\partial z}\right) = \gamma \ell(x) u_{max}(x). \tag{4.11}$$

The left hand side of (4.11) was computed from the data on a point by point basis using cubic spline fits to velocity deficit profiles to obtain $\frac{\partial u}{\partial z}$. Near the top of the wake and near the maximum velocity deficit, $\overline{u'w'}$ and $\frac{\partial u}{\partial z}$ become small so that errors in $\overline{u'w'}/(\frac{\partial u}{\partial z})$ can be large. However, the ratio was found to be nearly constant over the range between these extremes and an average value was computed for each downwind distance. These are plotted in Fig. 4.6 which shows that the left hand side of (4.11) can be reasonably fitted with a line of slope -1/2. Since we have already shown that $u_{max} \propto (\frac{x}{H})^{-3/4}$, this implies again that

$$\ell(x) \propto \left(\frac{x}{H}\right)^{1/4} \tag{4.12}$$

However, the theory developed in EH does <u>not</u> describe the lateral spread of the wake as well as desired. The EH theory assumes that $\ell(x)$ is the correct length scale in both the vertical and lateral directions. This is equivalent to assuming the vehicle is as wide as it is high which is incorrect. The line through $\overline{u'v'}/(\frac{\partial u}{\partial y})$ in Fig. 4.6 lies well above the line through $\overline{u'w'}/(\frac{\partial u}{\partial z})$ implying different length scales for the vertical and lateral directions.

4.3 MODIFIED WAKE THEORY

A modified theory which accounts for different scale lengths in the lateral and vertical directions is derived in Appendix B. The solution for

the velocity deficit is the same as (4.4) except that now

$$\eta = yH/\lambda W \ell(x) \tag{4.13}$$

and the constant A in (4.4) is given by

$$A = \left[\frac{C_D}{32\pi e^{1/2}\lambda\gamma^3}\right]^{1/4} \tag{4.14}$$

where λ and γ are constants with values of 1.14 and 0.095, respectively. The length scales are

$$\ell_{vertical} = \ell(x) \quad \text{and} \quad \ell_{lateral} = \lambda \frac{W}{H} \ell(x) \tag{4.15}$$

4.4 HEIGHT-DEPENDENT-VISCOSITY WAKE THEORY

A further modification to the theory was made in an attempt to improve the agreement between the theory and data for the region of strong shear near the surface. The eddy viscosity was allowed to vary in the z direction as described in Appendix C, where the details of how the height dependence of the eddy viscosity was determined from spectra of $\overline{w'^2}$ are also presented. A numerical solution was then found.

Appendix D contains a simplified approach to a height-dependent eddy viscosity solution using a linear approximation in the strong shear layer and dividing the solution of the equation into two regions. The lower region has a linear increase in eddy viscosity and the upper region has a constant eddy viscosity. Results from this technique did not differ substantially from the numerical solution using a continuously variable eddy viscosity and are therefore not presented.

The three theories, original EH, modified lateral length scale, and height-dependent-viscosity, are compared with vertical and lateral velocity deficit profiles in Fig. 4.7 and 4.8, respectively. The height-dependent eddy viscosity theory lowers the height of the maximum deficit by a factor of nearly two and increases the shear near the surface (Fig. 4.7). However, the maximum in the data occurs still lower. The improvement in describing the lateral extent of the wake by the modified lateral length scale theory is evident in Fig. 4.8.

Lateral profiles of velocity deficit at a constant similarity height, ξ, are shown in Figure 4.9. These profiles are reduced to similarity coordinates and compared with the height-dependent-viscosity theory in Fig. 4.10. Vertical profiles of velocity deficit are compared with the height-dependent-viscosity theory in Fig. 4.11.

4.5 TURBULENT KINETIC ENERGY TERMS

Preliminary analysis of the fluctuating velocity data indicated that the lateral length scale determined for the velocity deficit would not collapse the profiles of the turbulent kinetic energy components (TKEC). The decay rate of the TKEC was also found to be different than that proposed in EH where complete self-preserving flow was assumed for the wake.

The turbulent energy budget equation can be written (Tennekes and Lumley, 1972)

$$\frac{1}{2} U_j \frac{\partial}{\partial x_j}(\overline{u_i u_i}) = -\frac{\partial}{\partial x_j}\left(\frac{1}{\rho}\overline{u_j p} + \frac{1}{2}\overline{u_i u_i u_j} - 2\nu\overline{u_i s_{ij}}\right) - \overline{u_i u_j} S_{ij} - 2\nu\overline{s_{ij} s_{ij}} \tag{4.16}$$

where

$$S_{ij} = \frac{1}{2}\left(\frac{\partial U_i}{\partial x_j} + \frac{\partial U_j}{\partial x_i}\right) \quad \text{and} \quad s_{ij} = \frac{1}{2}\left(\frac{\partial u_i}{\partial x_j} + \frac{\partial u_j}{\partial x_i}\right) \tag{4.17}$$

and the convention of repeated indices to indicate summation is used.

Assuming as for the velocity deficit solution that longitudinal changes scale with x, while crosswind changes scale with ℓ' where $\ell'/x \ll 1$, let $\mathcal{U}^2 = 1/3\ \overline{u_i u_i}$ and make order of magnitude estimates of the terms in (4.16). Assuming there is only one velocity and length scale in the wake:

$$U_j \frac{\partial}{\partial x_j}\left(\frac{1}{2}\overline{u_i u_i}\right) \sim U_\infty \mathcal{U}^2/x \qquad \frac{\partial}{\partial x_j}\left(2\nu \overline{u_i s_{ij}}\right) \sim \mathcal{U}^3/\ell'(\mathcal{U}\ell'/\nu)$$

$$-\frac{\partial}{\partial x_j}\left(\frac{1}{\rho}\overline{u_i p}\right) \sim \mathcal{U}^3/\ell' \qquad \overline{u_i u_j} S_{ij} \sim \mathcal{U}^3/\ell'$$

$$-\frac{\partial}{\partial x_j}\left(\frac{1}{2}\overline{u_i u_i u_j}\right) \sim \mathcal{U}^3/\ell' \qquad 2\nu \overline{s_{ij} s_{ij}} \sim \mathcal{U}^3/\ell'$$

The order-of-magnitude estimate of the last term, viscous dissipation, is based on experimental evidence for flows with one length scale, as discussed in Tennekes and Lumley. The fourth term is negligible due to the Reynolds number in the denominator, $(\mathcal{U}\ell/\nu) \gg 1$. Thus, the order of magnitude estimates for all of the terms on the right side of (4.16) are the same, $\mathcal{U}^3/\ell'$. If we say that the combination of the terms on the right side is of the same order of magnitude, we can write

$$\frac{U_\infty \mathcal{U}^2}{x} \sim \frac{\mathcal{U}^3}{\ell'} \tag{4.18}$$

If we assume power law forms for the x-dependence of the lateral length scale and decay rate of the TKEC, we can obtain a relation between the exponents. Let the lateral length scale $\ell' \propto x^\alpha$ and $(\overline{u'^2}, \overline{v'^2}, \overline{w'^2}) \propto x^{-\beta}$. Equating the exponents of x for both sides of this relation results in a restriction on α and β.

$$\alpha + \frac{\beta}{2} = 1 \tag{4.19}$$

A transverse Eulerian integral length scale defined by

$$\ell_E \equiv \int_0^\infty \frac{\overline{v'(0)v'(y)}}{\overline{v'(0)^2}}\, dy\,, \tag{4.20}$$

was computed from data obtained using two x-film probes. This length scale is believed (Tennekes and Lumley, 1972) to be comparable to the Lagrangian integral length scale for most turbulent flows and is thus a measure of the size of the dominant eddies within the wake. Thus, ℓ' should be related to ℓ_E; if we empirically determine the x-dependence of ℓ_E and assume $\ell' \propto \ell_E$ we can evaluate α and β.

The two probes were calibrated and then positioned in the wake of the block vehicle at one half of the vehicle height. One probe was positioned on the wake centerline while the other was moveable in the lateral direction. Profiles of $\overline{v'(o)\ v'(y)}$ were obtained at downwind distances of x/H = 15, 30, 45, and 60 (Fig. 4.12). For the greater downwind distances, $\overline{v'^2}$ in the wake was not large compared with background values, so $\overline{v'^2_{background}}$ was subtracted from $\overline{v'^2(0)}$ for each profile.

The length scale ℓ_E was determined for each of the profiles by a trapezoidal integration. A power-law fit corresponding to $\alpha = 0.40$ is shown in Fig. 4.13. The value of β computed from (4.19) is therefore 1.2. Using the computed length scale ℓ_E to normalize the space correlations of Fig. 1 collapses the data nicely (Fig. 4.14).

The maximum values of $\overline{u'^2}$ and $\overline{v'^2}$ were determined from the vertical centerline profiles obtained at various downwind distances. These are shown in

Fig. 4.15 along with the least squared error fit which gives $\beta = 1.2$, in agreement with the independent estimate from (4.19).

Thus, the vehicle-generated turbulence in the wake was found to decay as $(x/H)^{-1.2}$ and the lateral length scale was found to grow as $(x/H)^{0.4}$.

The spatial variation of the turbulent kinetic energy is assumed to be given by

$$(\overline{u'^2}, \overline{v'^2}, \overline{w'^2}) = (a_1, a_2, a_3) A^2 U_\infty^2 \left(\frac{x}{H}\right)^{-1.2} F_c(\chi, \omega), \tag{4.21}$$

$$A^4 = C_D / 32\pi e^{1/2} \lambda \gamma^3, \tag{4.22}$$

$$\chi = y / [W(x/H)^{0.4}] \quad \text{and} \quad \omega = z / [H(x/H)^{0.4}] \tag{4.23}$$

and

$$F_c(\chi, \omega)_{max} = 1.0. \tag{4.24}$$

At $(x/H) = 30$ detailed measurements were taken in the lateral direction using a 3-min. averaging period. The function $F_c(\chi,\omega)$ was determined by a least-squares fit using orthogonal polynomials of the fourth degree (Clark, Kubik and Phillips, 1963):

$$\begin{aligned} F_c(\chi,\omega) = {} & \Psi_{00} + \omega(\Psi_{01} + \omega(\Psi_{02} + \omega(\Psi_{03} + \omega\Psi_{04}))) \\ & + \chi^2(\Psi_{20} + \omega(\Psi_{21} + \omega(\Psi_{22} + \omega(\Psi_{23} + \omega\Psi_{24})))) \\ & + \chi^4(\Psi_{40} + \omega(\Psi_{41} + \omega(\Psi_{42} + \omega(\Psi_{43} + \omega\Psi_{44})))) \end{aligned}$$

subject to the following restrictions which result from limiting the domain of F_c to the wake region. $F_c(\chi,\omega) = 0.0$ when:

i) $|\chi| \geq 0.55$ or $|\omega| \geq 0.64$
ii) $\chi \leq 0.0$ and $\omega > 1.82\chi + 1.15$
iii) $\chi > 0.0$ and $\omega > -1.82\chi + 1.15$

The coefficients in (4.25) are found in Table 4.1. From these data the constants in (4.21) were found to be $a_1 = 0.048$, $a_2 = 0.040$, and $a_3 = 0.030$.

In Figs. 4.16 to 4.18 normalized cross-sections of the turbulence components $\overline{u'^2}$, and $\overline{w'^2}$ are shown fitted by the orthogonal polynomials of (4.25). The contours of F_c are presented in Fig. 4.19.

Using (4.21) with the numerical fit from Table 4.1, vertical and lateral profiles of the fluctuation velocity components can be estimated. Using similarity coordinates, data at various longitudinal distances can be plotted and compared to these estimates. Figs. 4.20 to 4.22 show linear and similarity plots of vertical profiles of $\overline{u'^2}$, $\overline{v'^2}$ and $\overline{w'^2}$, respectively. Figs. 4.23 and 4.24 show linear and similarity plots of lateral profiles $\overline{u'^2}$ and $\overline{w'^2}$.

4.6 REYNOLDS STRESSES IN THE WAKE

The wake theories presented in this paper and that of EH make no predictions regarding the decay of the Reynolds stresses. Bevilaqua and Lykoudis (1978) define a hierarchy of self-preserving wakes starting with order one, where mean velocity profiles are self-preserving; order two, where in addition Reynolds stresses are also self-preserving and so on.

From the data for centerline variation of the stresses (Fig. 4.25a for $\overline{u'w'}$), it is easy to show that the stresses decay as $(x/H)^{-3/2}$ and hence using the EH value of $(x/H)^{.25}$ as the length scale growth rate, the data collapse as shown in Fig. 4.25b. Fig. 4.25c is the same data plotted using TKEC similarity coordinates. It is easily seen that the wake is self-preserving of order two in terms of EH similarity variables. Fig. 4.26a and b show lateral profiles of $\overline{u'w'}$ at various (x/H) distances, and then the same data in EH similarity coordinates. The $\overline{u'v'}$ stresses, shown, are similar to the $\overline{u'w'}$ stresses.

TABLE 4.1 COEFFICIENTS OF POLYNOMIAL TWO-DIMENSIONAL FIT TO TURBULENT KINETIC ENERGY FUNCTION F_c.

$$\Psi_{00} = 0.3163277 \times 10^{-1}$$

$$\Psi_{01} = 0.1130908 \times 10^{2}$$

$$\Psi_{02} = -0.4320938 \times 10^{2}$$

$$\Psi_{03} = 0.6065336 \times 10^{2}$$

$$\Psi_{04} = -0.3218438 \times 10^{2}$$

$$\Psi_{20} = -0.1703226$$

$$\Psi_{21} = -0.8419376 \times 10$$

$$\Psi_{22} = -0.1640925 \times 10^{3}$$

$$\Psi_{23} = 0.5061181 \times 10^{3}$$

$$\Psi_{24} = -0.3599435 \times 10^{3}$$

$$\Psi_{40} = 0.2386405$$

$$\Psi_{41} = -0.8499160 \times 10^{2}$$

$$\Psi_{42} = 0.9322793 \times 10^{3}$$

$$\Psi_{43} = -0.2115435 \times 10^{4}$$

$$\Psi_{44} = 0.1360754 \times 10^{4}$$

REFERENCES

Abramowitz, M. , and L.A. Stegun, 1964: Handbook of Mathematical Functions. NBS Appl. Math. Ser., No. 55, 1046 pp.

Arya, S.P.S. and M.S. Shipman, 1979: A model study of boundary layer flow and diffusion over a ridge. Proc. AMS Fourth Symp. on Turbulence, Diffusion and Air Pollution, Jan. 15-18, Reno, NV. Am. Meteorological Soc., Boston, MA, p 584-91.

Bevilaqua, P.M. and P.S. Lykoudis, 1978: Turbulence memory in self preserving wakes. J. Fluid Mech., 89, 589-606.

Castro, I.P., 1979: Relaxing wakes behind surface-mounted obstacles in rough wall boundary layers. J. Fluid Mech., 93, 631-659.

Castro, I.P. and J.E. Fackrell, 1978: A note on two-dimensional fence flows, with emphasis on wall constraint. J. Indust. Aero., 3, 1-20.

Castro, I.P. and A.G. Robins, 1977: The flow around a surface-mounted cube in uniform and turbulent streams. J. Fluid Mech., 79, 307-335.

Clark, R.E., R.N. Kubik, and L.P. Phillips, 1963: Orthogonal polynomial least squares surface fit. Comm. ACM., 6, 146-148.

Counihan, J., J.C.R. Hunt and P.S. Jackson, 1974: Wakes behind two-dimensional surface obstacles in turbulent boundary layers. J. Fluid Mech., 64, 526-563.

Counihan, J., 1971: An experimental investigation of the wake behind a two-dimensional block and behind a cube in a simulated boundary layer flow. C.E.G.B. Lab Note, RD/LN115/71, Central Electricity Research Laboratories, Leatherhead England, 45 pp.

Eskridge, R.E. and J.C.R. Hunt, 1979: Highway modeling. Part I: Prediction of velocity and turbulence fields in the wake of vehicles. J. Appl. Meteor., 18, 387-400.

Goldstein, S., 1938: Modern Developments in Fluid Dynamics. Oxford University Press, Oxford. Reprinted by Dover.

Hansen, A.C. and J.E. Cermak, 1975: Vortex-containing wakes of surface obstacles. Project THEMIS Technical report no. 29. (Fluid Dynamics and Diff. Lab. Rpt.No. CER75-76ACH-JFC16,) Colorado State University. Ft. Collins, CO. 163 pp., Dec.

Hinze, J.O., 1975: Turbulence. McGraw-Hill, 790 pp.

Hunt, J.C.R., 1971: A theory for the laminar wake of a two-dimensional body in a boundary layer. J. Fluid Mech., 49, 159-178.

Hunt, J.C.R., 1974: Wakes behind buildings. Aeronautical Research Council (London), Paper ARC35601, Atmos. 229.

Hunt, J.C.R., 1980: Personal communication.

Kreyszig, E., 1962: Advanced Engineering Mathematics. John Wiley and Sons, Inc., New York, NY., 856 pp.

Lemberg, R., 1973: On the wakes behind bluff bodies in a turbulent boundary layer. Ph.D. thesis, University of Western Ontario, 152 pp.

Mason, W.T. and P.S. Beebe, 1978: The drag related flow field characteristics of trucks and buses, In: Aerodynamic Drag Mechanisms of Bluff Bodies and Road Vehicles, Edited by G. Sovran, Timorel and W. Mason, Plenum Press, New York, NY. pp 380.

Robins, A.G. and I.P. Castro, 1977: A wind tunnel investigation of plume dispersion in the vicinity of a surface mounted cube. I. The flow field. Atmos. Environ., 11, 291-297.

Schlichting, H., 1960: Boundary Layer Theory, Sixth edition, McGraw-Hill, New York, NY., 747 pp.

Smith, F.T., R.I. Sykes and P.W.M. Brighton, 1977: A two-dimensional boundary layer encountering a three-dimensional hump. J. Fluid Mech., 83, 163-176.

Snyder, W.H., 1979: The EPA Meteorological Wind Tunnel - Its Design, Construction, and Operating Characteristics. EPA 600/4-79-051, U.S. Environmental Protection Agency, Research Triangle Park, N.C., September, 78 pp.

Tennekes, H. and J.L. Lumley, 1972: A First Course in Turbulence, MIT Press, Cambridge, MA., 300 pp.

Townsend, A.A., 1976: The Structure of Turbulent Shear Flow, second edition, Cambridge University Press, Cambridge, England, 429 pp.

Woo, H.G.C., J.A. Peterka and J.E. Cermak, 1977: Wind tunnel measurements in the wakes of structures. NASA Contractor Rpt. NASA CR-2806, Colorado State University, Fort Collins, CO., 243 pp., March.

APPENDIX A

CONTROL VOLUME ANALYSIS

The overturning moment acting on the vehicle can be related to the velocity deficit in the wake with a control volume analysis. Consider the control volume enclosed by the box shown in Fig. A-1. The vehicle is excluded from the control volume and the effects of the vehicle on the flow are combined into the overturning moment, C. The small areas where the vehicle tires contact the ground are ignored in the analysis.

The vector equation for conservation of moment of momentum is

$$\sum \vec{M} = \iint_{c.s.} (\vec{r} \times \vec{q}) \rho \vec{q} \cdot \vec{n} \, dA + \frac{\partial}{\partial t} \iiint_{C.V.} \rho (\vec{r} \times \vec{q}) \, dV \qquad \text{(A-1)}$$

where $\Sigma \vec{M}$ is the sum of externally acting moments on the control volume, $\vec{r}$ is a position vector, $\vec{q}$ is the velocity vector (U-u,v,w), $\vec{n}$ is an outwardly directed unit vector, $\vec{i}$, $\vec{j}$, $\vec{k}$ are the unit vectors in the x,y,z directions respectively, and $\vec{M} = \vec{r} \times \vec{F}$ where $\vec{F}$ is a force on the control surface.

Steady state conditions are assumed, i.e. $\frac{\partial}{\partial t}(\,) = 0$. Since the overturning moment of the vehicle is about the y-axis, the dot product of $\vec{j}$ with (A-1) is taken; this, together with an assumption of constant density gives

$$\sum \vec{M} \cdot \vec{j} = \rho \iint_{c.s.} \vec{j} \cdot (\vec{r} \times \vec{q}) \, \vec{q} \cdot \vec{n} \, dA \qquad \text{(A-2)}$$

By definition, a shear stress component is positive when the shear stress and vector outwardly normal to the surface of action both act in the positive or negative directions. The shear stress, $\tau_{x_i x_j}$, acts in the x_j direction along

a surface normal to the x_i direction.

The external moment about the y-axis resulting from forces acting on Face 1 are due to pressure and shear stress:

$$\vec{j}\cdot(\vec{r}\times d\vec{F}_{pressure}) = \vec{j}\cdot\left[(-\vec{i}X_1+\vec{j}y+\vec{k}z)\times P(-X_1,y,z)\vec{i}\,dy\,dz\right]$$
$$= \vec{j}\cdot\left[-\vec{k}y\,P(-X_1,y,z)dy\,dz+\vec{j}z\,P(-X_1,y,z)dy\,dz\right]$$
$$= z\,P(-X_1,y,z)\,dy\,dz$$

and
$$\vec{j}\cdot(\vec{r}\times d\vec{F}_{\substack{shear\\stress}}) = \vec{j}\cdot\left[(-\vec{i}X_1+\vec{j}y+\vec{k}z)\times(-\vec{j}\tau_{xy}(-X_1,y,z)\right.$$
$$\left.-\vec{k}\tau_{xz}(-X_1,y,z))\,dy\,dz\right]$$
$$= \vec{j}\cdot\left[\vec{i}(-y\tau_{xz}(-X_1,y,z)+z\tau_{xy}(-X_1,y,z))\right.$$
$$\left.+\vec{j}(-X_1\tau_{xz}(-X_1,y,z))+\vec{k}(X_1\tau_{xy}(-X_1,y,z))\right]dy\,dz$$
$$= -X_1\tau_{xz}(-X_1,y,z)\,dy\,dz$$

Combining and integrating over the area of the face yields the total torque about the y-axis on

Face 1: $$\int_0^{Z_1}\int_{-Y_1}^{Y_1}\left[z\,P(-X_1,y,z)-X_1\tau_{xz}(-X_1,y,z)\right]dy\,dz.$$

In a similar manner the external moments on the other faces are found to be on

Face 2: $$\int_{-X_1}^{X_2}\int_0^{Z_1}\left[x\,\tau_{yz}(x,-Y_1,z)-z\,\tau_{yx}(x,-Y_1,z)\right]dz\,dx,$$

Face 3: $$\int_0^{Z_1}\int_{-Y_1}^{Y_1}\left[-zP(X_2,y,z)-X_2\tau_{xz}(X_2,y,z)\right]dy\,dz,$$

Face 4: $$\int_{-X_1}^{X_2}\int_0^{Z_1}\left[-x\tau_{yz}(x,Y_1,z)+z\tau_{yx}(x,Y_1,z)\right]dz\,dx,$$

Face 5: $$\int_{-X_1}^{X_2}\int_{-Y_1}^{Y_1}\left[xP(x,y,Z_1)+Z_1\tau_{zx}(x,y,Z_1)\right]dy\,dx$$

Face 6
(and vehicle surface): $$\int_{-X_1}^{X_2}\int_{-Y_1}^{Y_1}\left[-xP(x,y,0)\right]dy\,dx-C.$$

C is the overturning moment acting on the vehicle which is positive in the y direction; C is the result of all forces from pressure and stress acting on the surfaces of the vehicle.

Now the left hand side of (A-2) can be written

$$\begin{aligned}\sum \vec{M}\cdot\vec{j} = &\int_0^{Z_1}\int_{-Y_1}^{Y_1}\Big\{Z\big[P(-X_1,y,z)-P(X_2,y,z)\big]+X_1\tau_{xz}(-x,y,z)\\ &-X_2\tau_{xz}(X_2,y,z)\Big\}\,dy\,dz\\ &+2\int_{-X_1}^{X_2}\int_0^{Z_1}\big[Z\tau_{yx}(x,Y_1,z)-X\tau_{yz}(x,Y_1,z)\big]\,dx\,dz\ *\\ &+\int_{-X_1}^{X_2}\int_{-Y_1}^{Y_1}\Big\{X\big[P(x,y,Z_1)-P(x,y,0)\big]+Z_1\tau_{zx}(x,y,Z_1)\Big\}\,dy\,dx-C\,.\end{aligned} \tag{A-3}$$

We also can write the pressure as the sum of a mean and perturbation

$$P(x,y,z) = \bar{P} - p(x,y,z),$$

and we assume the perturbation pressure to be zero far upstream of the vehicle, i.e. $p(x_1, y, z) = 0$. The τ's may also be considered perturbation quantities since $\tau_{upstream} = 0$ (uniform flow). Equation A-3 can now be written as

* From symmetry, $\tau_{yx}(x,Y_1,z) = -\tau_{yx}(x, -Y_1,z)$, etc.

$$\sum \vec{M}\cdot\vec{j} = \int_0^{Z_1}\int_{-Y_1}^{Y_1}\left[z\,p(X_2,y,z) - X_2\,\tau_{xz}(X_2,y,z)\right]dy\,dz$$

$$+\,2\int_{-X_1}^{X_2}\int_0^{Z_1}\left[z\,\tau_{yx}(x,Y_1,z) - x\,\tau_{yz}(x,Y_1,z)\right]dz\,dx \tag{A-4}$$

$$+\int_{-X_1}^{X_2}\int_{-Y_1}^{Y_1}\Big\{x\left[-p(x,y,Z_1)+p(x,y,0)\right]$$

$$+\,Z_1\,\tau_{zx}(x,y,Z_1)\Big\}\,dy\,dx - C.$$

Now the moment of momentum crossing each face of the control surface must be computed, i.e. the right hand side of (A-2).

Face (1) $\vec{n} = -\vec{i}$, $\vec{r} = -X_1\vec{i} + y\vec{j} + z\vec{k}$ and $\vec{q} = U\vec{i}$

also $(\vec{r}\times\vec{q})\cdot\vec{j} = zU$ and $(\vec{n}\cdot\vec{q}) = -U$

therefore $$I_1 = -\rho\int_0^{Z_1}\int_{-Y_1}^{Y_1} z\,U^2\,dy\,dz.$$

Face (2) $\vec{n} = -\vec{j}$, $\vec{r} = x\vec{i} - Y_1\vec{j} + z\vec{k}$, and $\vec{q} = (U-u)\vec{i} + v\vec{j} + w\vec{k}$,

also $(\vec{r} \times \vec{q}) \cdot \vec{j} = z\left(U - u(x, -Y_1, z)\right) - x\,w(x, -Y_1, z)$,

and $(\vec{n} \cdot \vec{q}) = -v(x, -Y_1, z)$, and

$$I_2 = -\rho \int_{-X_1}^{X_2} \int_0^{Z_1} \left[z\left(U - u(x, -Y_1, z)\right) - x\,w(x, -Y_1, z)\right] v(x, -Y_1, z)\, dz\, dx.$$

Face (3) $\vec{n} = \vec{i}$, $\vec{r} = X_2\vec{i} + y\vec{j} + z\vec{k}$ and $\vec{q} = \left(U - u(X_2, y, z)\right)\vec{i} + v\vec{j} + w\vec{k}$

also $(\vec{r} \times \vec{q}) \cdot \vec{j} = z(U-u) - X_2 w$, and $\vec{n} \cdot \vec{q} = U - u$. Hence,

$$I_3 = \rho \int_0^{Z_1} \int_{-Y_1}^{Y_1} \left[z\left(U - u(X_2, y, z)\right) - X_2 w(X_2, y, z)\right]\left(U - u(X_2, y, z)\right) dy\, dz.$$

Face (4) $\vec{n} = \vec{j}$, $\vec{r} = x\vec{i} + Y_1\vec{j} + z\vec{k}$

and $q = (U-u)\vec{i} + v\vec{j} + w\vec{k}$

also $(\vec{r} \times \vec{q}) \cdot \vec{j} = z(U-u) - xw$

and $(\vec{n} \cdot \vec{q}) = v$

Thus $$I_4 = \rho \int_{-X_1}^{X_2} \int_0^{Z_1} \left[z\left(U - u(x, Y_1, z)\right) - x\,w(x, Y_1, z)\right] v(x, Y_1, z)\, dz\, dx.$$

Face (5) $\vec{n} = \vec{k}$, $\vec{r} = x\vec{i} + y\vec{j} + z_1\vec{k}$ and $\vec{q} = (U-u)\vec{i} + v\vec{j} + w\vec{k}$,

also $(\vec{r} \times \vec{q}) \cdot \vec{j} = z_1(U-u) - xw$ and $\vec{n} \cdot \vec{q} = w$,

$$I_5 = \rho \int_{-X_1}^{X_1} \int_{-Y_1}^{Y_1} [z_1(U - u(x,y,z_1)) - xw(x,y,z_1)] w(x,y,z_1)\, dy\, dx.$$

Face (6) and vehicle surface: $\vec{n} \cdot \vec{q} = 0$,

$$I_6 = 0.$$

The above integrals can be combined to get the right hand side of (A-2) noting that due to symmetry, $u(x,Y_1,z) = u(x,-Y_1,z)$, $v(x,Y_1,z) = -v(x,-Y_1,z)$ and $W(x,Y_1,z) = w(x,-Y_1,z)$, the contributions due to surfaces 2 and 4 add. Second order terms like u^2 and uv have been neglected.

Solving (A-2) for C and by use of (A-3) yields

$$\begin{aligned} C = &\int_0^{z_1} \int_{-Y_1}^{Y_1} \{ z p(X_2,y,z) - X_2 \tau_{xz}(X_2,y,z) + 2z\rho U u(X_2,y,z) \\ &+ X_2 \rho U w(X_2,y,z) \} dy\, dz + \int_{-X_1}^{X_2} \int_{-Y_1}^{Y_1} \{ x[-p(x,y,z_1) + p(x,y,0)] \\ &+ z_1 \tau_{zx}(x,y,z_1) - z_1 \rho U w(x,y,z_1) \} dy\, dx \\ &+ 2 \int_{-X_1}^{X_2} \int_0^{z_1} \{ [z\tau_{yx}(x,Y_1,z) - x\tau_{yz}(x,Y_1,z)] + zUv(x,Y_1,z) \} dz\, dx. \end{aligned} \tag{A-5}$$

Now $|w| \ll |u|$ (from EH), so that $X_2 Uw \ll zUu$ in the first integral.

Let $Z_1 \to \infty$; then $p(x,y,Z_1) \to 0$, $w(x,y,Z_1) \to 0$, and $\tau_{zx}(x,y,Z_1) \to 0$.

Also let $Y_1 \to \infty$; then $\tau_{yx}(x,Y_1,z) \to 0$ and $v(x,Y_1,z) \to 0$. Let $-X_1 \to -\infty$, and since X_2 is arbitrary it can be replaced with x, reducing (A-5) to

$$C \cong \int_0^\infty \int_{-\infty}^\infty [zp - \tau_{xz} + 2\rho U u z]\, dy\, dz + \int_{-\infty}^{x} \int_{-\infty}^\infty x p(x,y,0)\, dy\, dx. \qquad \text{(A-6)}$$

The first equation of motion in perturbation form is

$$-U \frac{\partial u}{\partial x} = \frac{1}{\rho}\frac{\partial p}{\partial x} + \frac{1}{\rho}\frac{\partial \tau_{xz}}{\partial z} + \frac{1}{\rho}\frac{\partial \tau_{xy}}{\partial y}. \qquad \text{(A-7)}$$

Since there are no momentum sources in the control volume from x = x to x = ∞, y = $-\infty$ to y = ∞, z = 0 to z = ∞, eq. (A-7) holds everywhere and can be integrated over this volume.

Integrating (A-7) with respect to y from $-\infty$ to ∞ yields

$$-\int_{-\infty}^\infty U \frac{\partial u}{\partial x}\, dy = \frac{1}{\rho}\int_{-\infty}^\infty \frac{\partial p}{\partial x}\, dy + \frac{1}{\rho}\int_{-\infty}^\infty \frac{\partial \tau_{xz}}{\partial z}\, dy + \frac{1}{\rho}\int_{-\infty}^\infty \frac{\partial \tau_{xy}}{\partial y}\, dy. \qquad \text{(A-8)}$$

Now $\frac{1}{\rho}\int_{-\infty}^\infty \frac{\partial \tau_{xy}}{\partial y}\, dy = \tau_{xy}\Big|_{-\infty}^{\infty} = 0$, yielding

$$-\rho \int_{-\infty}^\infty U \frac{\partial u}{\partial x}\, dy = \int_{-\infty}^\infty \frac{\partial p}{\partial x}\, dy + \int_{-\infty}^\infty \frac{\partial \tau_{xz}}{\partial z}\, dy. \qquad \text{(A-9)}$$

Integrating (A-9) with respect to x from x to ∞ yields

$$-\int_x^\infty \int_{-\infty}^\infty U \frac{\partial u}{\partial x}\, dy\, dx = \frac{1}{\rho}\int_x^\infty \int_{-\infty}^\infty \frac{\partial p}{\partial x}\, dy\, dx + \frac{1}{\rho}\int_x^\infty \int_{-\infty}^\infty \frac{\partial \tau_{xz}}{\partial z}\, dy\, dx. \qquad \text{(A-10)}$$

or

$$\rho \int_{-\infty}^{\infty} uU\,dy = -\int_{-\infty}^{\infty} p\,dy + \int_{x}^{\infty}\int_{-\infty}^{\infty} \frac{\partial \tau_{xz}}{\partial z}\,dy\,dx. \tag{A-11}$$

Multiply by z and integrate with respect to z from 0 to ∞

$$\int_{0}^{\infty}\int_{-\infty}^{\infty} \rho z u U\,dy\,dz = \int_{0}^{\infty}\int_{-\infty}^{\infty} z p\,dy\,dz + \int_{0}^{\infty}\int_{x}^{\infty}\int_{-\infty}^{\infty} \frac{\partial \tau_{xz}}{\partial z}\,dy\,dx\,dz. \tag{A-12}$$

But,

$$\int_{0}^{\infty} z \int_{x}^{\infty}\int_{-\infty}^{\infty} \frac{\partial \tau_{xz}}{\partial z}\,dy\,dx\,dz = \int_{-\infty}^{\infty}\int_{x}^{\infty}\int_{0}^{\infty} z\,\frac{\partial \tau_{xz}}{\partial z}\,dz\,dx\,dy.$$

and

$$\int_{0}^{\infty} z\,\frac{\partial \tau_{xz}}{\partial z}\,dz = z\,\tau_{xz}\Big|_{0}^{\infty} - \int_{0}^{\infty} \tau_{xz}\,dz = -\int_{0}^{\infty} \tau_{xz}\,dz, \tag{A-13}$$

so that (A-12) becomes

$$\int_{0}^{\infty}\int_{-\infty}^{\infty} z p\,dy\,dz = -\int_{0}^{\infty}\int_{-\infty}^{\infty} \rho z u U\,dy\,dz - \int_{0}^{\infty}\int_{-\infty}^{\infty}\left[\int_{x}^{\infty} \tau_{xz}\,dx\right] dy\,dz. \tag{A-14}$$

And (A-6) can now be written as

$$\begin{aligned} C &= \int_{0}^{\infty}\int_{-\infty}^{\infty}\left[\rho u U z - x\tau_{xz} - \int_{x}^{\infty} \tau_{xz}\,dx\right] dy\,dz + \int_{-\infty}^{\infty}\int_{-\infty}^{x} x\,p(x,y,0)\,dx\,dy \\ &= \int_{0}^{\infty}\int_{-\infty}^{\infty} \rho u U z\,dy\,dz - \int_{-\infty}^{\infty} x\,\tau_{xz}\,dz\,dy - \int_{-\infty}^{\infty}\int_{x}^{\infty}\int_{0}^{\infty} \tau_{xz}\,dz\,dx\,dy \\ &\quad + \int_{-\infty}^{\infty}\int_{\infty}^{x} x\,p(x,y,0)\,dx\,dy. \end{aligned} \tag{A-15}$$

Since

$$\int_0^\infty \tau_{xz}\,dz = -\nu_T \int_0^\infty \frac{\partial u}{\partial z}\,dz = -\nu_T u\Big|_0^\infty = 0, \tag{A-16}$$

(A-15) becomes

$$C = \int_0^\infty\int_{-\infty}^\infty \rho u U z\,dy\,dz + \int_{-\infty}^\infty\int_{-\infty}^x x p(x,y,0)\,dx\,dy. \tag{A-17}$$

Now (A-7) can be written for distances sufficiently far downwind that the perturbation pressure is negligible (see section 4.1), as

$$U\frac{\partial u}{\partial x} = \nu_T(x)\left[\frac{\partial^2 u}{\partial y^2} + \frac{\partial^2 u}{\partial z^2}\right] \tag{A-18}$$

Multiply this by z, integrate the right hand side by parts from $z = 0$ to ∞ and then integrating with respect to y from $-\infty$ to ∞, to get

$$\frac{\partial}{\partial x}\int_{-\infty}^\infty\int_0^\infty \rho u U z\,dy\,dz = 0$$

or

$$\int_{-\infty}^\infty\int_0^\infty \rho u U z\,dy\,dz = \text{constant, at large } x. \tag{A-19}$$

The couple on the vehicle for a given situation is a value that could be determined by measurement. At distances sufficiently downwind for (A-19) to hold, we can therefore conclude that the second integral on the right of (A-17) is a constant, not a function of x. It is assumed that the second integral in (A-17) is small and therefore the couple on the vehicle determines the wake strength. Hunt (1974) indicates that the second integral can be neglected for three dimensional objects.

When the stress is approximated by a viscosity that varies in the vertical direction the analysis is similar to that given with the following modifications. Equation (4.1) in section 4.1 takes the form

$$\rho U \frac{\partial u}{\partial x} = \nu_T(x) \left[\frac{\partial}{\partial z} \left(H^*(x,z) \frac{\partial u}{\partial z} \right) + \frac{\partial^2 u}{\partial y^2} \right], \tag{A-20}$$

where $H^*(x,z)$ is the vertical dependence of viscosity

Multiplying by z and integrating with respect to y and z yields

$$\frac{\partial}{\partial x} \int_{-\infty}^{\infty} \int_{0}^{\infty} z \rho U u \, dz \, dy = \nu_T(x) \int_{-\infty}^{\infty} \left[- \int_{0}^{\infty} H^*(x,z) \frac{\partial u}{\partial z} dz \right] dy. \tag{A-21}$$

(A-21) then gives an integral constraint on the definition of $H^*(x,z)$ i.e.

$$\int_{0}^{\infty} H^*(x,z) \frac{\partial u}{\partial z} dz = 0 \tag{A-22}$$

since the right hand side of (A-21) must be zero. From (A-21) and (A-22)

$$\int_{-\infty}^{\infty} \int_{0}^{\infty} z \rho U u \, dz \, dy = \text{constant}. \tag{A-23}$$

The analysis of the couple would be the same since (A-16) would take the form

$$\int_{0}^{\infty} \tau_{xz} \, dz = - \nu_T(x) \int_{0}^{\infty} H^*(x,z) \frac{\partial u}{\partial z} dz = 0. \tag{A-24}$$

In the work presented in this paper it is assumed that (A-22) is satisfied.

APPENDIX B

MULTI-SCALE WAKE THEORY

The following derivation follows very closely the form in EH. The assumptions are the same as those given in Section 4.1 and we use the same notation.

The linearized first equation of motion is given

$$-\rho U \frac{\partial u}{\partial x} = \frac{\partial p}{\partial x} + \frac{\partial \tau_{xz}}{\partial z} + \frac{\partial \tau_{xy}}{\partial y} \tag{B-1}$$

where the shearing stresses are assumed to have the form

$$\tau_{xz}/\rho = -\nu_T \frac{\partial u}{\partial z} \quad \text{and} \quad \tau_{xy}/\rho = -\lambda^2 \frac{W^2}{H^2} \nu_T \frac{\partial u}{\partial y}, \tag{B-2}$$

where W and H are the width and height of the vehicle, respectively, and

$$\nu_T(x) = \gamma \ell(x) u_{max}(x). \tag{B-3}$$

We have allowed for different length scales in the lateral and vertical and assume them to be related by

$$\ell_{vertical} = \ell(x) \quad \text{and} \quad \ell_{lateral} = \lambda \frac{W}{H} \ell(x). \tag{B-4}$$

As in EH it can be shown that $\partial p/\partial x$ can be neglected. (B-1) now becomes

$$U \frac{\partial u}{\partial x} = \nu_T(x) \left[\frac{\partial^2 u}{\partial z^2} + \lambda^2 \frac{W^2}{H^2} \frac{\partial^2 u}{\partial y^2} \right]. \tag{B-5}$$

Assume a solution of the form

$$u = U\left(\frac{x}{H}\right)^{-m} A\, f\left[z/\ell(x),\ yH/\lambda W \ell(x)\right], \tag{B-6}$$

where A is a constant to be determined and $f \leq 1$.

Now, let

$$\zeta = z/\ell(x) \quad \text{and} \quad \eta = yH/\lambda W \ell(x) \tag{B-7}$$

and substitute (B-6) into (B-5) to get

$$U\left(\frac{-m}{H}\right)\left(\frac{x}{H}\right)^{-1} f(\zeta,\eta) - U\frac{1}{\ell(x)}\frac{d\ell(x)}{dx}\left[\zeta f_\zeta + \eta f_\eta\right] = \frac{\nu_T(x)}{\ell^2(x)}\left[f_{\zeta\zeta} + f_{\eta\eta}\right]. \tag{B-8}$$

Along a path where $f = f_{max} = 1$, one finds

$$f_\zeta = f_\eta = 0 \quad \text{and} \quad f_{\zeta\zeta} = \text{constant},\ f_{\eta\eta} = \text{constant}. \tag{B-9}$$

Hence

$$U\left(\frac{-m}{H}\right)\left(\frac{x}{H}\right)^{-1} = \frac{\nu_T(x)}{\ell^2(x)} \times \text{constant} \tag{B-10}$$

which implies

$$\frac{U}{x} \propto \frac{\nu_T(x)}{\ell^2(x)} \quad \text{or} \quad \ell(x) \propto x\, U_{max}(x). \tag{B-11}$$

From the control volume analysis given in Appendix A the overturning couple on the vehicle is given by

$$C = \rho \int_{-\infty}^{\infty} \int_{0}^{\infty} z u U \, dz \, dy \cong \frac{\rho C_D}{4} U^2 H^2 W. \tag{B-12}$$

The approximation on the right is obtained by taking the overturning moment to be the drag force times one-half the vehicle height.

If we substitute (B-6) into (B-12) the integral constraint becomes

$$C = \lambda \frac{W}{H} U^2 A \left(\frac{x}{H}\right)^{-m} \ell^3(x) \int_{-\infty}^{\infty} \int_{0}^{\infty} \zeta f(\zeta, \eta) \, d\zeta \, d\eta. \tag{B-13}$$

Hence,

$$C \propto \lambda \frac{W}{H} U^2 A \left(\frac{x}{H}\right)^{-m} \ell^3(x) \quad \text{or} \quad \ell^3(x) \left(\frac{x}{H}\right)^{-m} = \text{constant}. \tag{B-14}$$

From (B-11) and (B-14)

$$x^3 \, x^{-3m} \, x^{-m} = \text{constant}, \tag{B-15}$$

which implies that $m = 3/4$. Thus, we have $u_{max}(x) \propto x^{-3/4}$ and $\ell(x) \propto x^{1/4}$. If we define $\ell(x) = \gamma AH \, (x/H)^{1/4}$, and note that $u_{max} = AU \, (x/H)^{-3/4}$, (B-8) becomes

$$f_{\zeta\zeta} + f_{\eta\eta} + \frac{1}{4}(\zeta f_{\zeta} + \eta f_{\eta}) + \frac{3}{4} f = 0 \tag{B-16}$$

describing the behavior of the velocity deficit in all planes normal to the wake.

The solution to (B-16) is known (EH) to be

$$f(\zeta,\eta) = \frac{\Lambda_1}{(8\pi)^{1/2}} \zeta \exp\left[-(\zeta^2+\eta^2)/8\right], \tag{B-17}$$

where $\Lambda_1 = (2\pi e)^{1/2}$

The constant A can now be computed using (B-12) and (B-17);

$$\frac{C_D}{4} U^2 H^2 W = U u_{max} \left(\frac{\lambda W}{H}\right) \lambda^3 \int_{-\infty}^{\infty}\int_{0}^{\infty} \zeta f(\zeta,\eta)\, d\zeta\, d\eta, \tag{B-18}$$

yielding

$$A = \left[\frac{C_D}{32\pi e^{1/2} \lambda \gamma^3}\right]^{1/4}. \tag{B-19}$$

The solution for the velocity deficit is now known (B-6, B-17, and B-19) except for two constants γ and λ.

To determine λ we use (B-2);

$$\nu_T(x) = \overline{u'w'} \Big/ \left(\frac{\partial u}{\partial z}\right) \tag{B-20}$$

and

$$\lambda^2 \frac{W^2}{H^2} \nu_T(x) = \overline{u'v'} \Big/ \left(\frac{\partial u}{\partial y}\right). \tag{B-21}$$

The right hand sides of (B-20) and (B-21) have been determined at various downwind distances by fitting vertical and lateral velocity profiles with cubic splines which were differentiated to determine the velocity gradients (Fig. B-1). Above the maximum velocity deficit the velocity gradient was well behaved and averaged values of $-\overline{u'w'}/(\partial u/\partial z)$ and $-\overline{u'v'}/(\partial v/\partial z)$ are plotted in Fig. 4.5. The straight lines fitting these points are least squares linear fits to the data.

The value of λ can now be determined by using, say, x/H = 10 and the fitted values to the profiles yielding

$$\lambda = \frac{H}{W}\left[\left(\overline{u'v'}\Big/\frac{\partial u}{\partial z}\right)\Big/\left(\overline{u'w'}\Big/\frac{\partial u}{\partial y}\right)\right]^{1/2} = \frac{0.043}{0.056}\left(\frac{0.015}{0.007}\right)^{1/2} = 1.19\,. \tag{B-22}$$

To determine γ we rewrite B-3 as

$$\nu_T(x) = \gamma\, l(x)\, u_{max}(x) = \gamma^2 A^2 H \left(\frac{x}{H}\right)^{-1/2} U \tag{B-23}$$

or

$$\frac{\nu_T^2}{U^2H^2} = \frac{\gamma^4 A^4}{(x/H)} \tag{B-24}$$

At $x/H = 10$, $\nu_T^2/U^2H^2 = (0.007)^2$ and by use of (B-19) one finds that

$$\gamma = 0.095. \tag{B-25}$$

APPENDIX C

HEIGHT-DEPENDENT-VISCOSITY WAKE THEORY

Assume the perturbation equation of motion (B-1) can be written as

$$U\frac{\partial u}{\partial x} = \frac{\partial}{\partial z}\left(H^*(x,z)\nu_T(x)\frac{\partial u}{\partial z}\right) + \frac{\partial}{\partial y}\left(\lambda^2\frac{W^2}{H^2}\nu_T(x)\frac{\partial u}{\partial y}\right), \tag{C-1}$$

where $H^*(x,z)$ is some function of height having a continuous derivative. From Appendix B we can express (C-1) and its solution as

$$\frac{\partial u}{\partial x} = \bar{x}^{-1/2}\left[\frac{\partial}{\partial z}\left(H^*(x,z)\frac{\partial u}{\partial z}\right) + \frac{\partial^2 u}{\partial y^2}\right] \tag{C-2}$$

and

$$u = UA\left(\frac{x}{H}\right)^{-3/4} f\left(\bar{z}/\ell(x), \bar{y}/\ell(x)\right) \tag{C-3}$$

where

$$\bar{x} = (x/H)\ , \ \bar{z} = z/\gamma AH, \text{ and } \bar{y} = y/\lambda\gamma AW. \tag{C-4}$$

Substituting (C-3) into (C-2) yields for f the partial differential equation ($\tilde{H}(\zeta)$ is the transform of $H^*(x,z)$ and $\tilde{H}(\zeta) \leq 1$)

$$\tilde{H}(\zeta) f_{\zeta\zeta} + f_{\eta\eta} + \tilde{H}_{\zeta}(\zeta) f_{\zeta} + \frac{1}{4}(\zeta f_{\zeta} + \eta f_{\eta}) + \frac{3}{4} f = 0. \tag{C-5}$$

Equation (C-5) can be solved in part by assuming it is separable, i.e.

$$f(\zeta,\eta) = T(\zeta) Y(\eta) \tag{C-6}$$

This yields

$$Y(\eta) = C_1 e^{-\eta^2/8}$$

and

$$\tilde{H} T'' + \frac{3}{4} T' + \tilde{H}' T' + \frac{T}{2} = 0, \tag{C-7}$$

where (C-7) is subject to the boundary conditions

$$T(0) = 0, \quad T_{max}(\zeta) = 1. \tag{C-8}$$

Analytic solutions are easily found for (C-7) and (C-8) only when $\tilde{H}(\zeta)$ is a simple function. Hence, (C-7) and (C-8) have been solved numerically using the Runge-Kutta-Nystrom method (Kreyszig, 1962).

To arrive at an expression for $\tilde{H}(\zeta)$ we have taken data along the centerline (y=0) at x/H = 30 for z/H = 0.15, 0.29, 0.44, 0.59, 0.74, 0.88, 1.03, 1.18,

1.32, 1.47, 1.76, 2.06, 2.35, and 2.94, which allowed us to compute spectra at each height (see Fig. C-1). We further assumed that

$$\nu_T \propto (\overline{w'^2})^{1/2} U/N \quad \text{or} \quad \tilde{H}(\zeta) \propto (\overline{w'^2})^{1/2} U(\zeta)/N, \tag{C-10}$$

where $(\overline{w'^2})^{1/2}$ is the standard deviation of the vertical velocity, $U(\zeta)$ is the mean wind speed at height ζ, and N is the frequency containing the maximum energy. A best N was determined for each height from the spectra together with estimated upper and lower bounds. The product $(\overline{w'^2})^{1/2}$ $U(\zeta)$ N is normalized by dividing by its maximum value. These results together with error ranges are plotted in Fig. C-2. The following function describing $\tilde{H}(\zeta)$ was found by a least-squares fit to the data in Fig. C-2, after changing variables from z/H to ζ.

$$\tilde{H}(\zeta) = 0.2616 + 0.48745 \cdot 0.096175^2 + 0.0061935^3 - 0.00013055^4 \tag{C-11}$$

In order to describe the vertical change in viscosity we plotted $\overline{u'w'}/(\partial u/\partial z)$ from data taken with the 1/8 scale block vehicle. The vertical velocity gradient was estimated at each point with a cubic spline fit. The estimate naturally contains error and is partly responsible for the scatter in Fig. C-3. Careful study of Figure C-2 and C-3 shows that, except for scatter, the trends in both plots are the same and the maximum occurs near z/H = 1.25 in both plots.

APPENDIX D

SIMPLIFIED HEIGHT-DEPENDENT-VISCOSITY WAKE THEORY

A simple approximation for the height-dependence of the eddy viscosity can be made that will lead to an analytic solution. If we assume that viscosity distribution function $\tilde{H}(\zeta)$ has the form

$$\begin{aligned} \tilde{H}(\zeta) &= \alpha\zeta + \beta \ , \quad \text{for } \zeta \leq \zeta_c \\ &= 1.0 \ , \quad \text{for } \zeta > \zeta_c \ , \end{aligned} \tag{D-1}$$

then (C-8) can be solved as follows. Substituting (D-1) and its derivative into (C-8) yields (assuming $\zeta < \zeta_c$)

$$4(\alpha\zeta + \beta)T'' + (\zeta + 4\alpha)T' + 2T = 0. \tag{D-2}$$

(D-2) can be transformed into a standard form of Kummer's equation by (Abramowitz and Stegun, 1964)

$$\zeta = -4\alpha\bar{z} + \beta/\alpha \tag{D-3}$$

Eq. (D-2) becomes

$$\bar{z}\,T_{\bar{z}\bar{z}} + \left(1 - \frac{\beta}{4\alpha^2} - \bar{z}\right)T_{\bar{z}} - 2T. \tag{D-4}$$

The general solution to (D-4) is

$$T(\bar{z}) = \Lambda_2 \bar{z}^{1-b} M(1+a-b, 2-b, \bar{z}) + \Lambda_3 M(a,b,\bar{z}) \equiv f_2(\bar{z}) \qquad \text{(D-5)}$$

where Λ_2 and Λ_3 are constants and the power series, M(a,b,z), is defined by

$$M(a,b,z) = 1 + \frac{az}{b} + \frac{(a)_2 z^2}{(b)_2 z!} + \cdots , \qquad \text{(D-6)}$$

where $(a)_n = a(a+1)\,(a+2)\ldots(a+n-1)$ and $(a)_0 = 1$.

In (D-5) $\quad a = 2, \; b = 1 - \beta/4\alpha^2, \; \bar{z} = (\zeta + \beta/\alpha)/4\alpha \qquad$ (D-7)

While the first part of the solution can be expressed in terms of elementary functions as

$$\Lambda_2 \bar{z}^{\beta/4\alpha^2} e^{\bar{z}} \left[1 + \bar{z}/(1+\beta/4\alpha^2)\right] \qquad \text{(D-8)}$$

no such simplification appears to be obtainable for M(a,b,z).

Above the height ζ_c, where $\tilde{H}(\zeta) = 1$, the general solution was found in EH to be (for the differential equation describing the vertical variation of the solution)

$$\begin{aligned} \bar{T}(\bar{\zeta}) &= B_1 M(1, 1/2, \bar{\zeta}) + B_2 M(3/2, 3/2, \bar{\zeta}) \\ &\equiv f_1(\bar{\zeta}) \quad \text{where } \bar{\zeta} = -\zeta^2/8. \end{aligned} \qquad \text{(D-9)}$$

In order to match solutions, it is necessary to assume that γ and A (defined in Appendix B) are independent of the assumed form of viscosity used in each model. Otherwise the ζ in D-9 and D-8 will not be the same coordinate.

The two solutions D-5 and D-9 have four unknown constants; therefore, it is necessary to specify four constraints on the problem.

The boundary condition U(0) = 0 means

$$f_2(\bar{z}) = 0 \quad \text{at} \quad \zeta = 0 \tag{D-10}$$

which furnishes the first condition. Requiring a continuous solution and derivative at the matching point ξ_c requires that

$$f_2(\bar{z}) = f_1(\bar{\zeta}) \tag{D-11}$$

and $$\frac{d}{d\zeta}\left(f_2(\bar{z})\right) = \frac{d}{d\zeta}\left(f_1(\bar{\zeta})\right) \quad \text{at} \quad \zeta = \zeta_c$$

The fourth condition used is that

$$\max \quad f_1, f_2 = 1.0. \tag{D-12}$$

With the constraints given in D-10 thru D-12, the normalized variation of velocity deficit in the vertical can be computed and the lateral variation can be computed using (C-7).

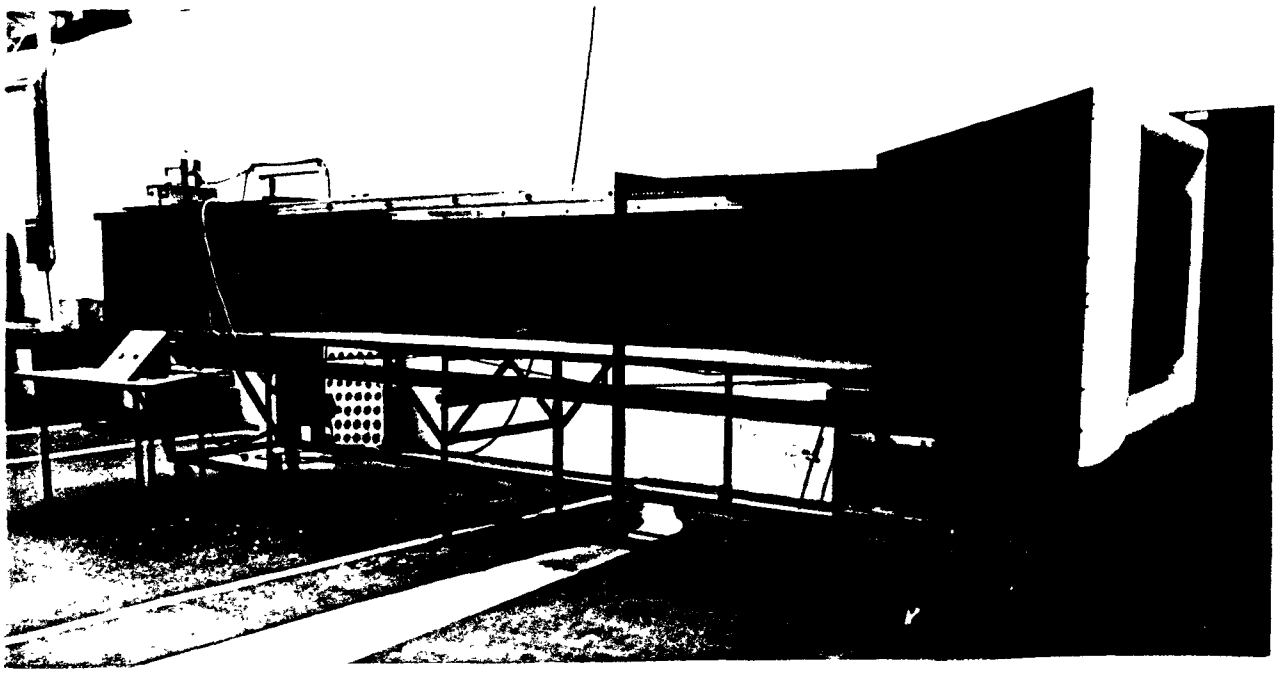

Figure 3.1. The wind tunnel.

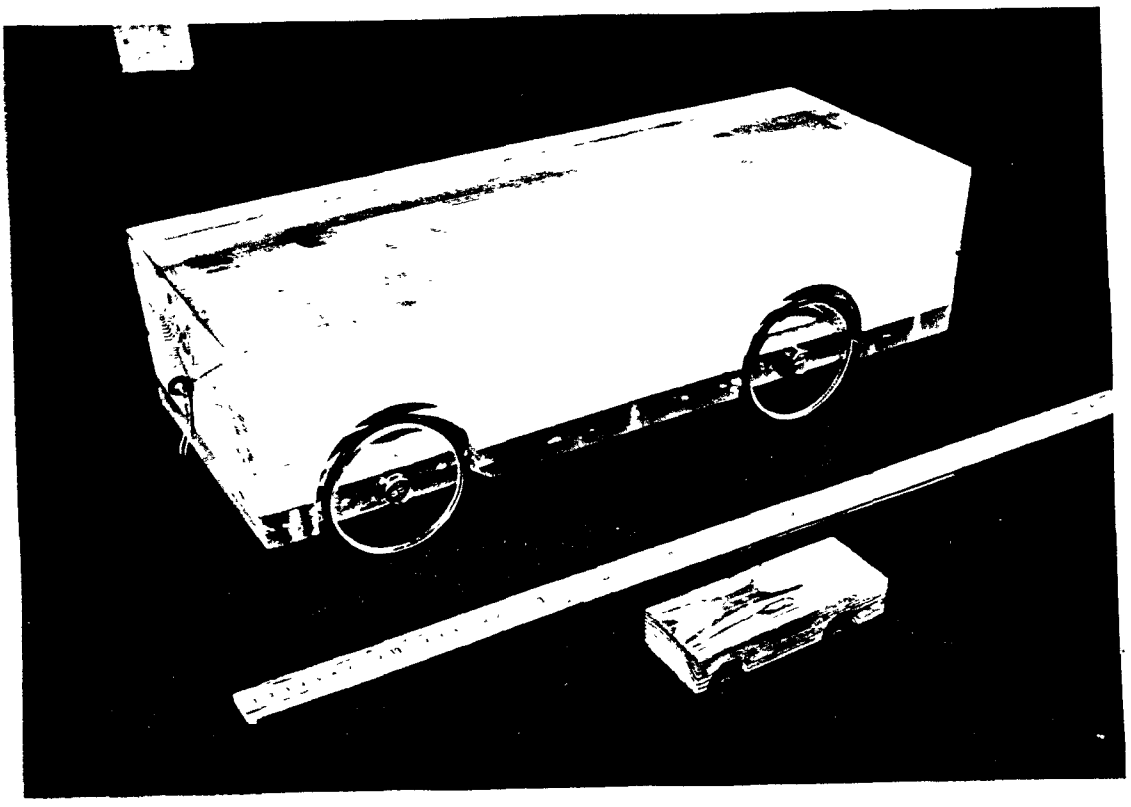

Figure 3.2. Scale model vehicles.

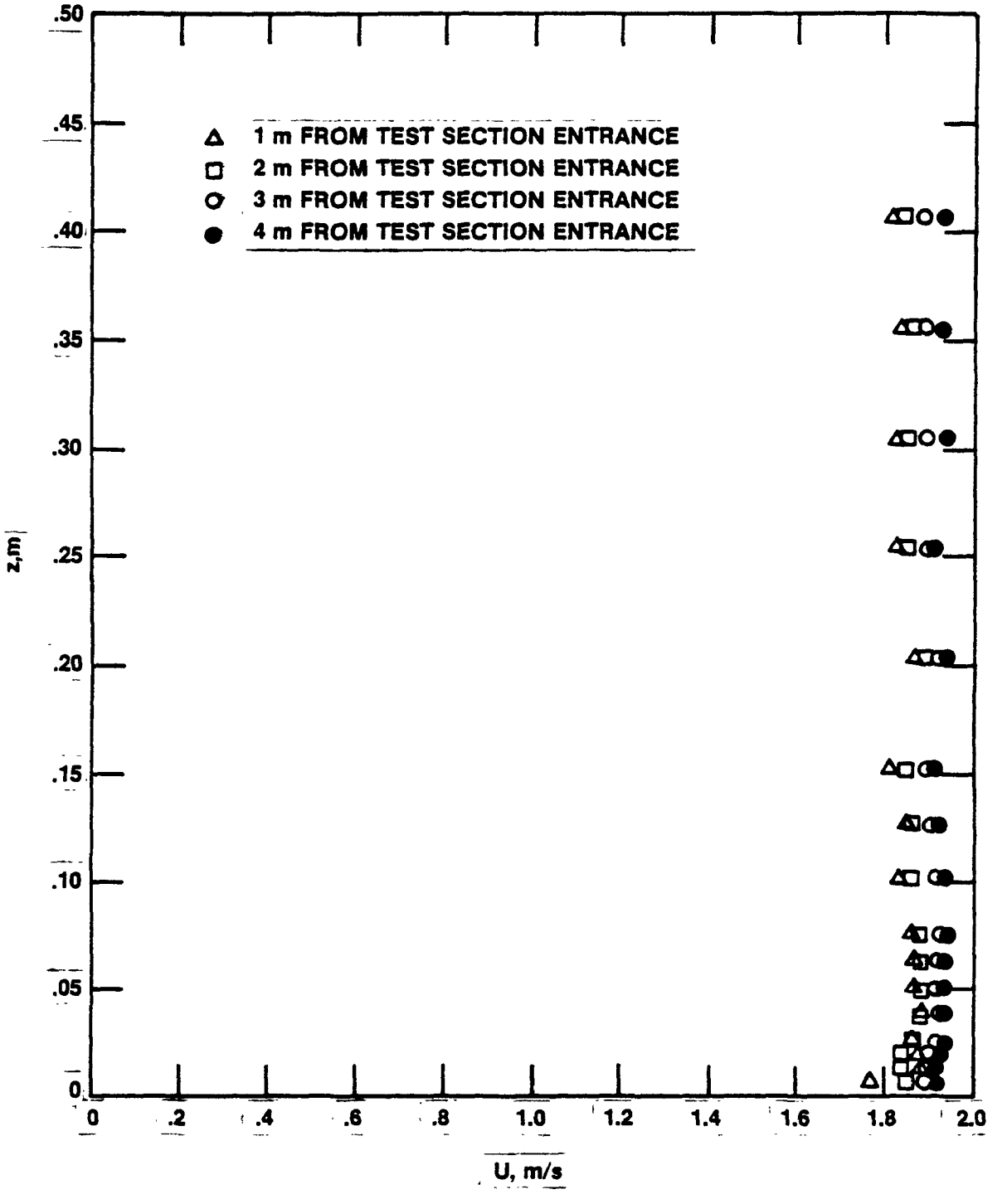

Figure 3.3. Empty tunnel, mean velocity profiles for four longitudinal positions on centerline.

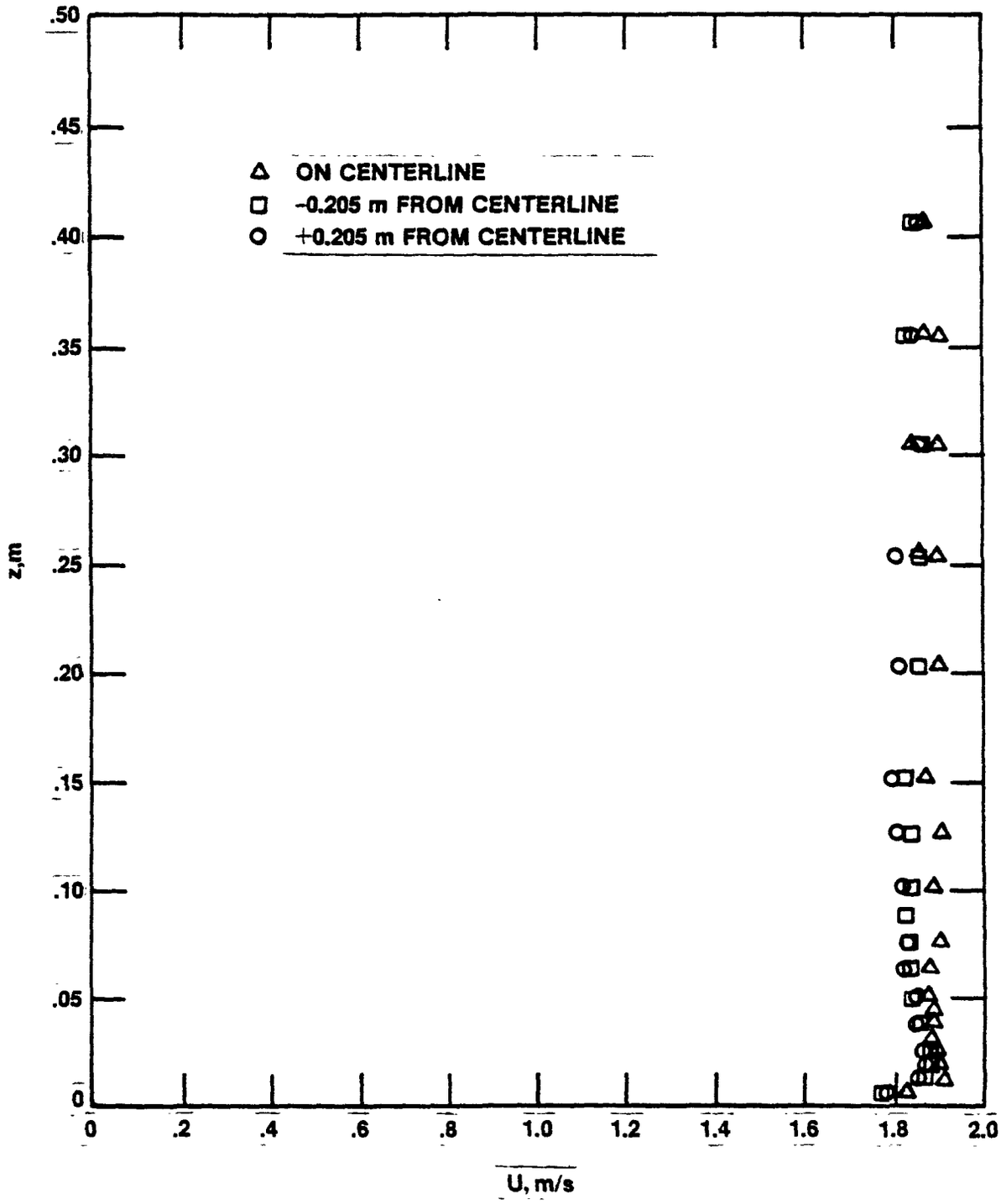

Figure 3.4. Empty tunnel, mean velocity profiles for three lateral positions at a distance of 1m from the test section entrance.

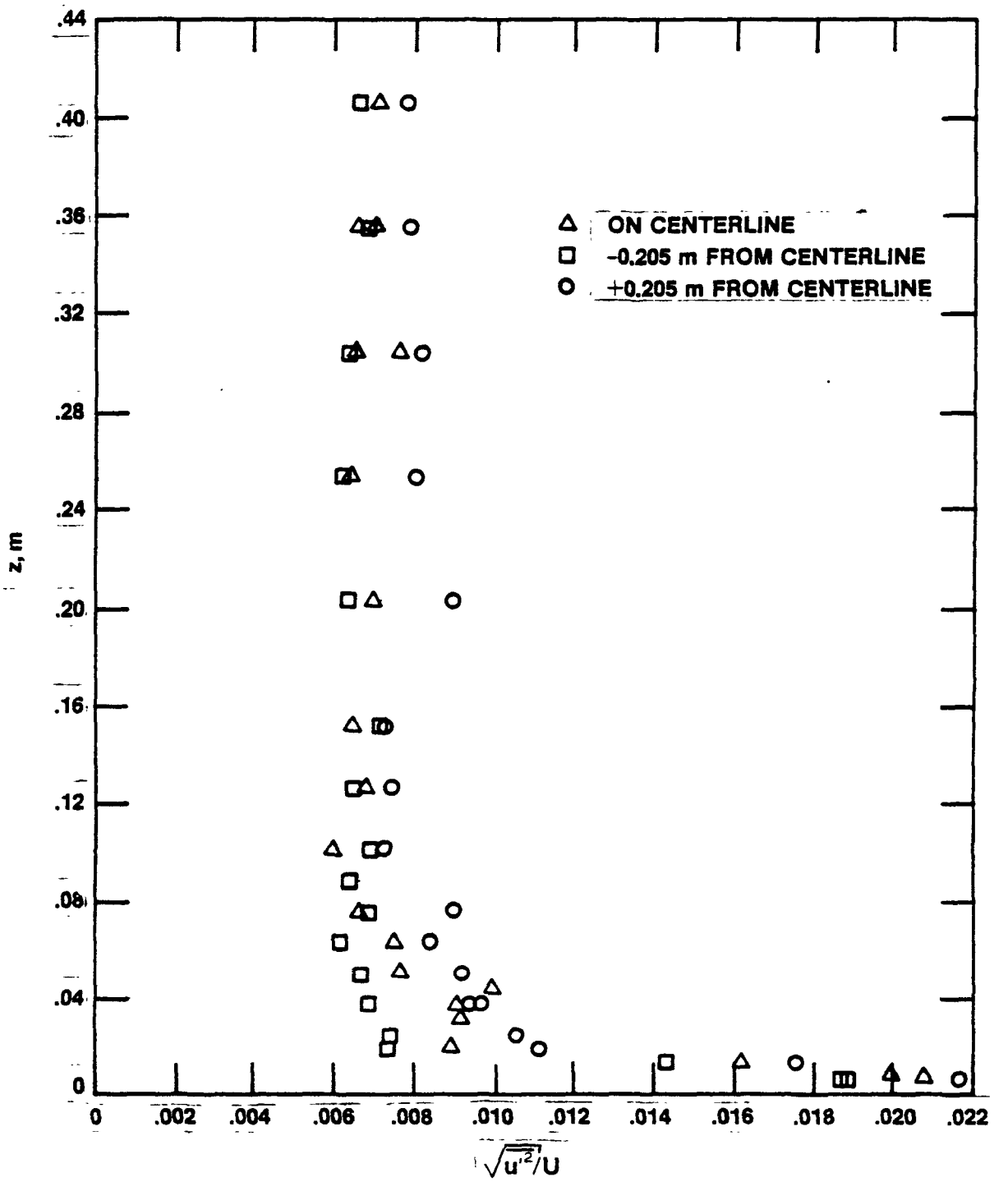

Figure 3.5. Empty tunnel, turbulence intensity profiles for three lateral positions at a distance of 1m from the test section entrance.

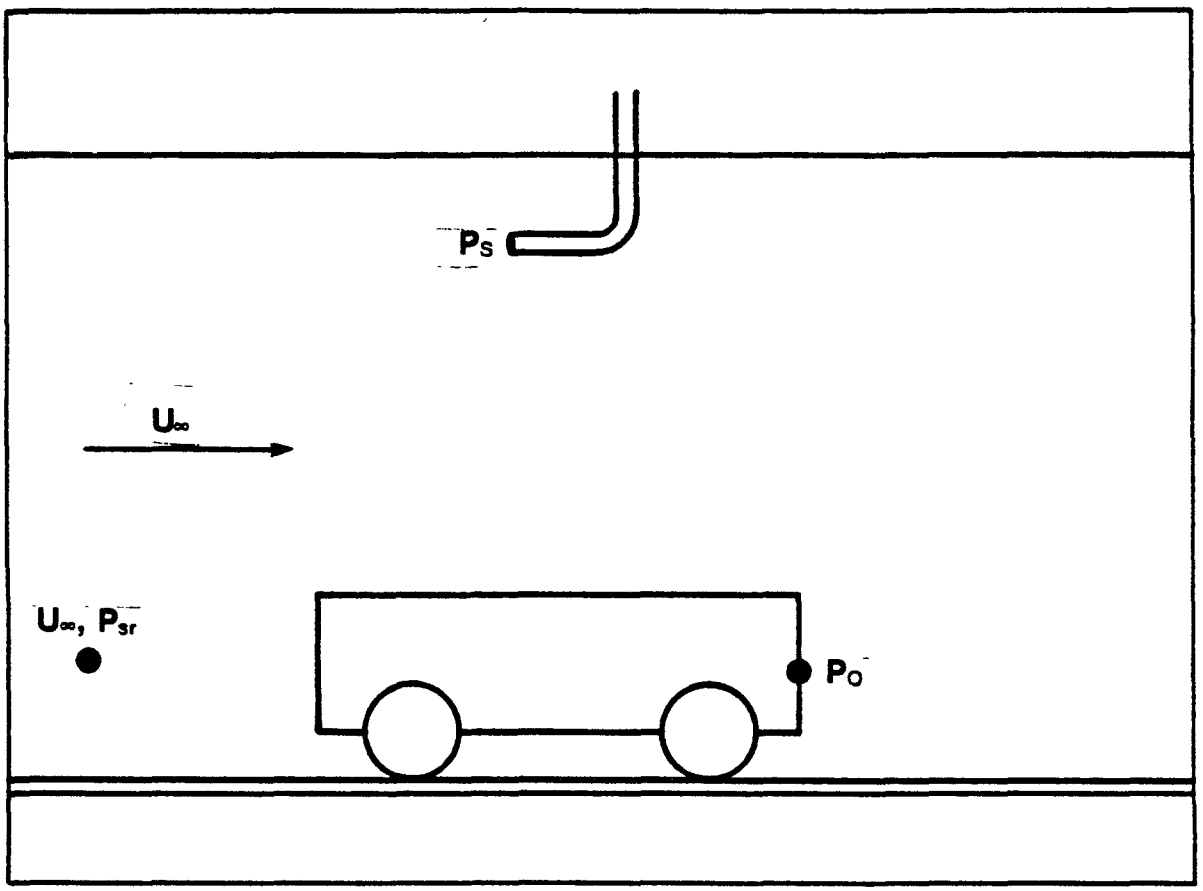

Figure 3.6. Locations of pressure measurements for determining blockage effects.

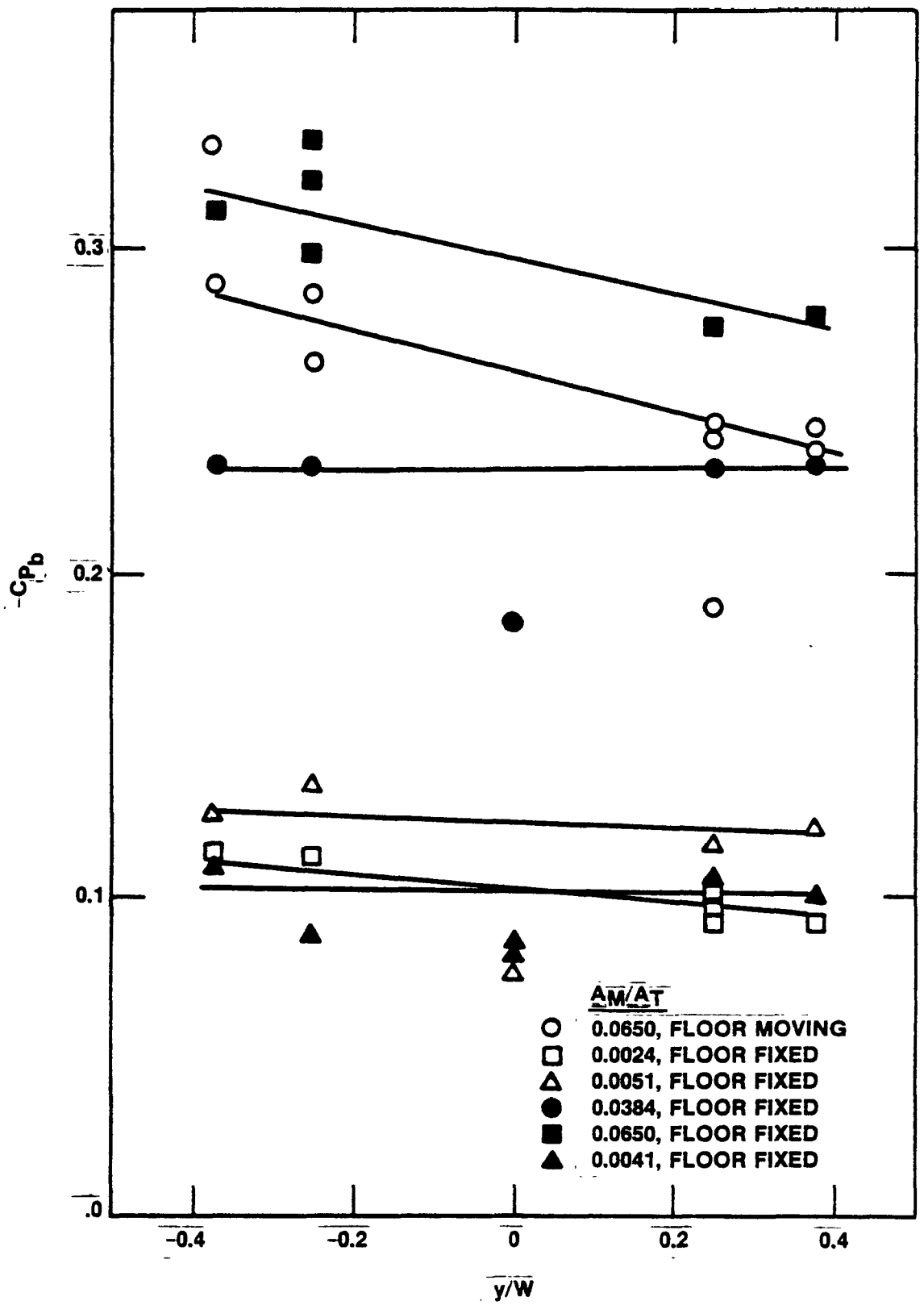

Figure 3.7. Spanwise variation on C_{P_b} for various blockage ratios, A_M/A_T.

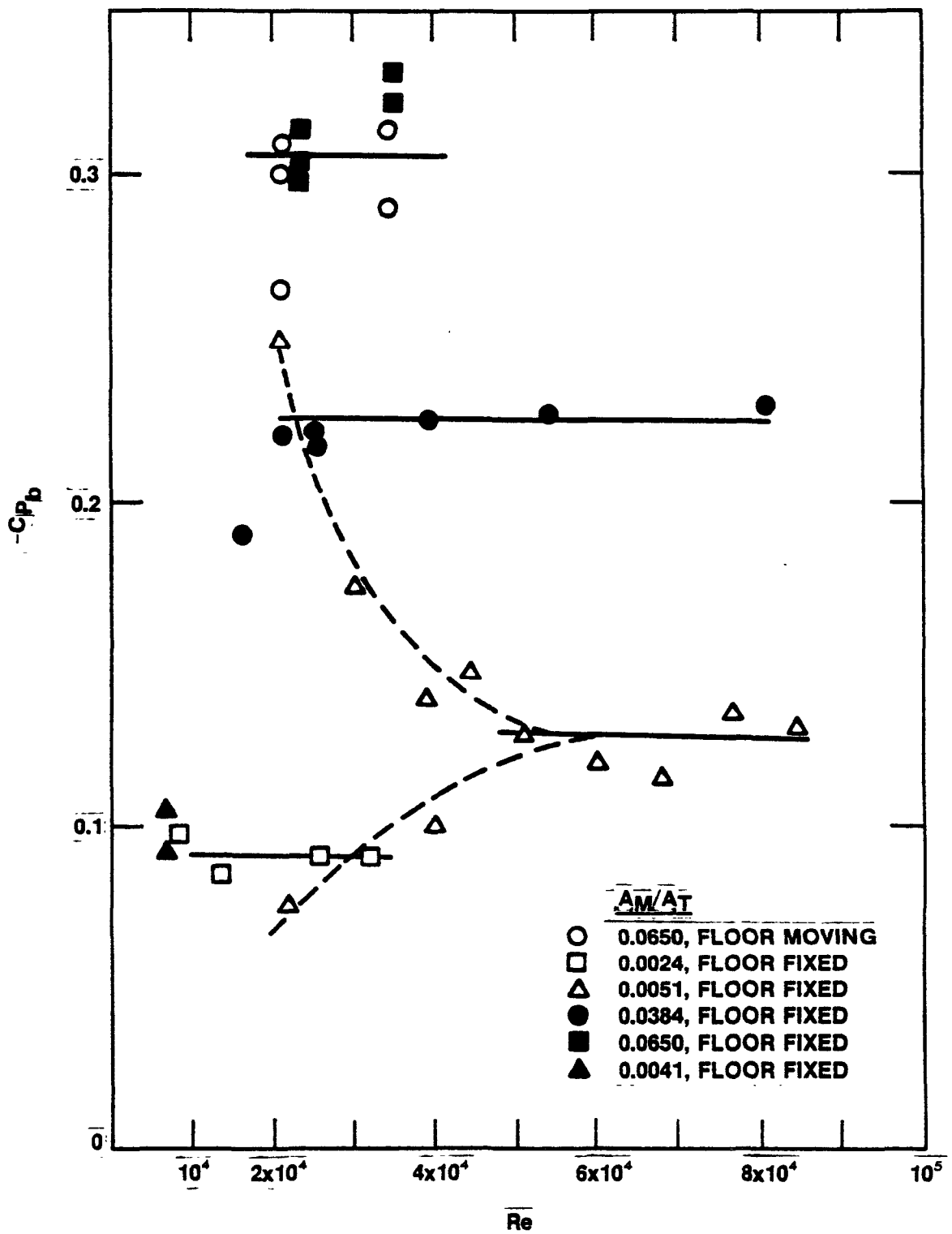

Figure 3.8. C_{P_b} as function of Reynolds number for various A_M/A_T.

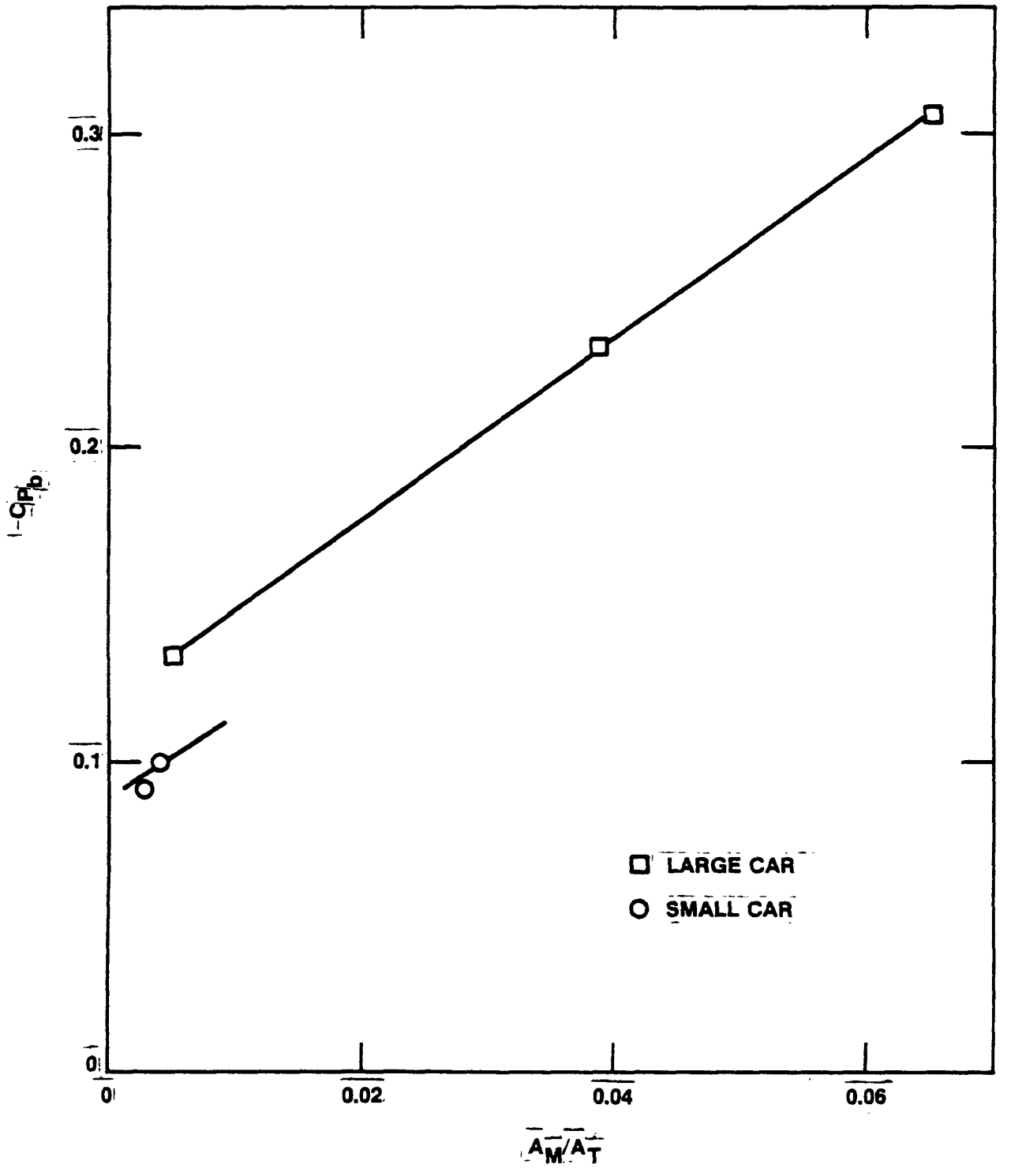

Figure 3.9. Variation of C_{P_b} with blockage ratio.

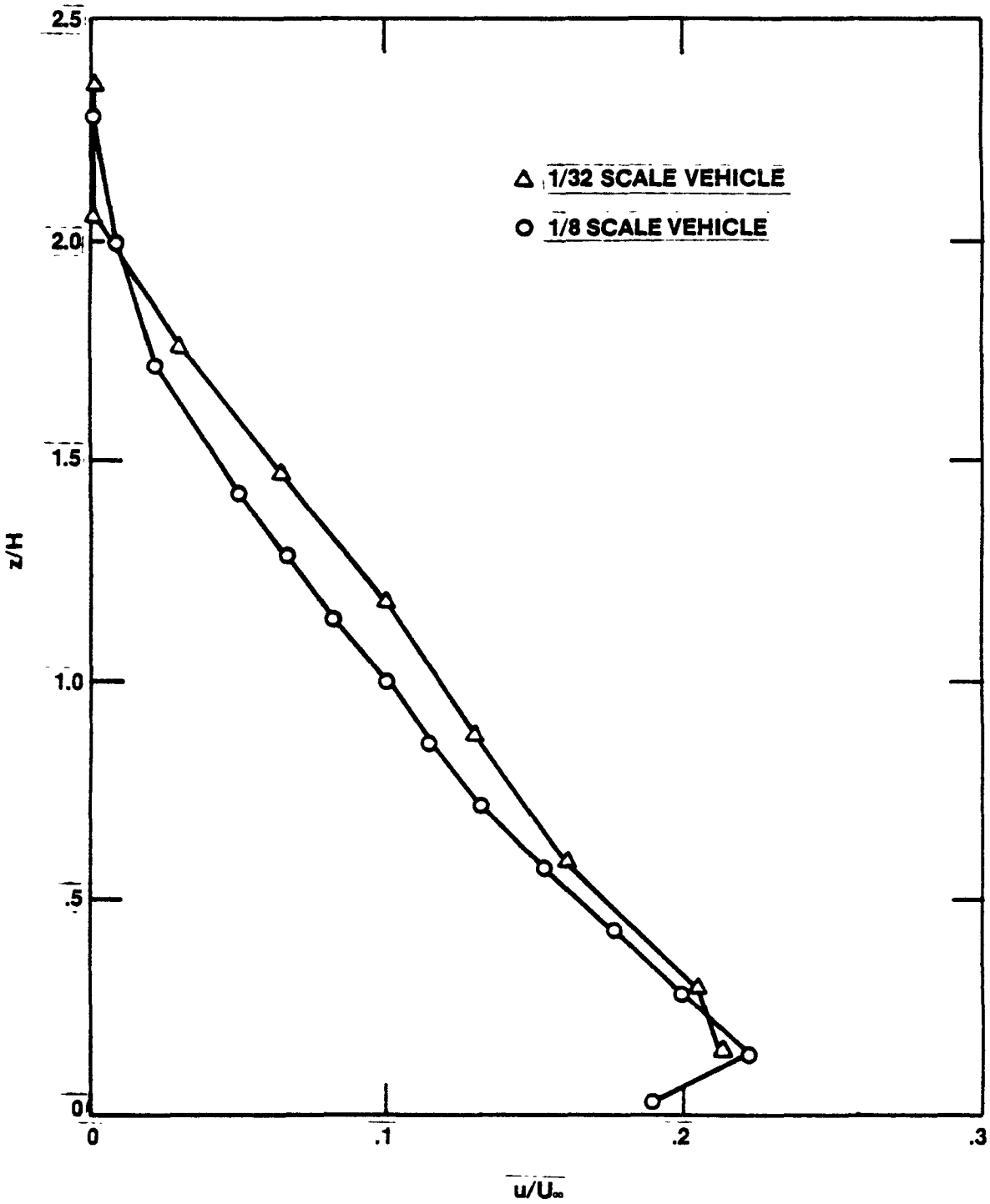

Figure 3.10. Vertical profiles of deficit velocity at x/H = 15, y = 0 for 1/8 and 1/32 scale vehicles.

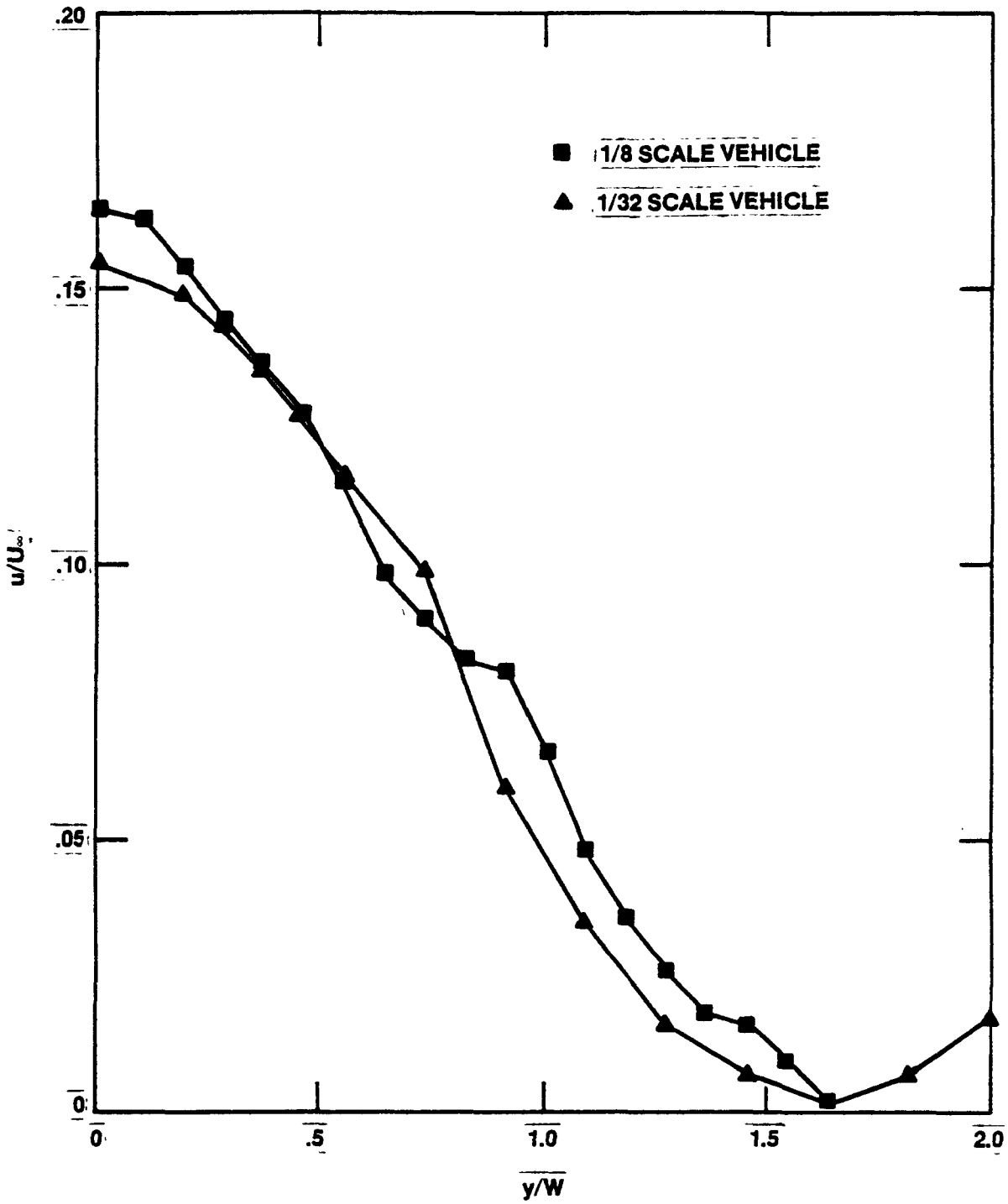

Figure 3.11. Lateral profiles of deficit velocity at x/H = 15, z/H = 0.5 for 1/8 and 1/32 scale vehicles.

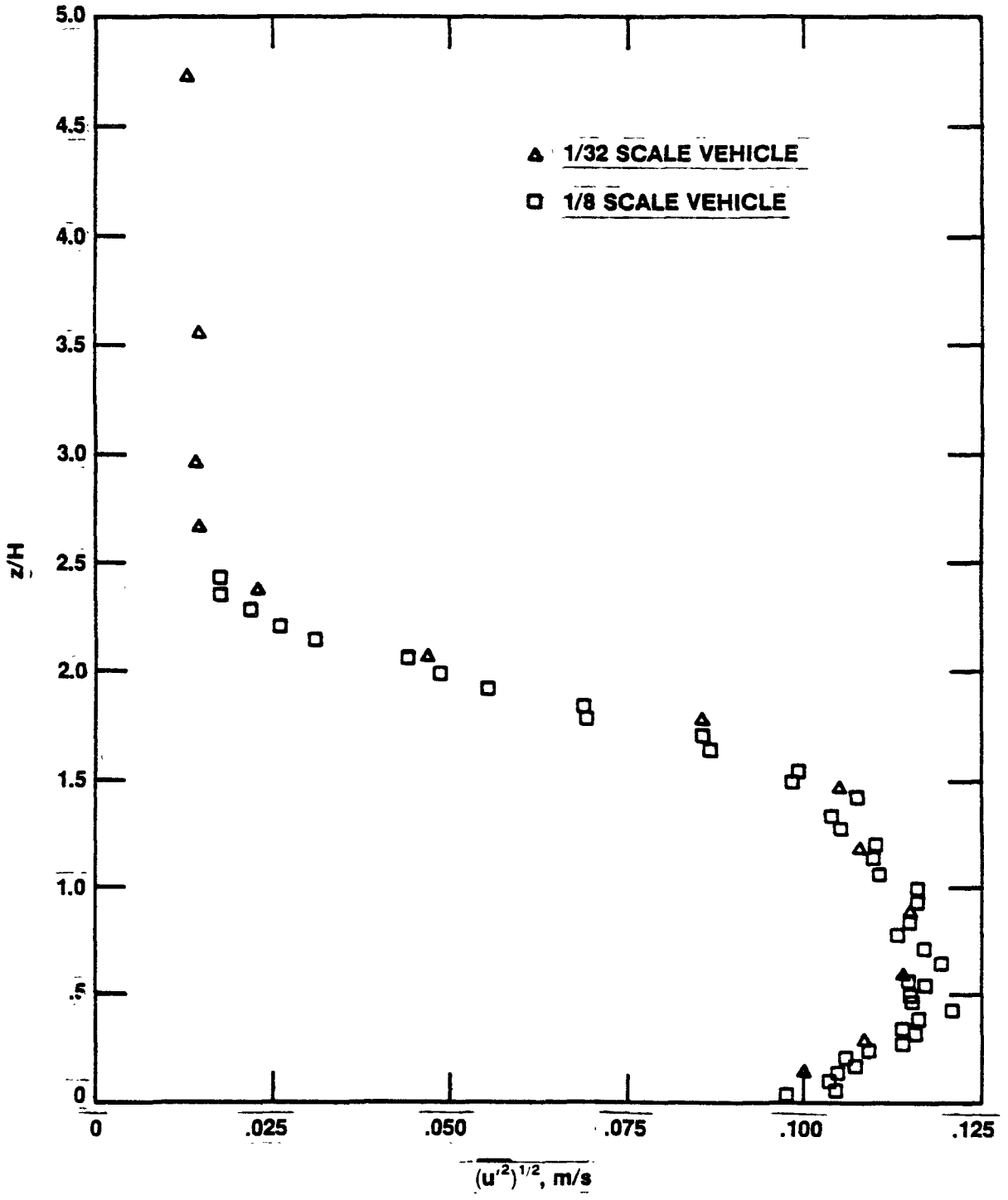

Figure 3.12. Vertical profiles of fluctuating velocity component at x/H = 15, y = 0 for 1/8 and 1/32 scale vehicles.

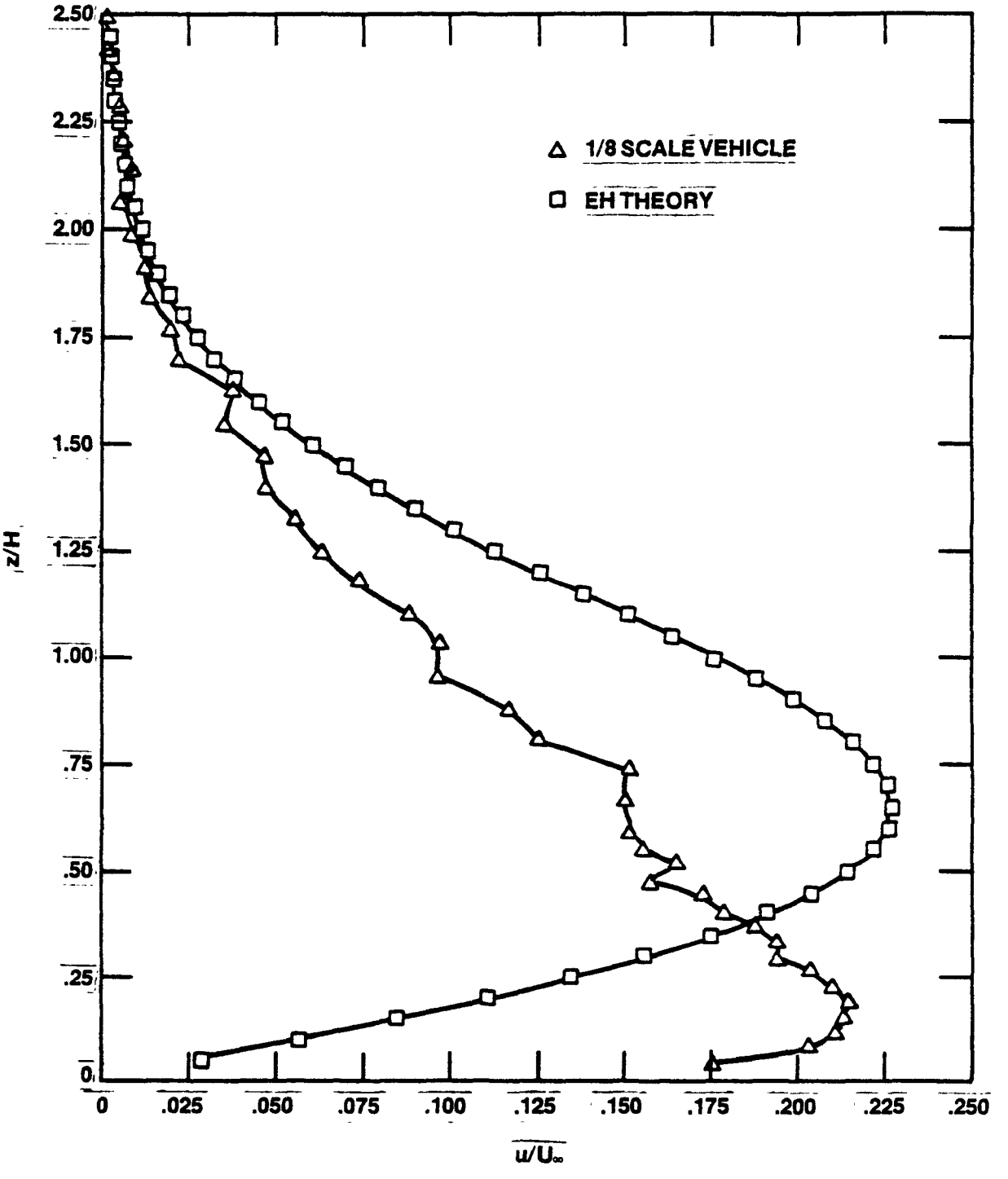

Figure 4.1. Vertical profile of velocity deficit at x/H = 15, y = 0 for 1/8 scale block vehicle and EH theory.

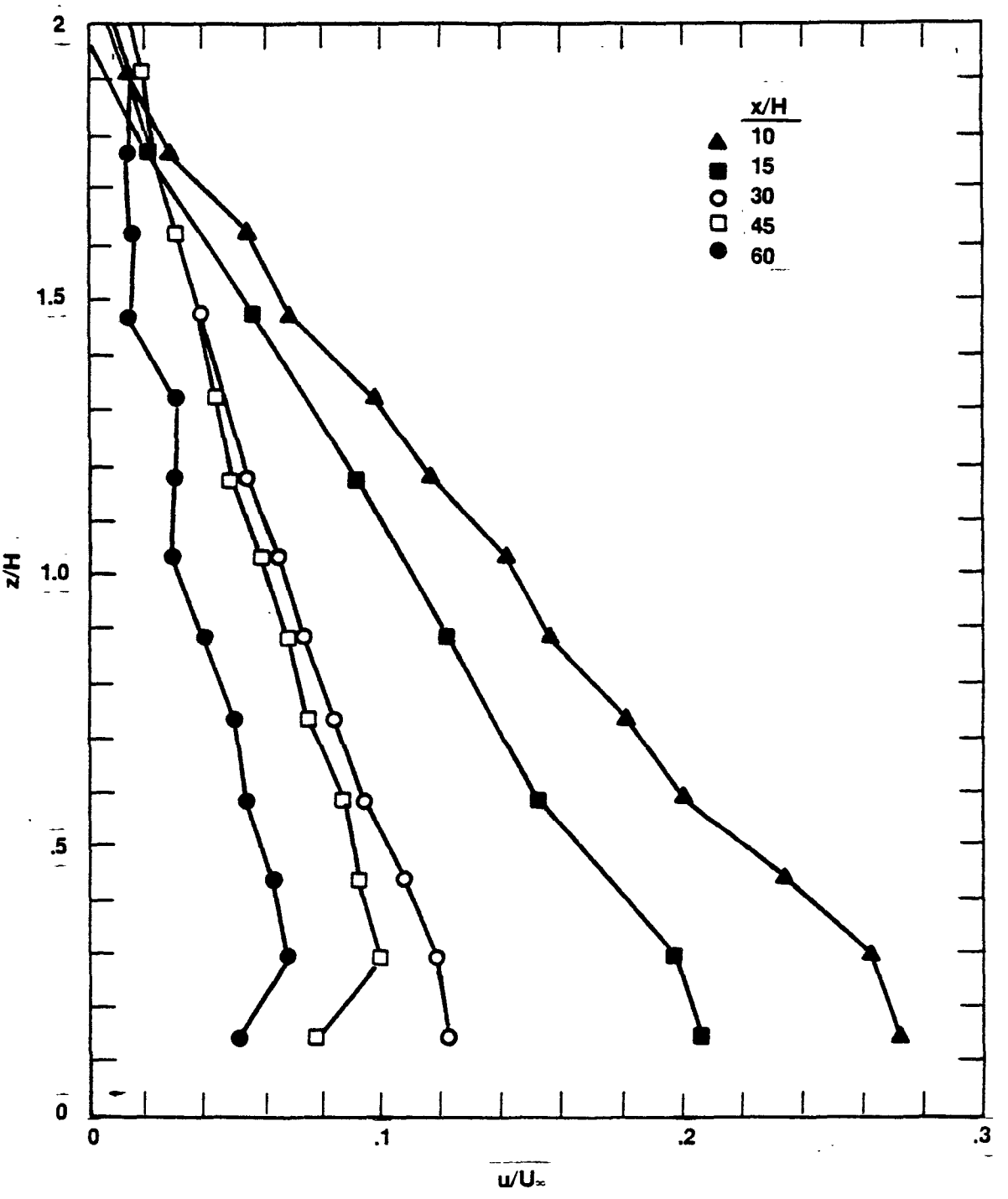

Figure 4.2. Vertical profiles of velocity deficit for 1/32 scale vehicle, y = 0.

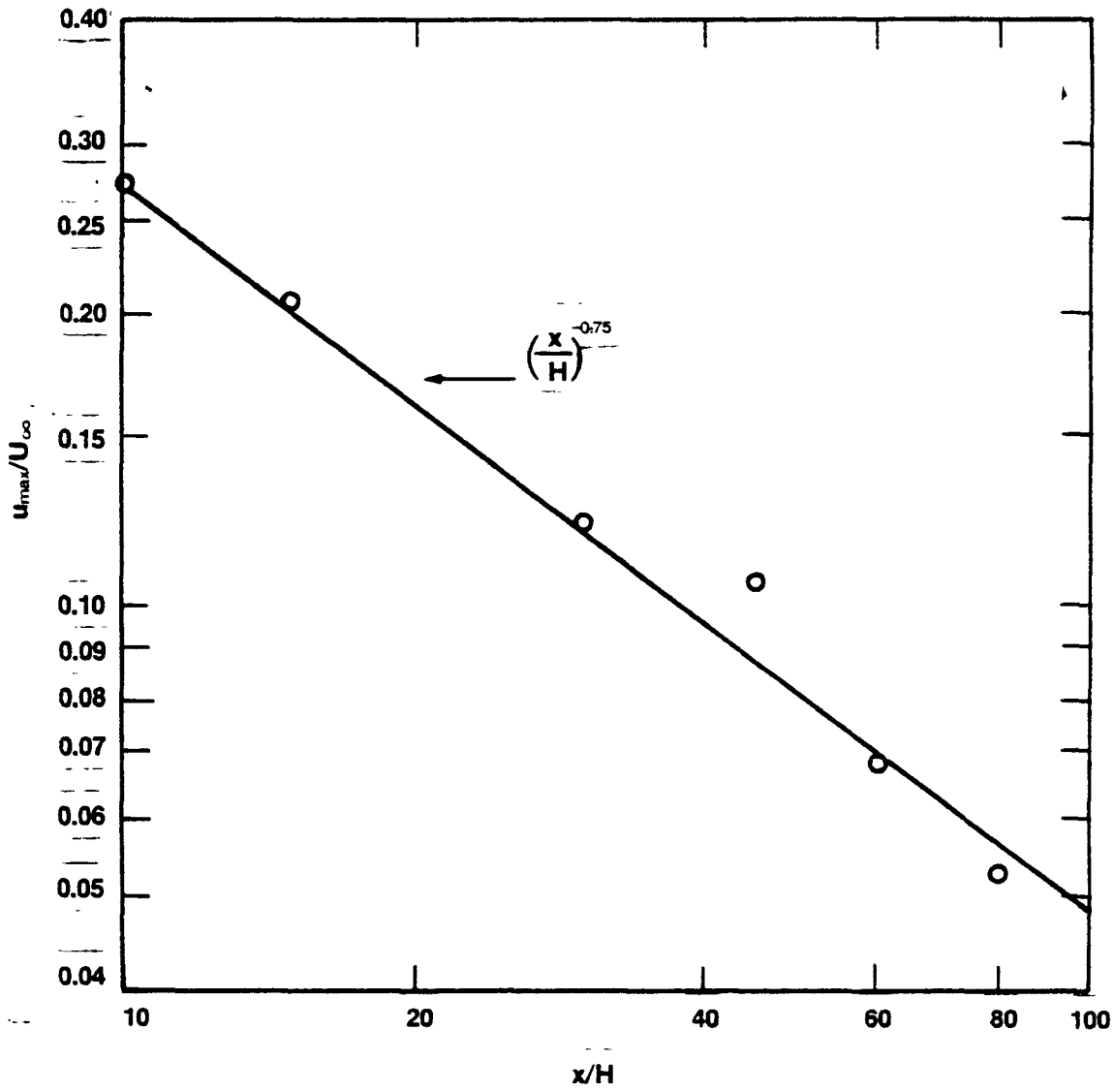

Figure 4.3. Decay of maximum velocity deficit with downwind distance.

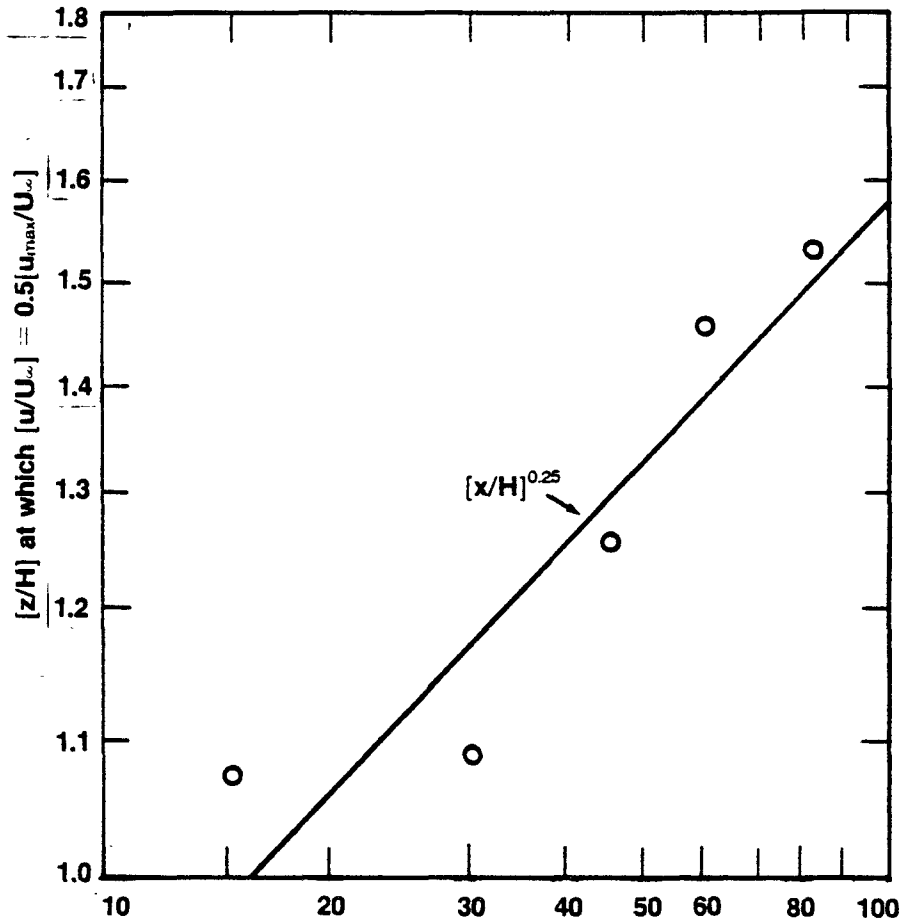

Figure 4.4 Rate of growth of the vertical length scale as determined from velocity profiles.

Figure 4.5. Smoke release showing slow growth of the wake.

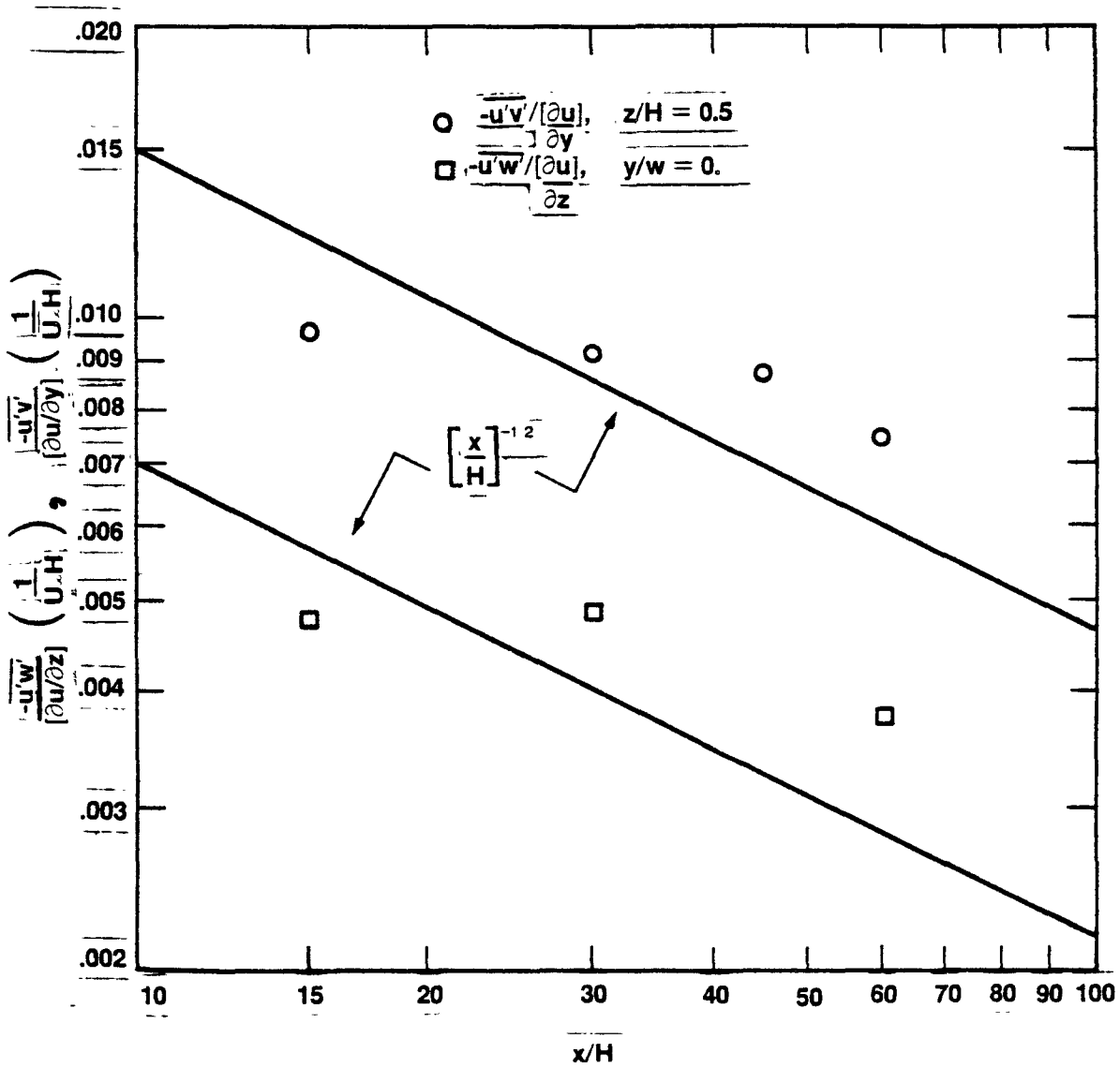

Figure 4.6 Measured Reynolds stress divided by velocity shear as a function of downwind distance.

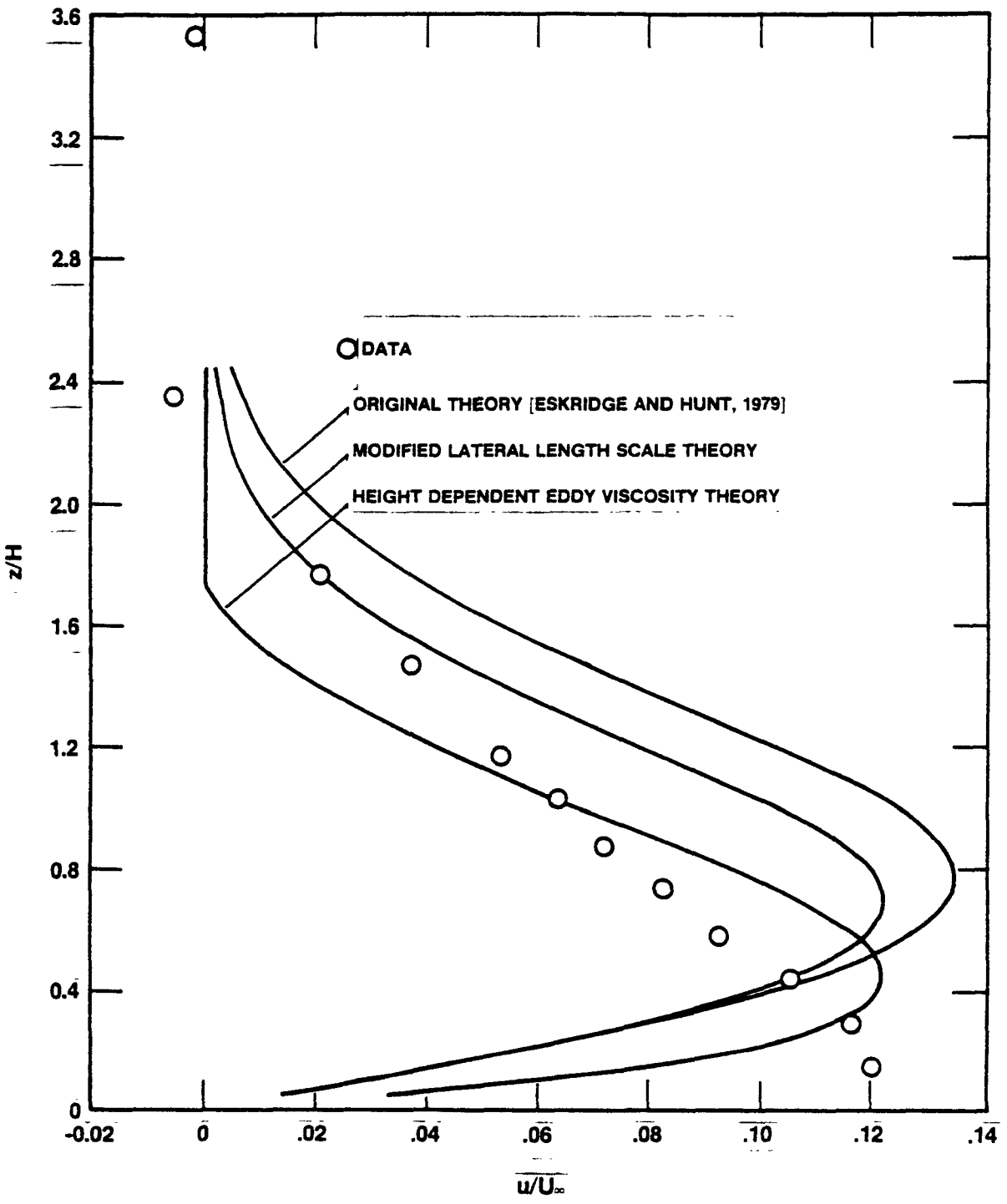

Figure 4.7. Theoretical curves and data for vertical profile of velocity deficit for x/H = 30 and y = 0.

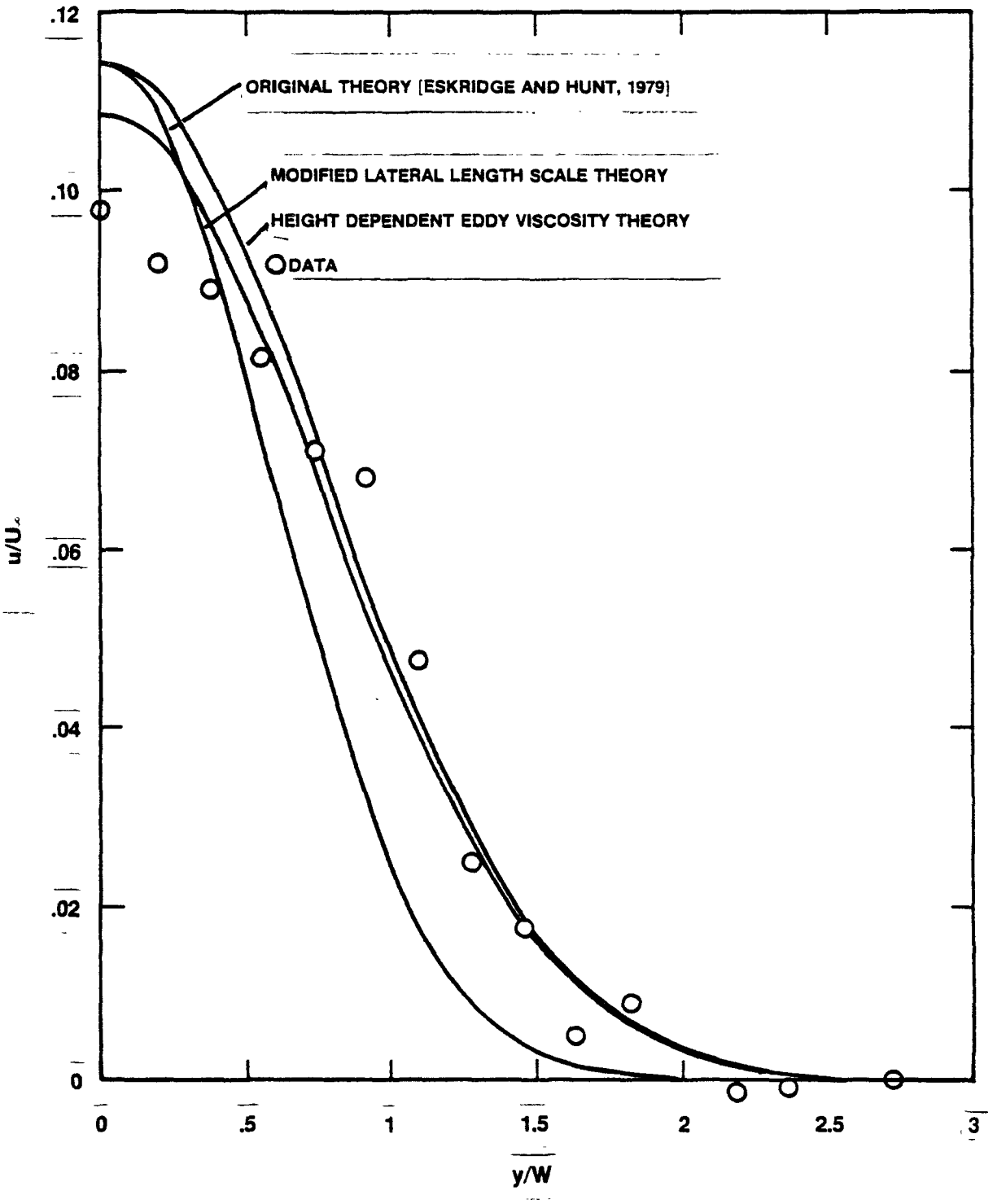

Figure 4.8. Theoretical curves and data for lateral profile of velocity deficit for x/H = 30 and z/H = 0.5.

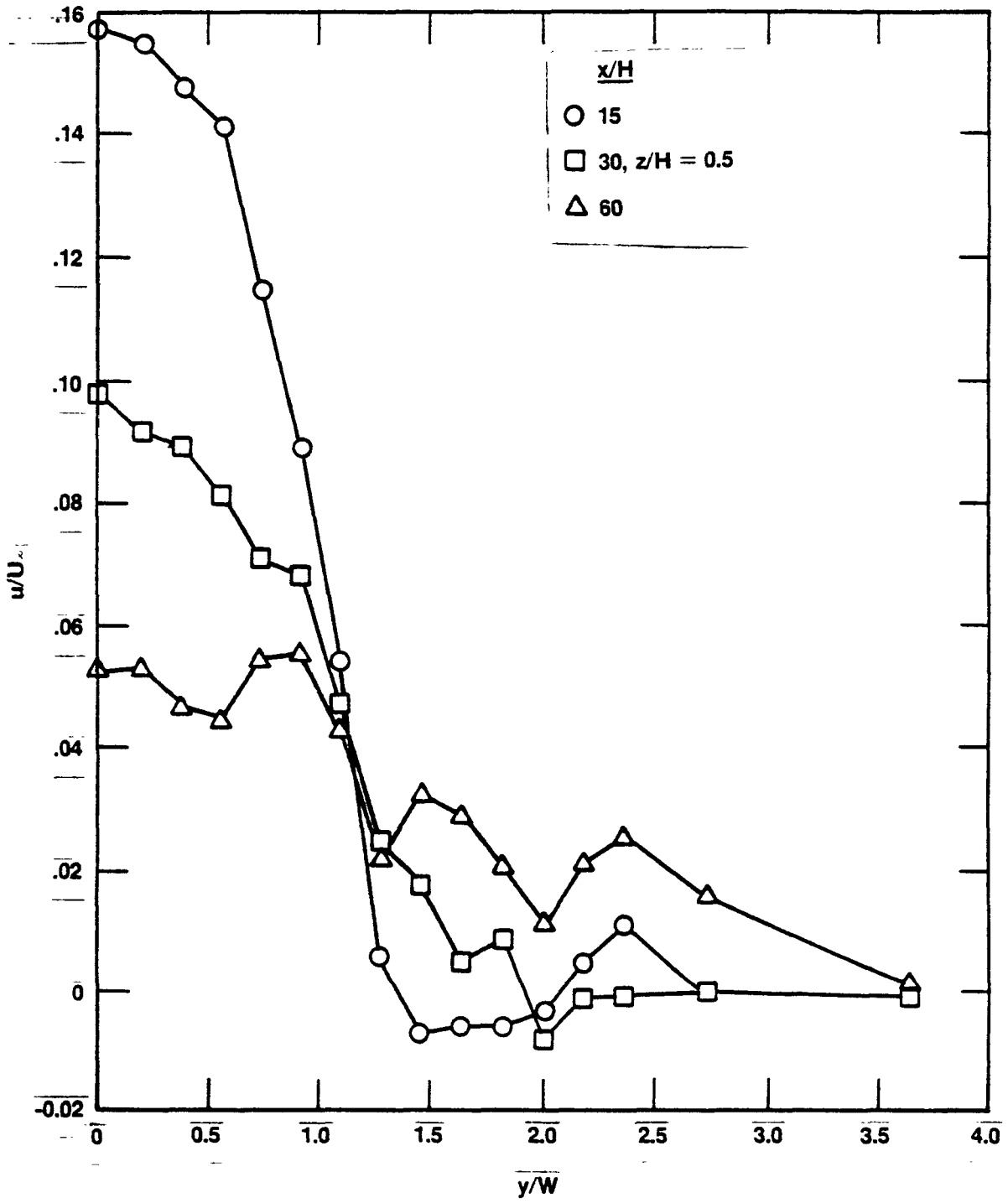

Figure 4.9. Lateral profile of velocity deficit at three longitudinal positions at constant ζ.

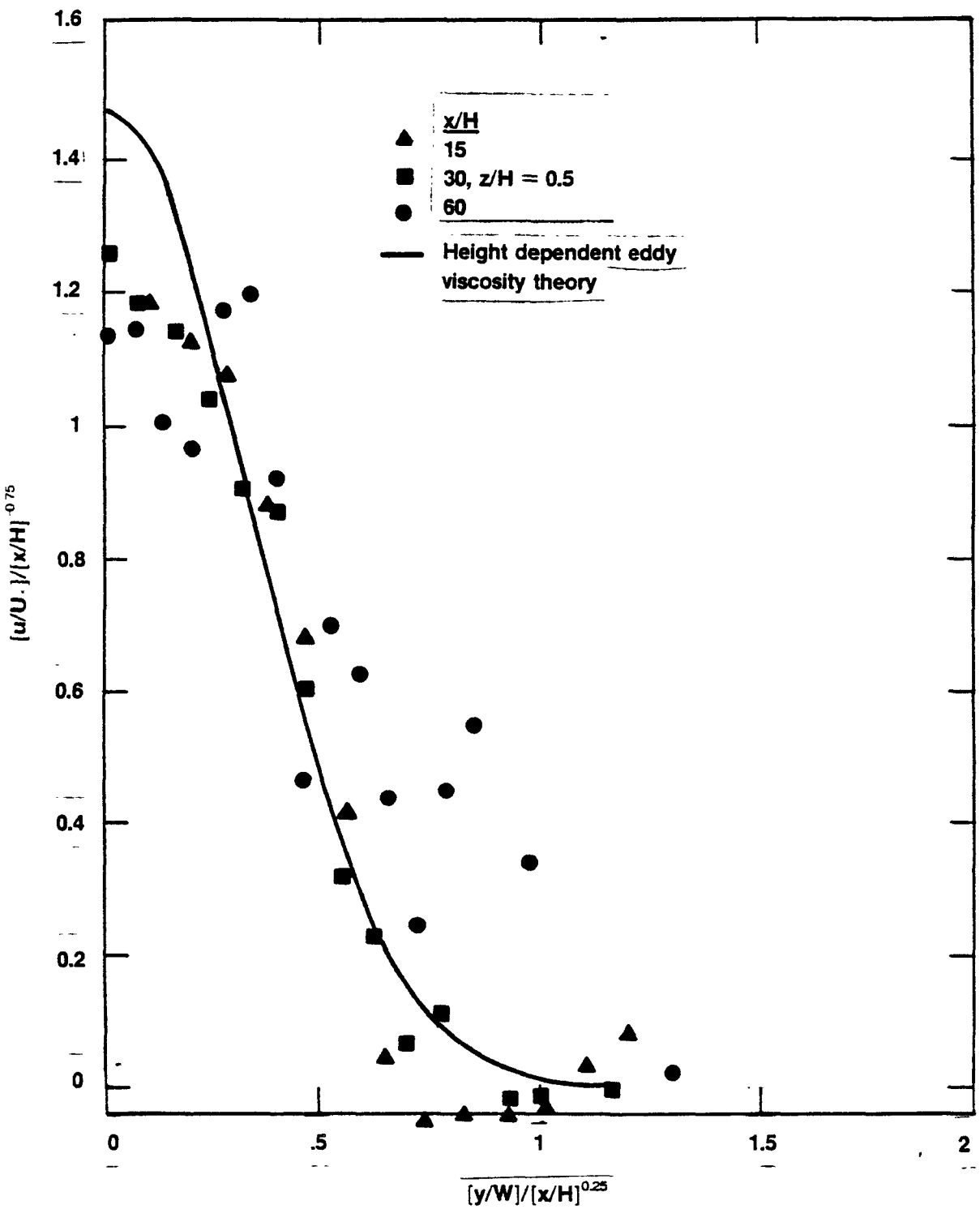

Figure 4.10. Theoretical curve and lateral profiles of velocity deficit at constant ζ using similarity coordinates.

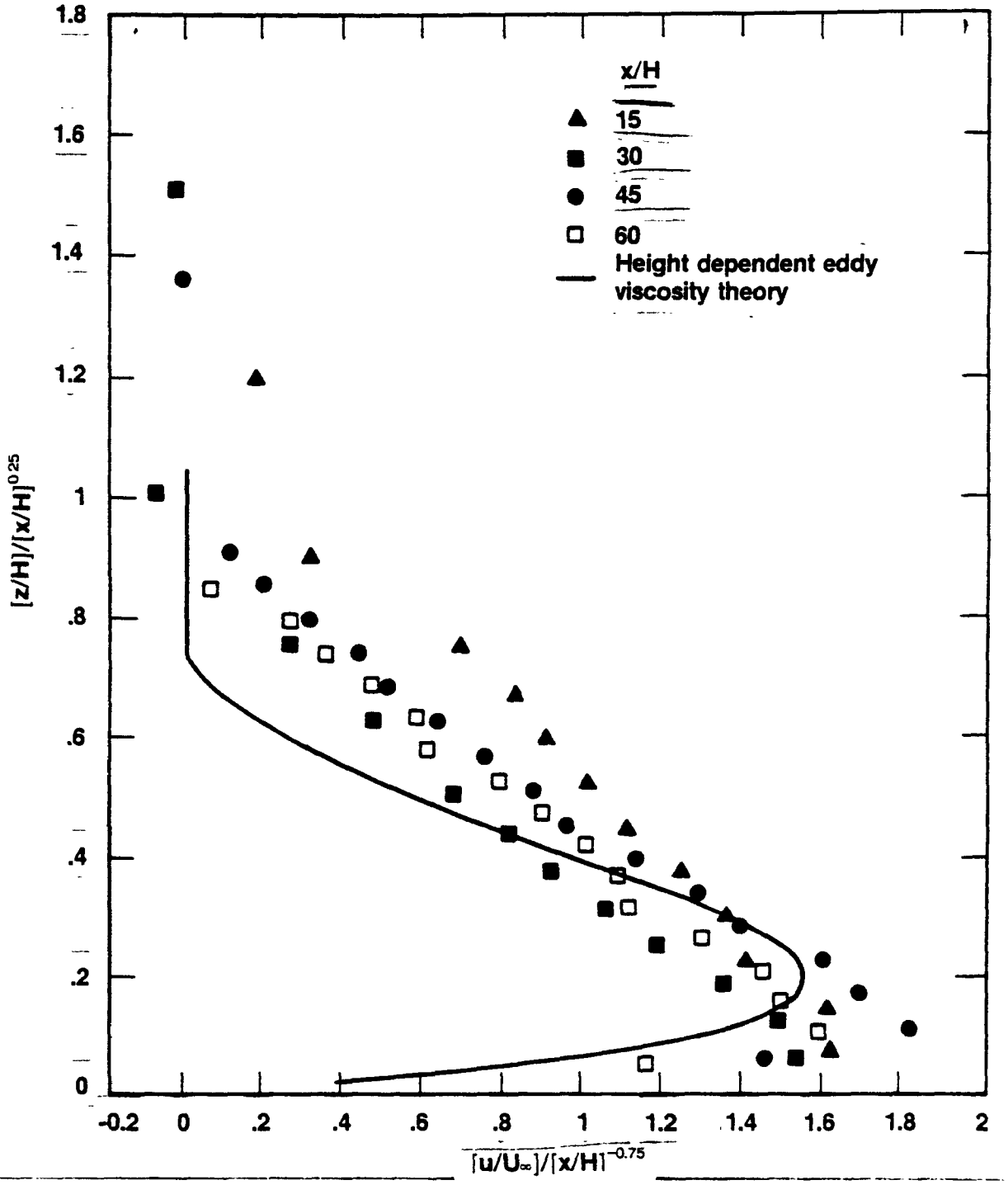

Figure 4.11. Theoretical curve and vertical profiles along centerline of velocity deficit using similarity coordinates.

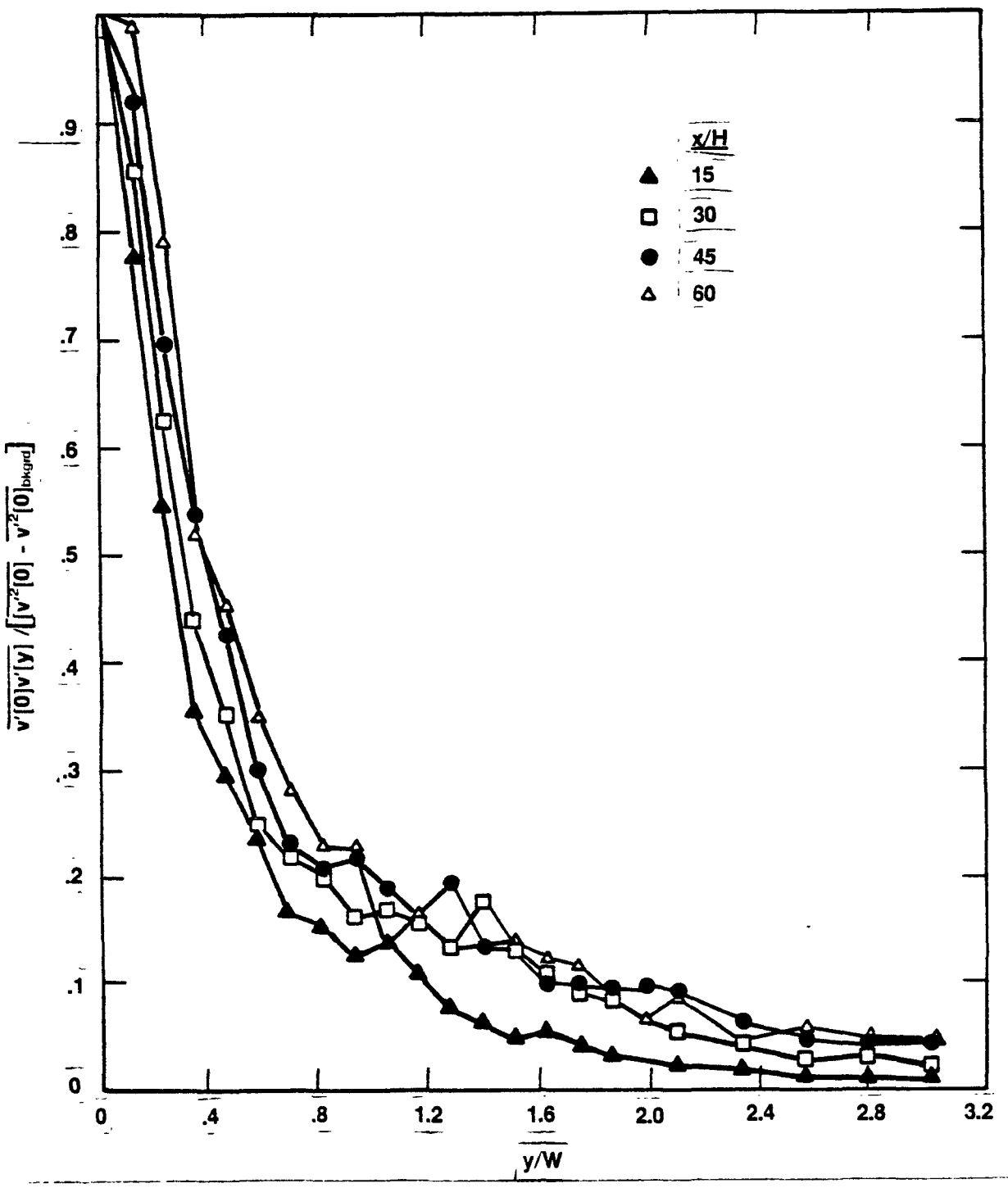

Figure 4.12. Lateral variation of the correlation of the fluctuating velocity component, v'.

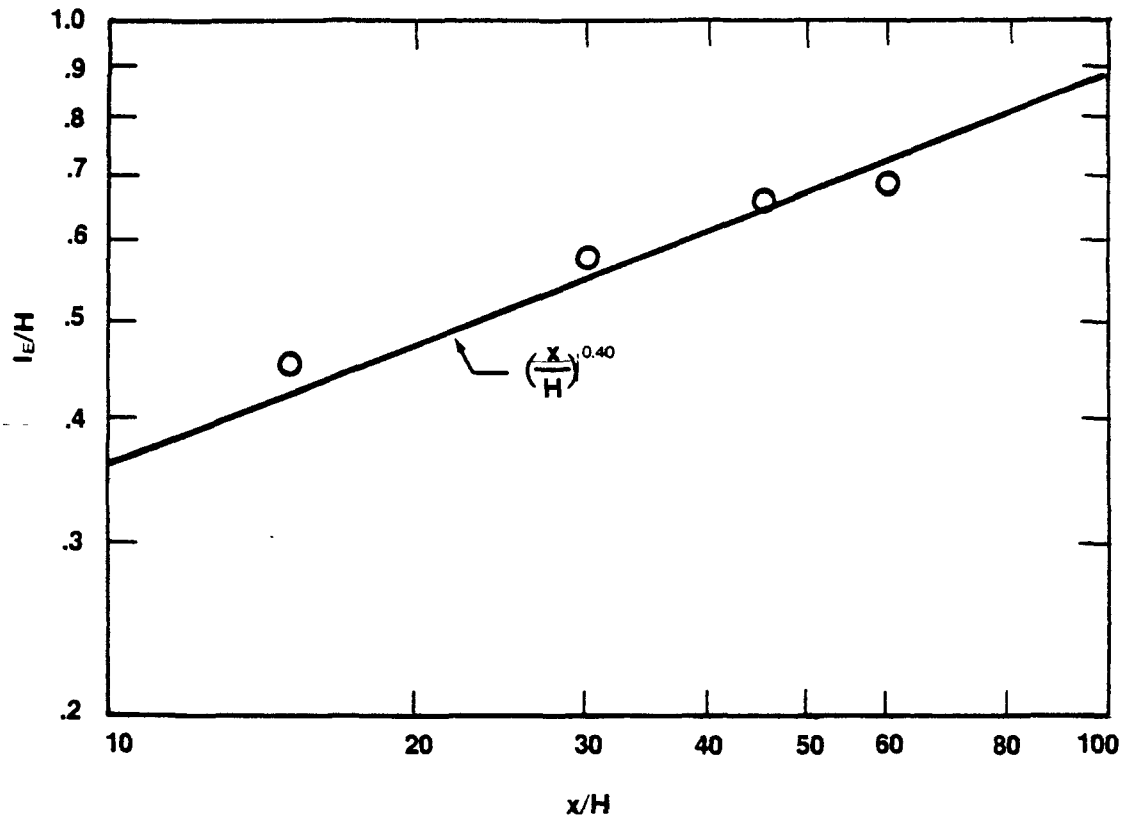

Figure 4.13. Length scale determined from fluctuating velocity component, v'.

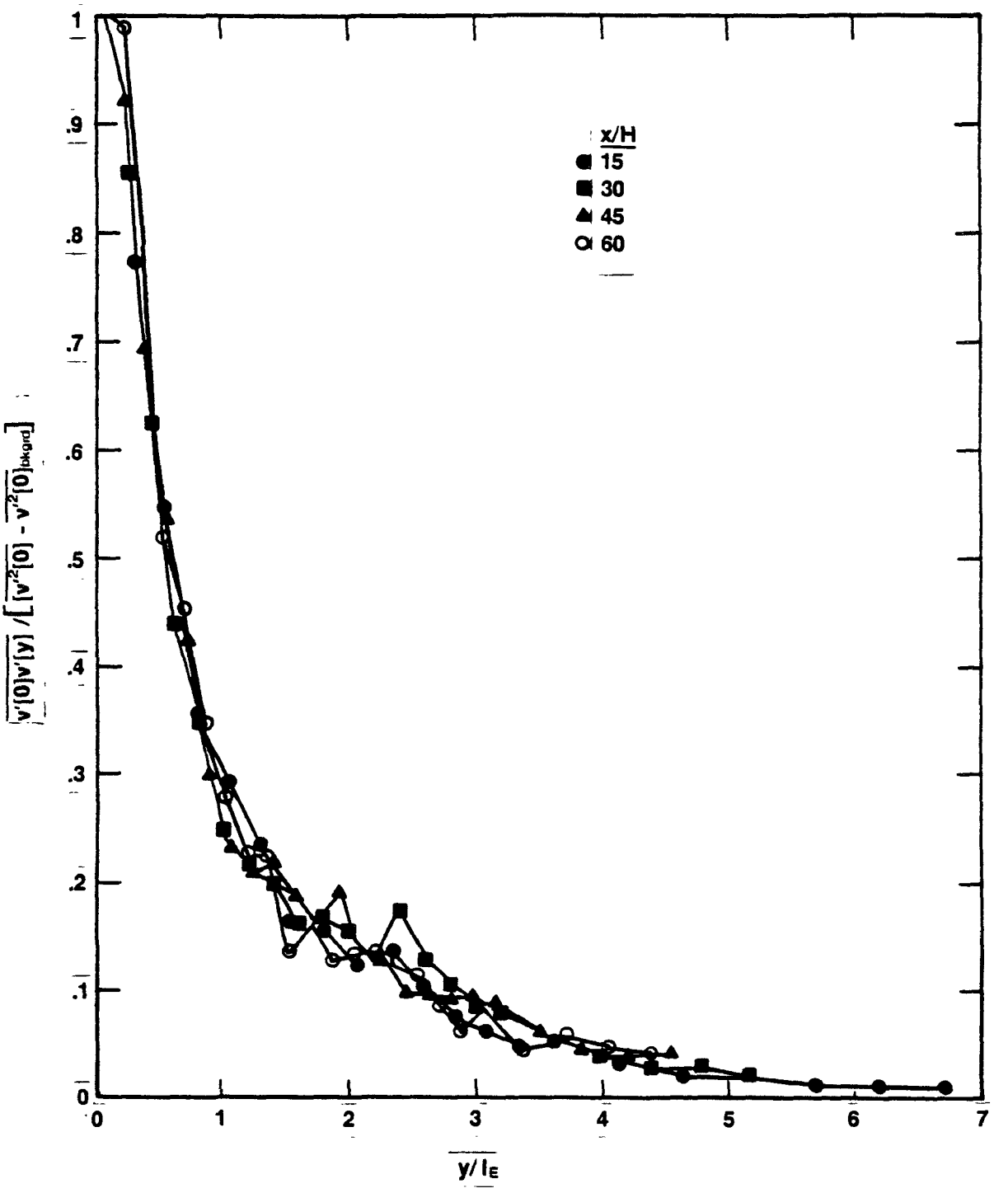

Figure 4.14. Correlation of the fluctuating velocity component in similarity coordinates.

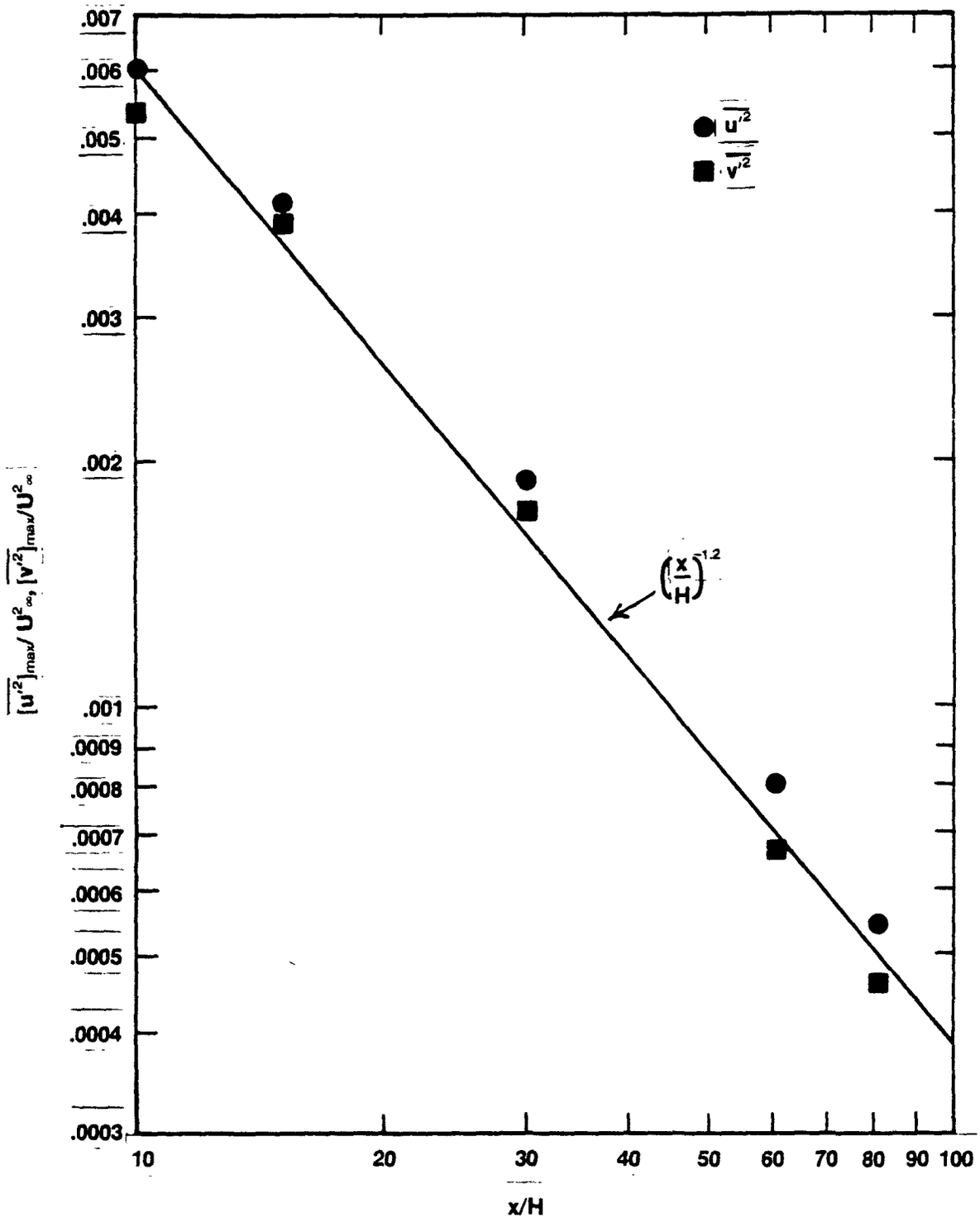

Figure 4.15. Longitudinal variation of the maximum values of the turbulent kinetic energy components $\overline{u'^2}$ and $\overline{v'^2}$ together with least squares linear fit.

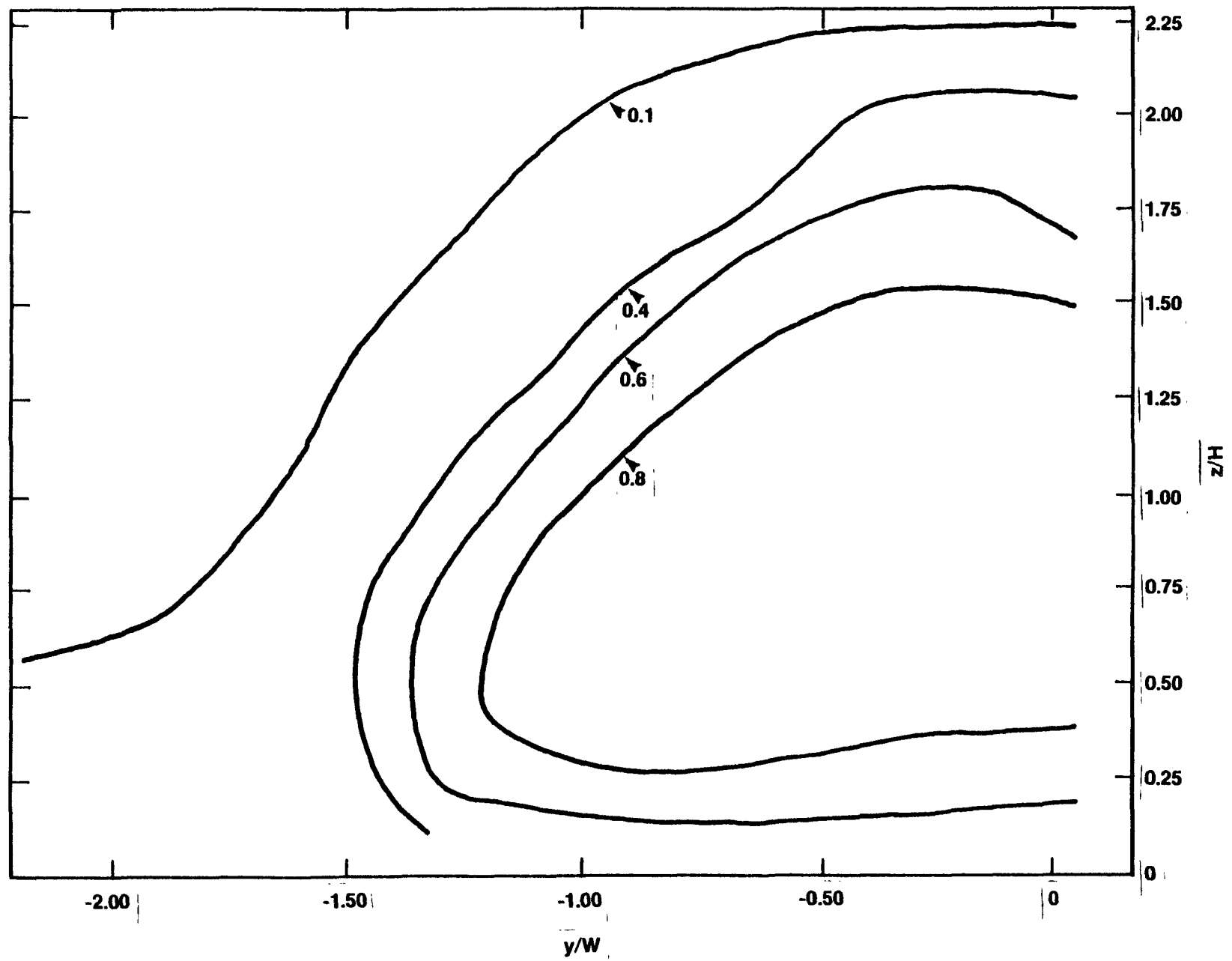

Figure 4.16. Cross-section of normalized turbulent kinetic energy component $\overline{u'^2}$ with analyzed isolines of the distribution at x/H = 30.

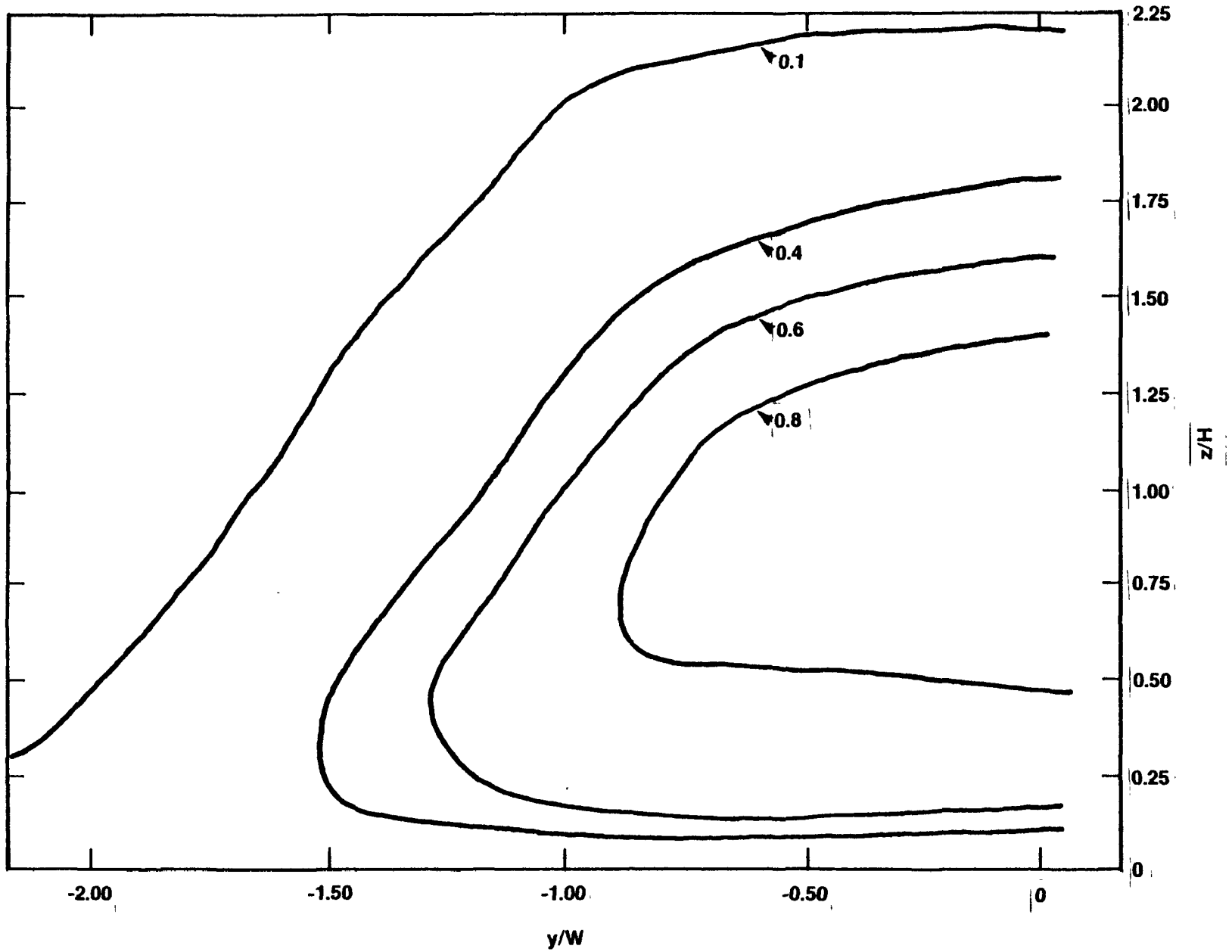

Figure 4.17. Cross-section of normalized turbulent kinetic energy component $\overline{v'^2}$ with analyzed isolines of the distribution at x/H = 30.

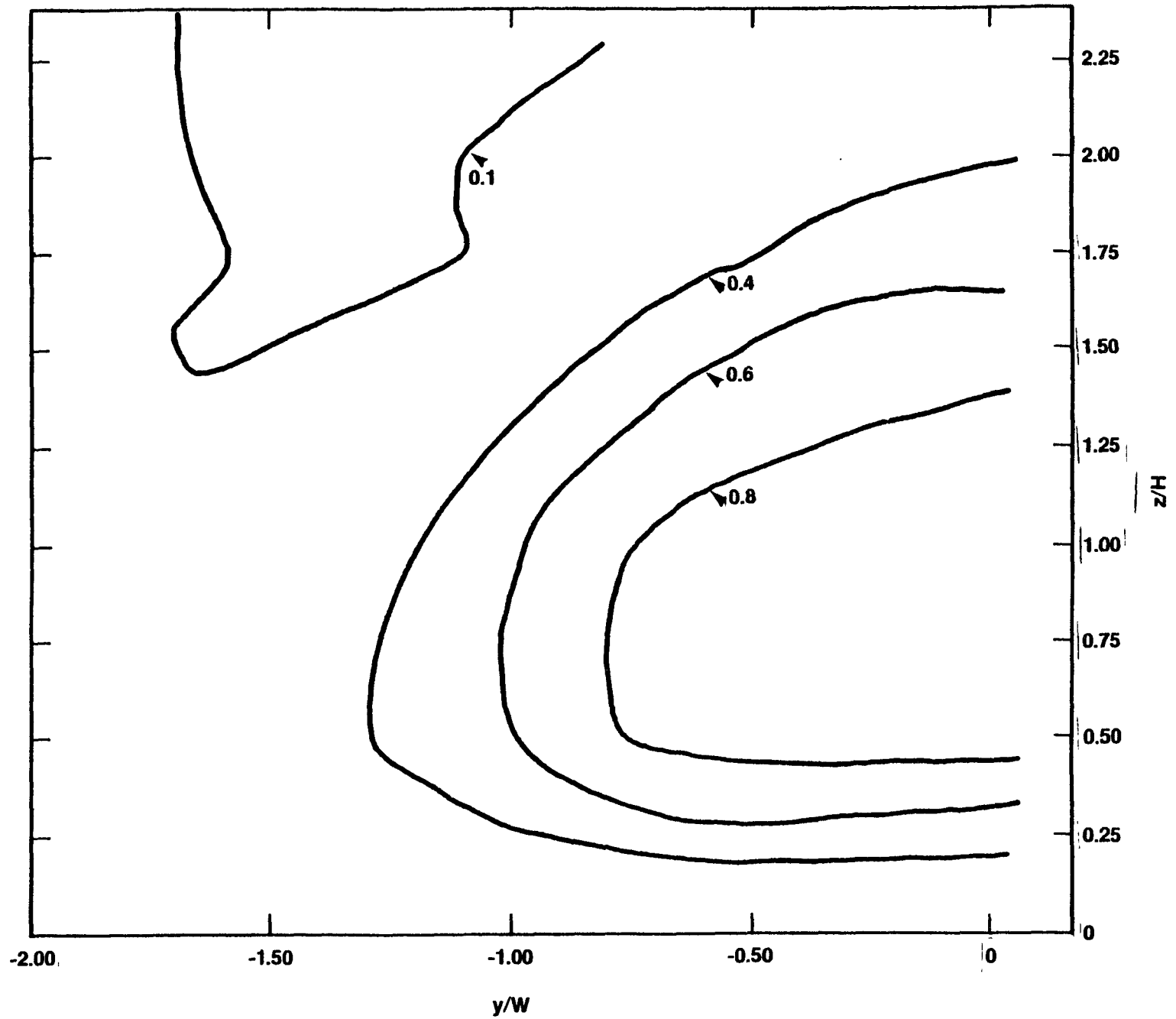

Figure 4.18. Cross-section of normalized turbulent kinetic energy component $\overline{w'^2}$ with analyzed isolines of the distribution at x/H = 30.

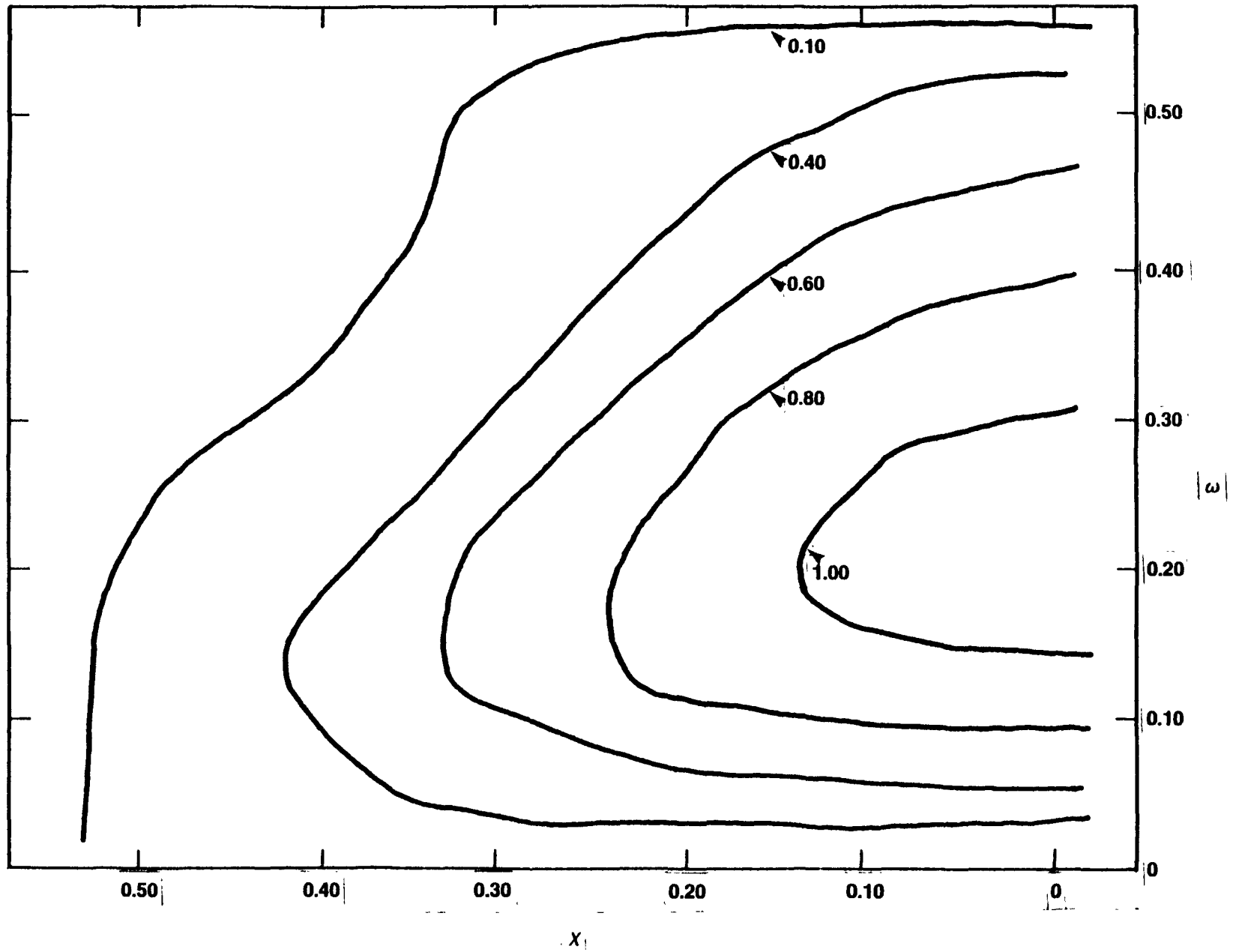

Figure 4.19. Cross-section of F_C $[\chi,\omega]$ with analyzed isolines of the distribution of F_C.

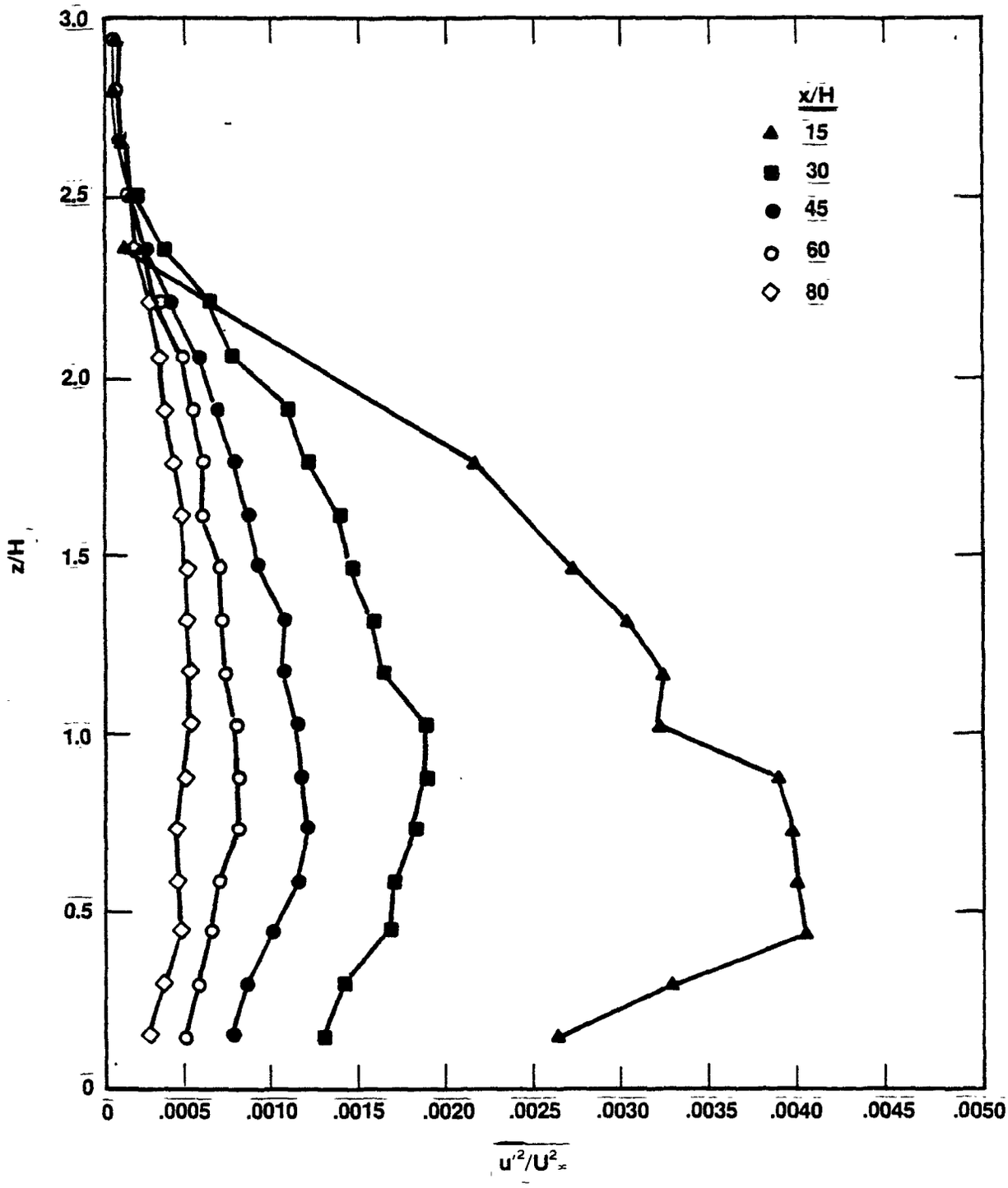

Figure 4.20a. Measured centerline vertical of the turbulent kinetic energy component $\overline{u'^2}$ at various downwind distances.

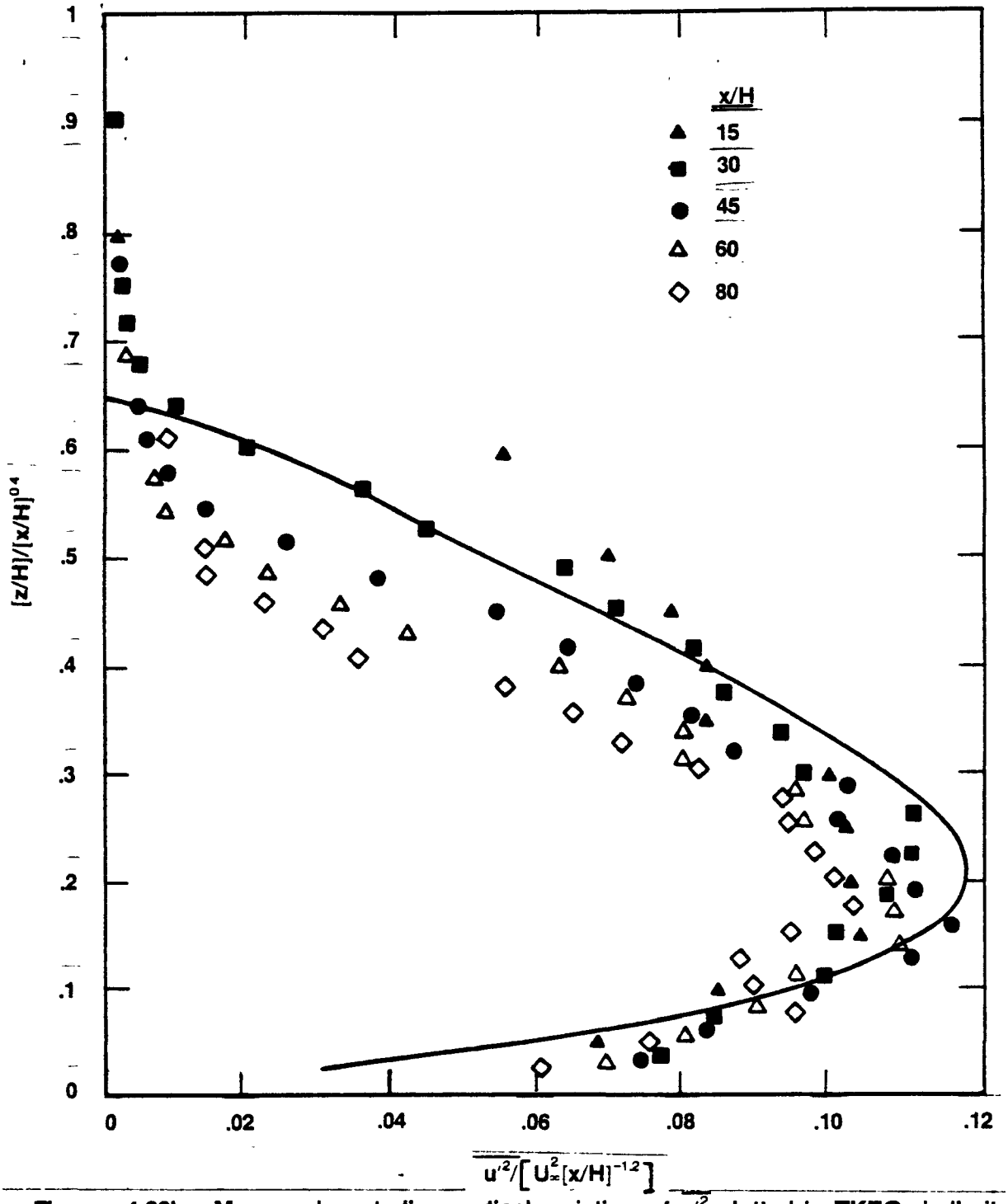

Figures 4.20b. Measured centerline vertical variation of $\overline{u'^2}$ plotted in TKEC similarity variables compared to eq. 4.21 [solid line].

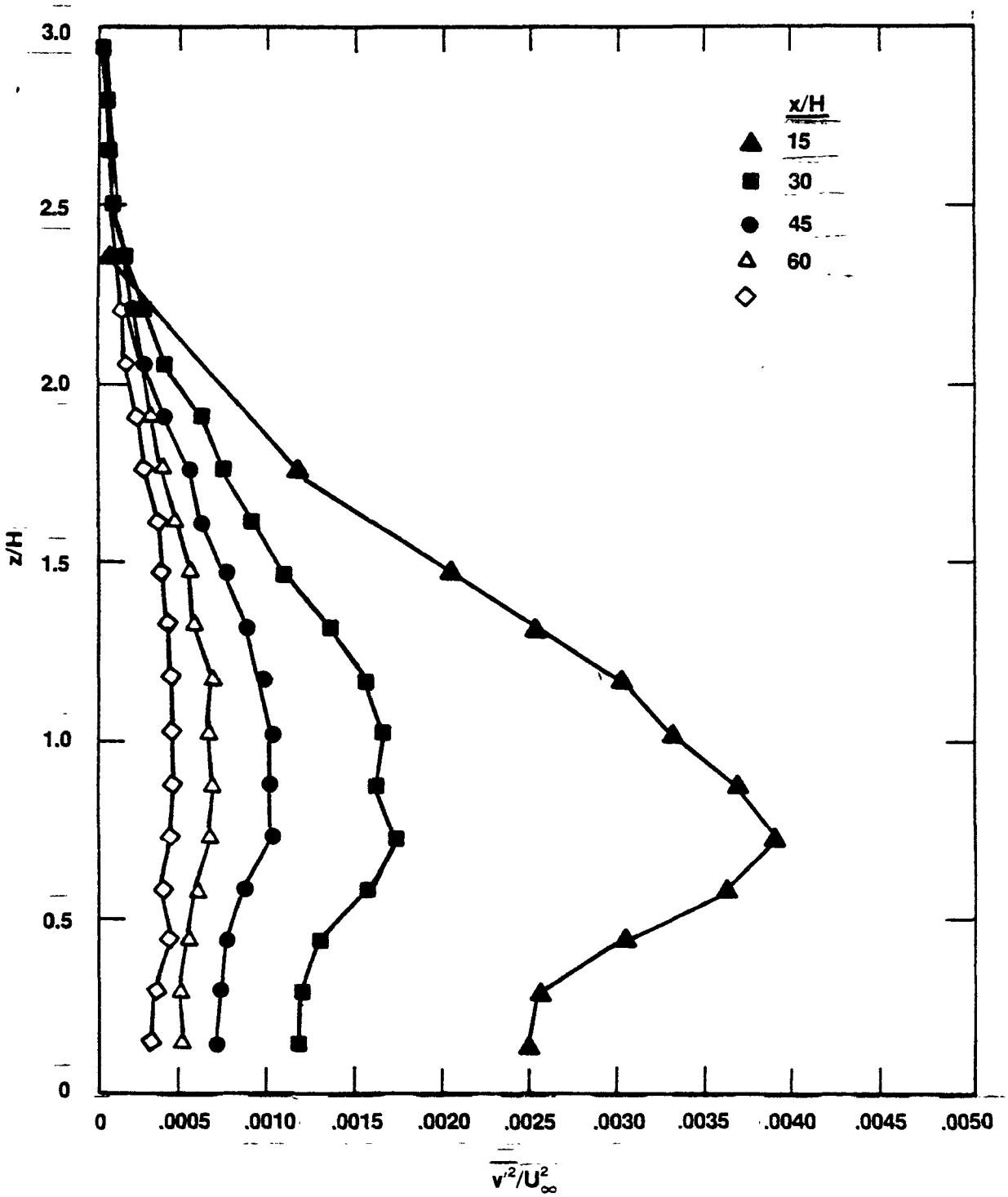

Figure 4.21a. Measured centerline vertical variation of the turbulent kinetic energy component $\overline{v'^2}$ at various downwind distances.

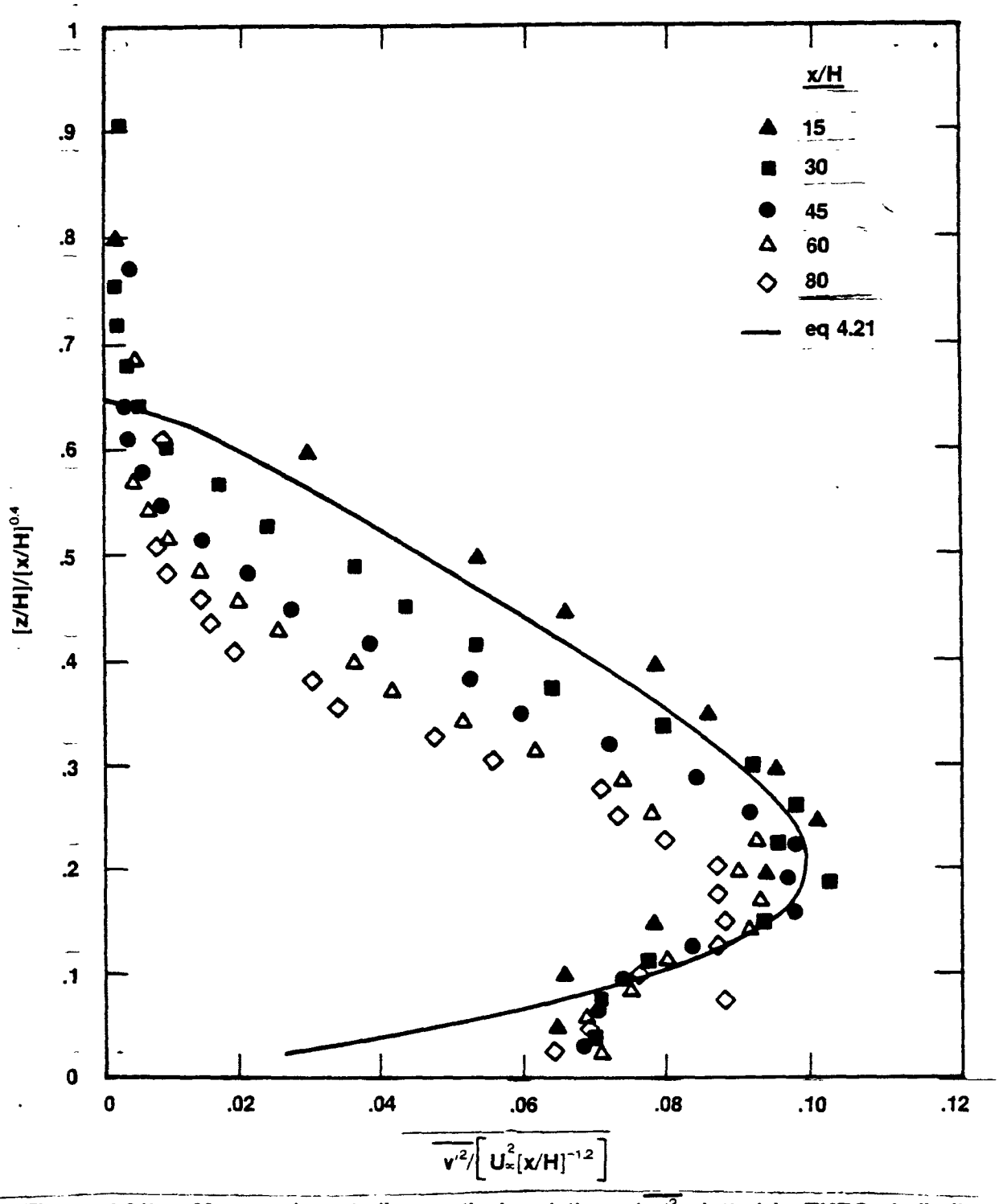

Figure 4.21b. Measured centerline vertical variation of $\overline{v'^2}$ plotted in TKEC similarity variables compared to eq. 4.21 [solid line].

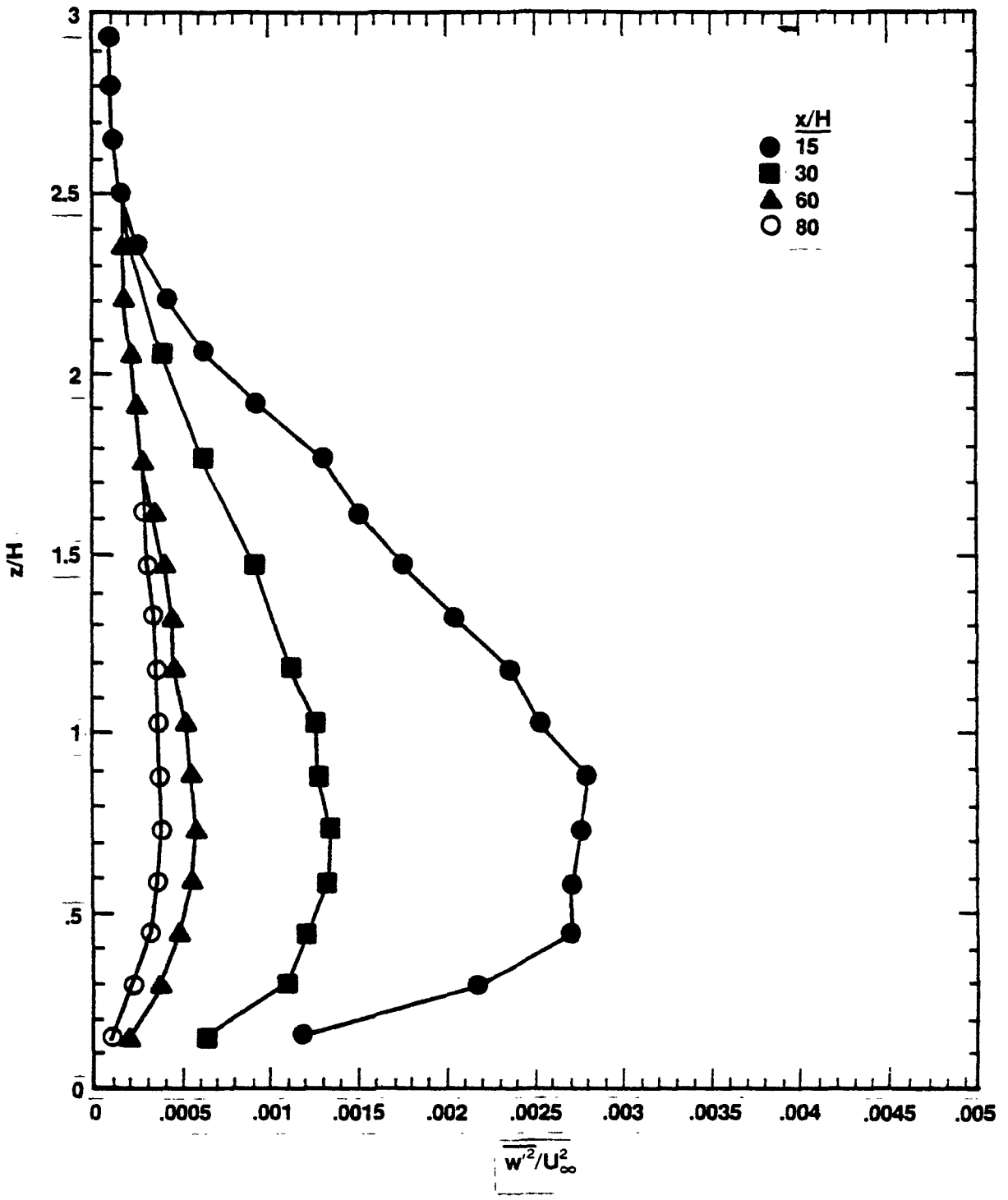

Figure 4.22a. Measured centerline vertical variation of the turbulent kinetic energy component $\overline{w'^2}$ at various downwind distances.

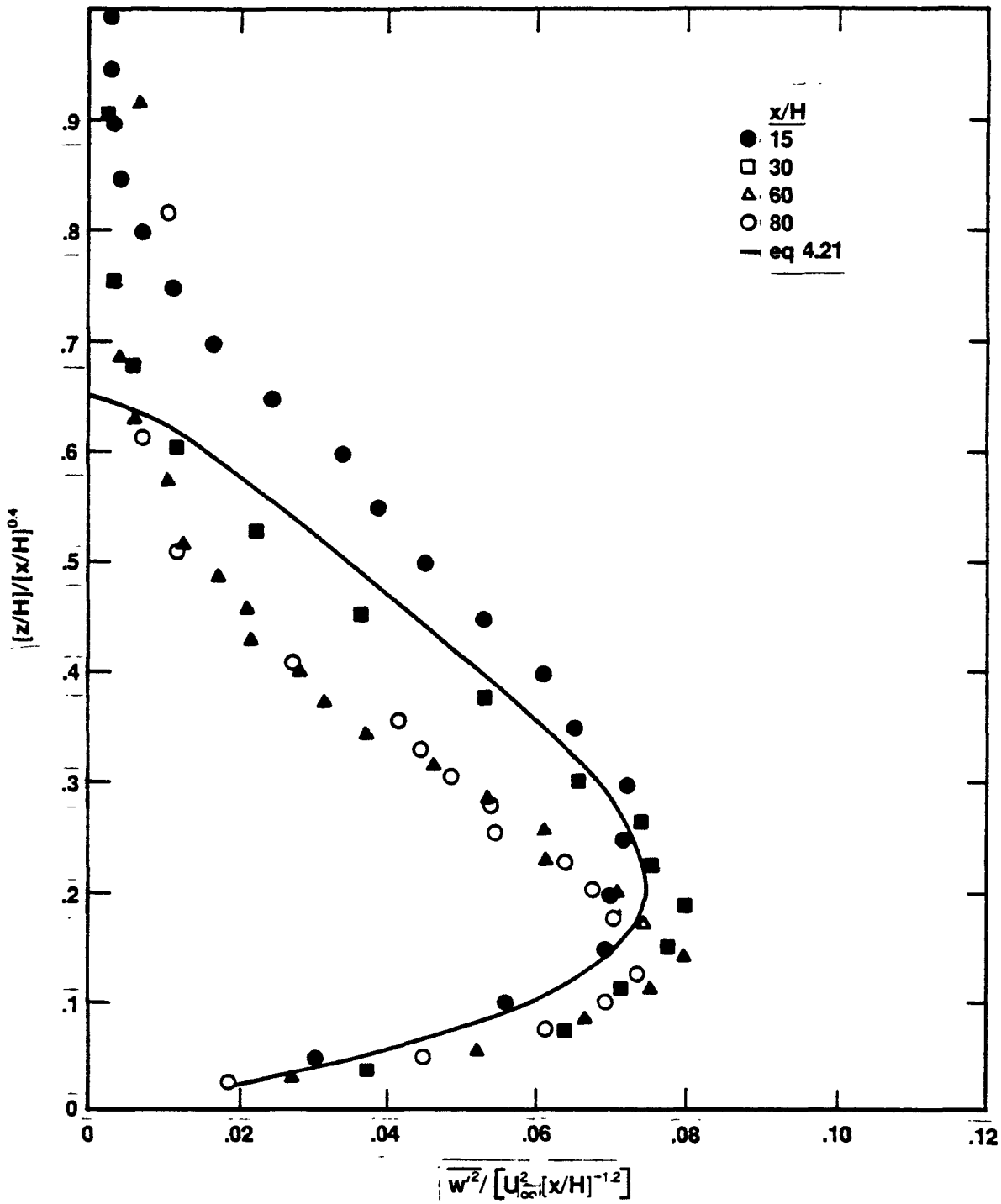

Figure 4.22b. Measured centerline vertical variation of $\overline{w'^2}$ plotted in TKEC similarity variables compared to eq. 4.21 [solid line].

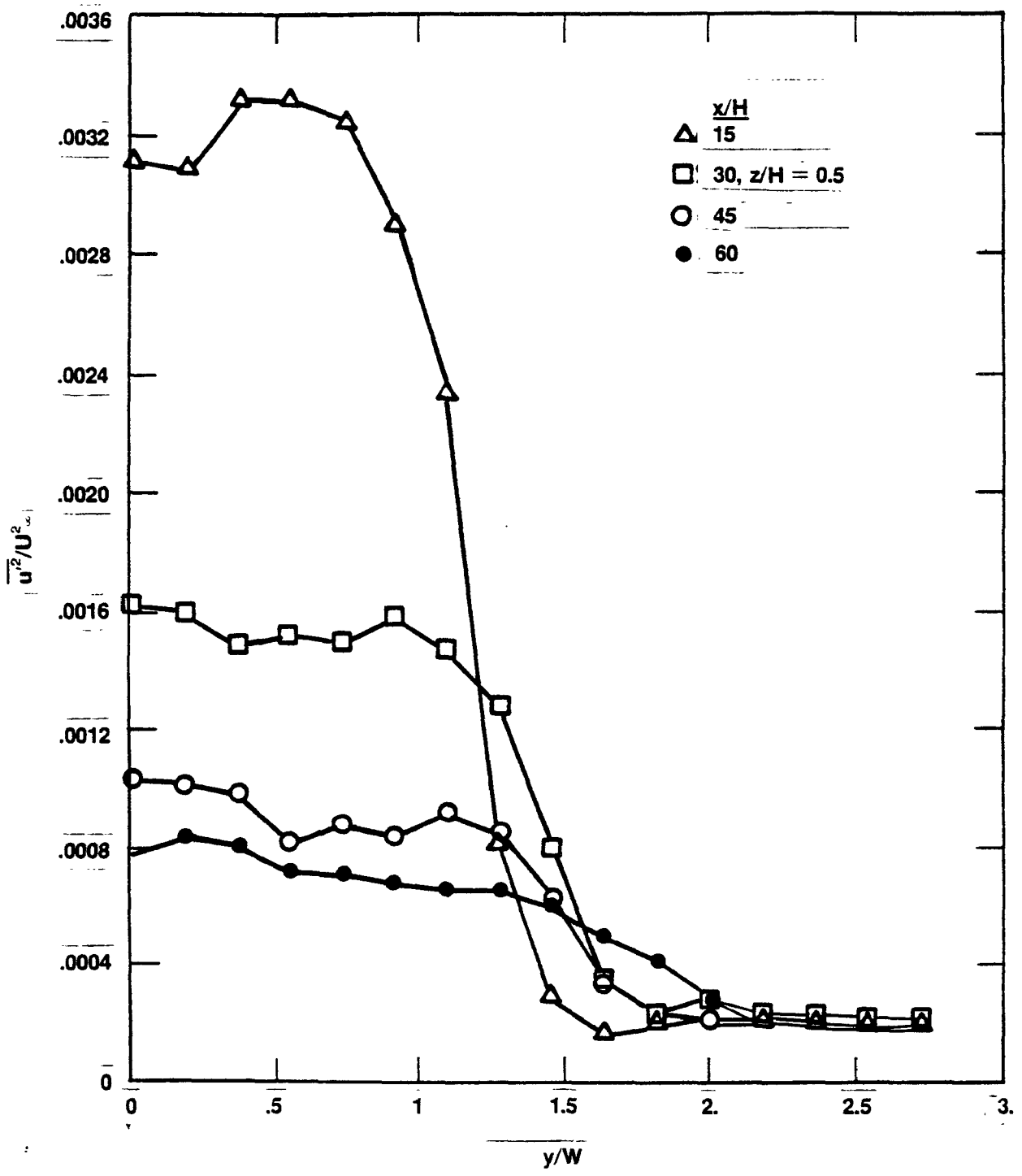

Figure 4.23a. Measured lateral variation of the turbulent kinetic energy component $\overline{u'^2}$ at various downwind distances.

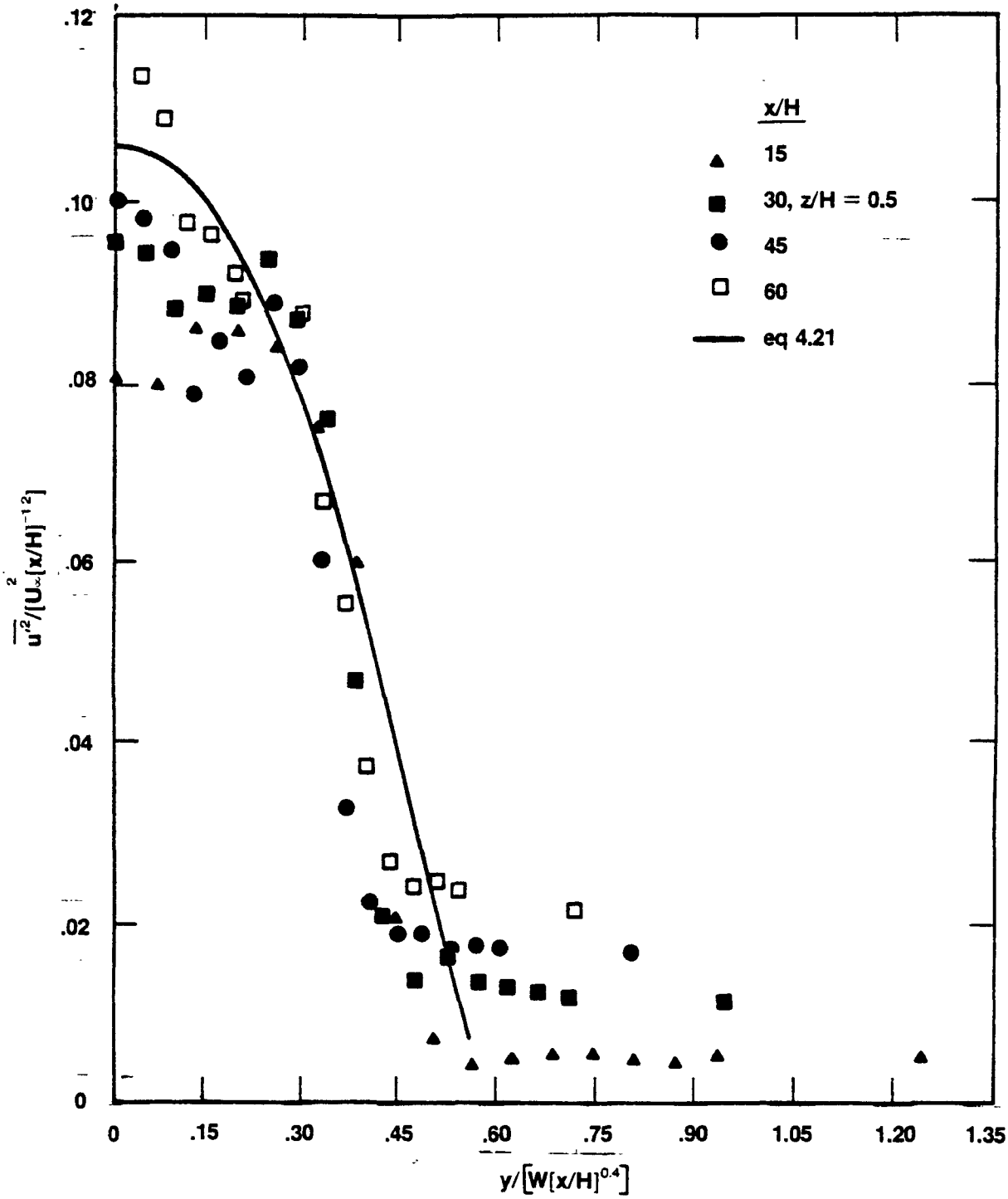

Figure 4.23b. Measured lateral variation of u'^2 plotted in TKEC similarity variables compared to eq. 4.21 [solid line].

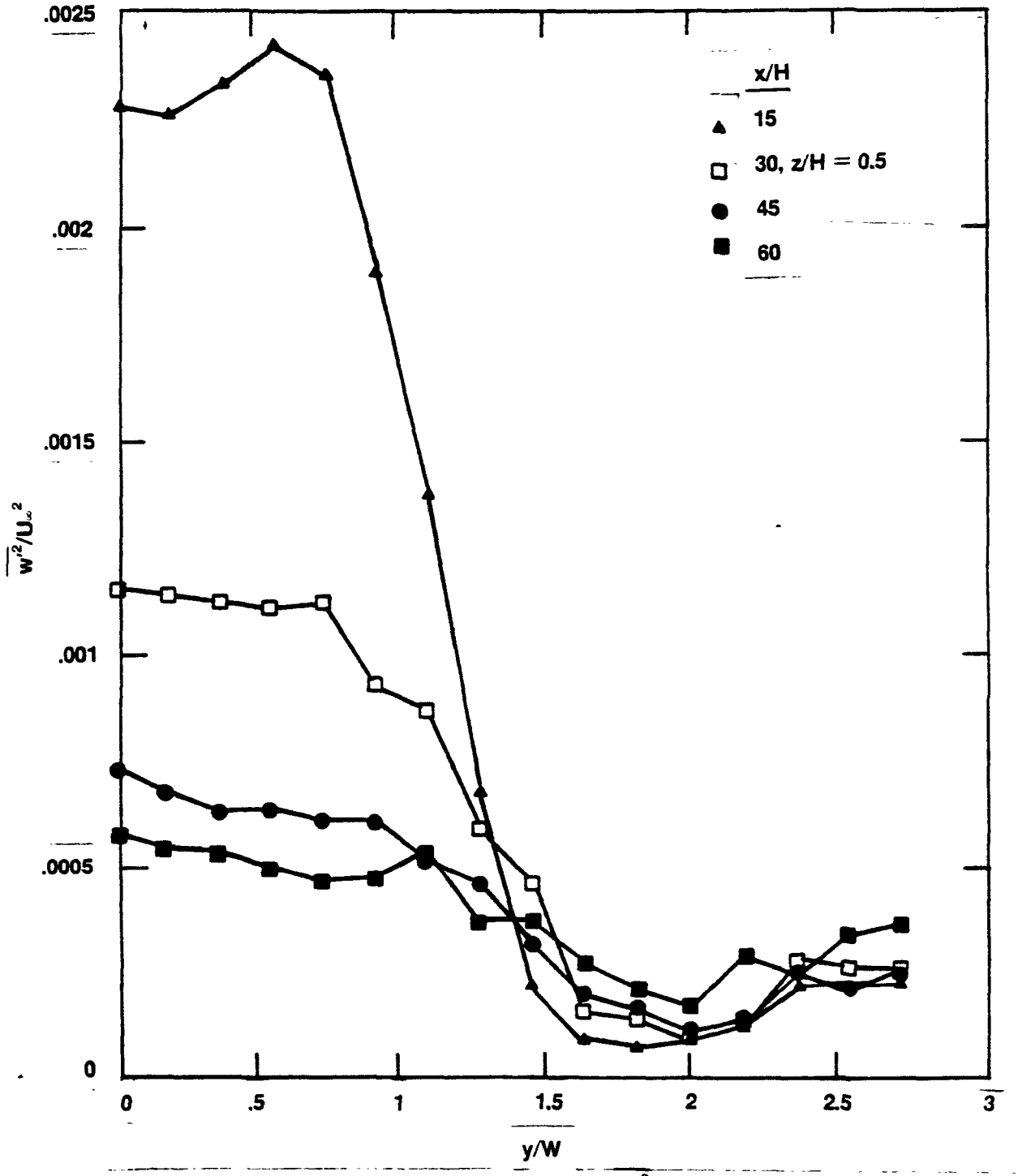

Figure 4.24a. Measured lateral variation of w'^2 at various downwind distances.

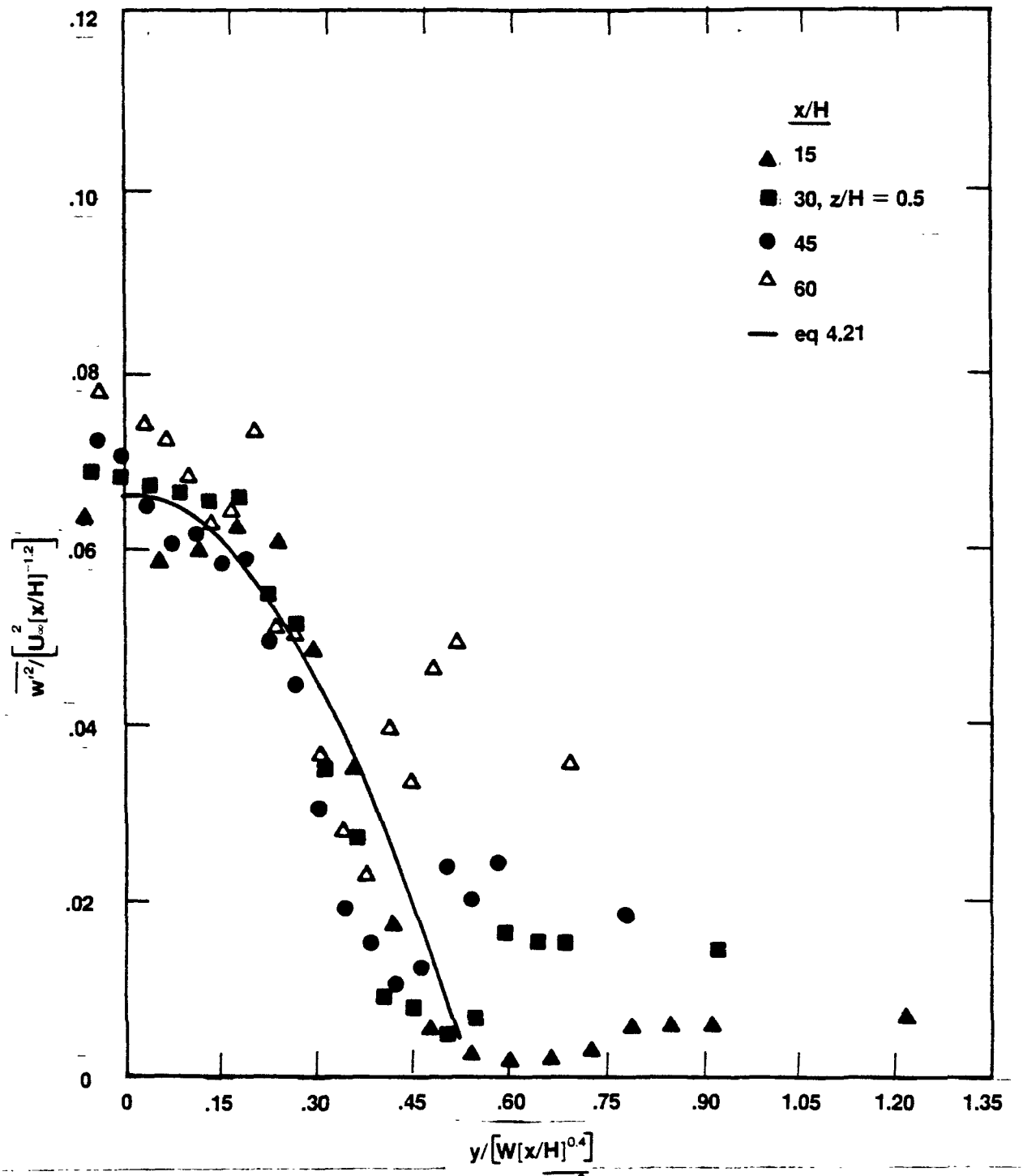

Figure 4.24b. Measured lateral variation of $\overline{w'^2}$ plotted in TKEC similarity variables compared to eq. 4.21 [solid line].

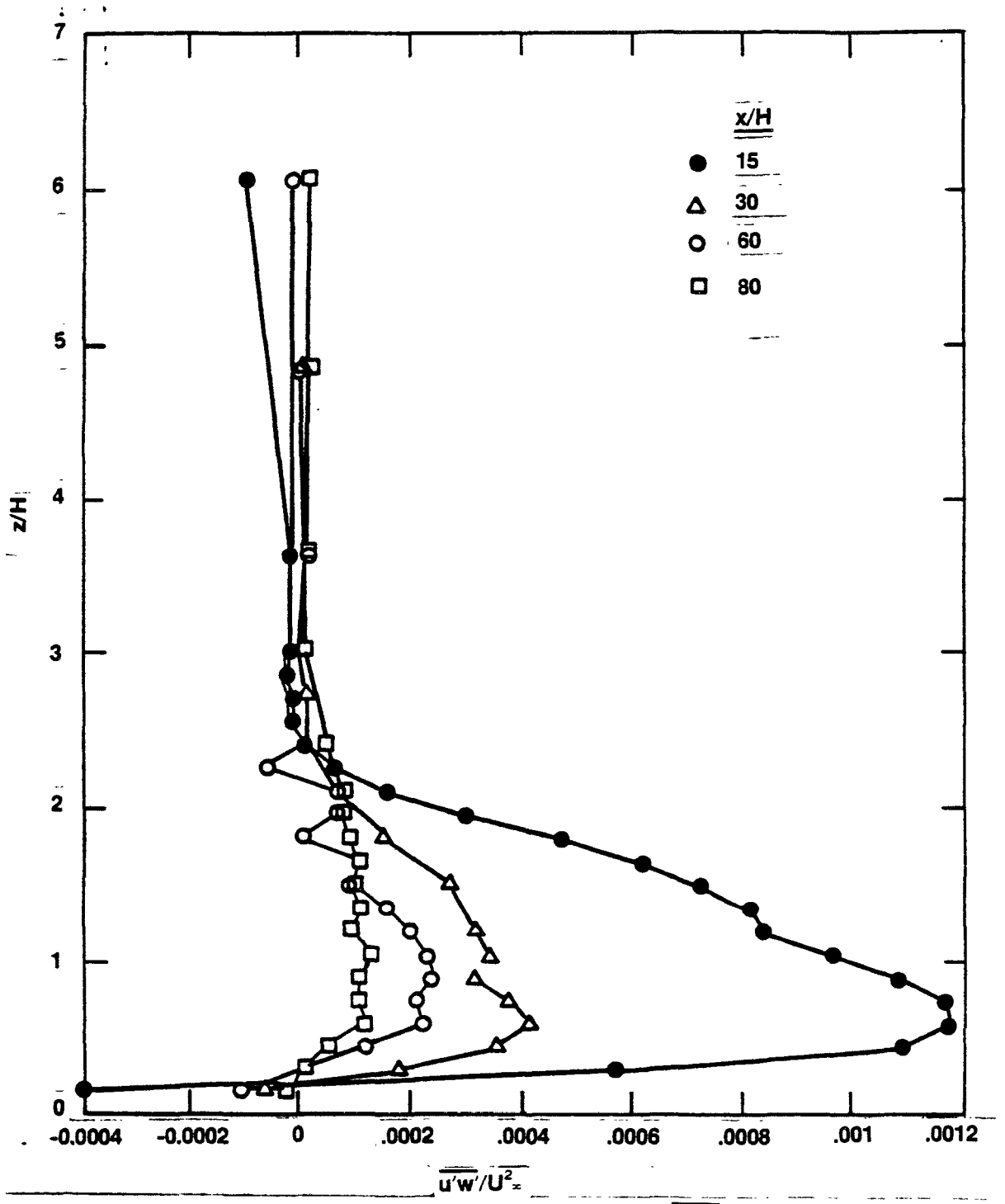

Figure 4.25a. Measured centerline vertical variation of $\overline{u'w'}$ at various downwind distances.

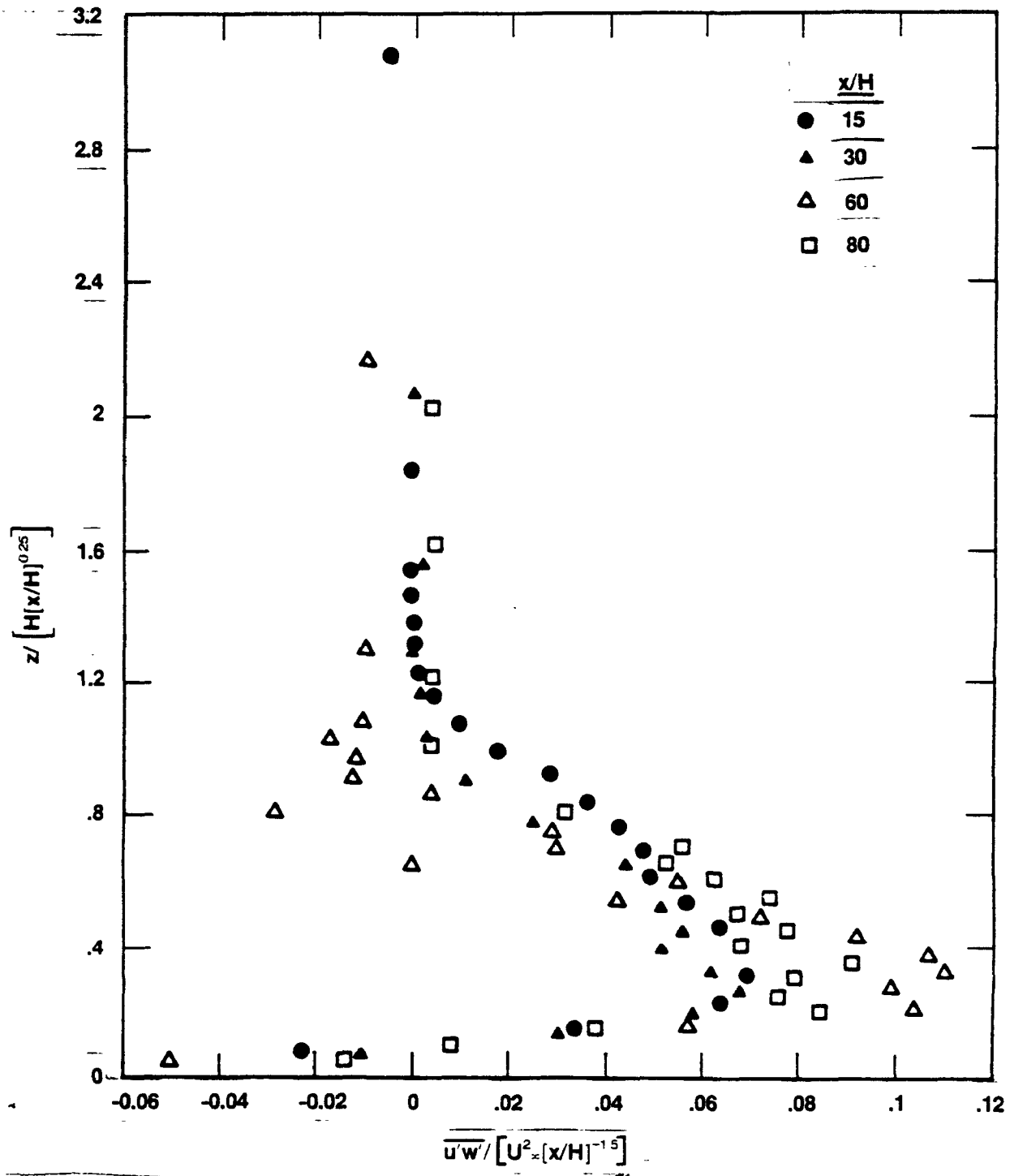

Figure 4.25b. Measured centerline vertical variation of $\overline{u'w'}$ in EH similarity coordinates.

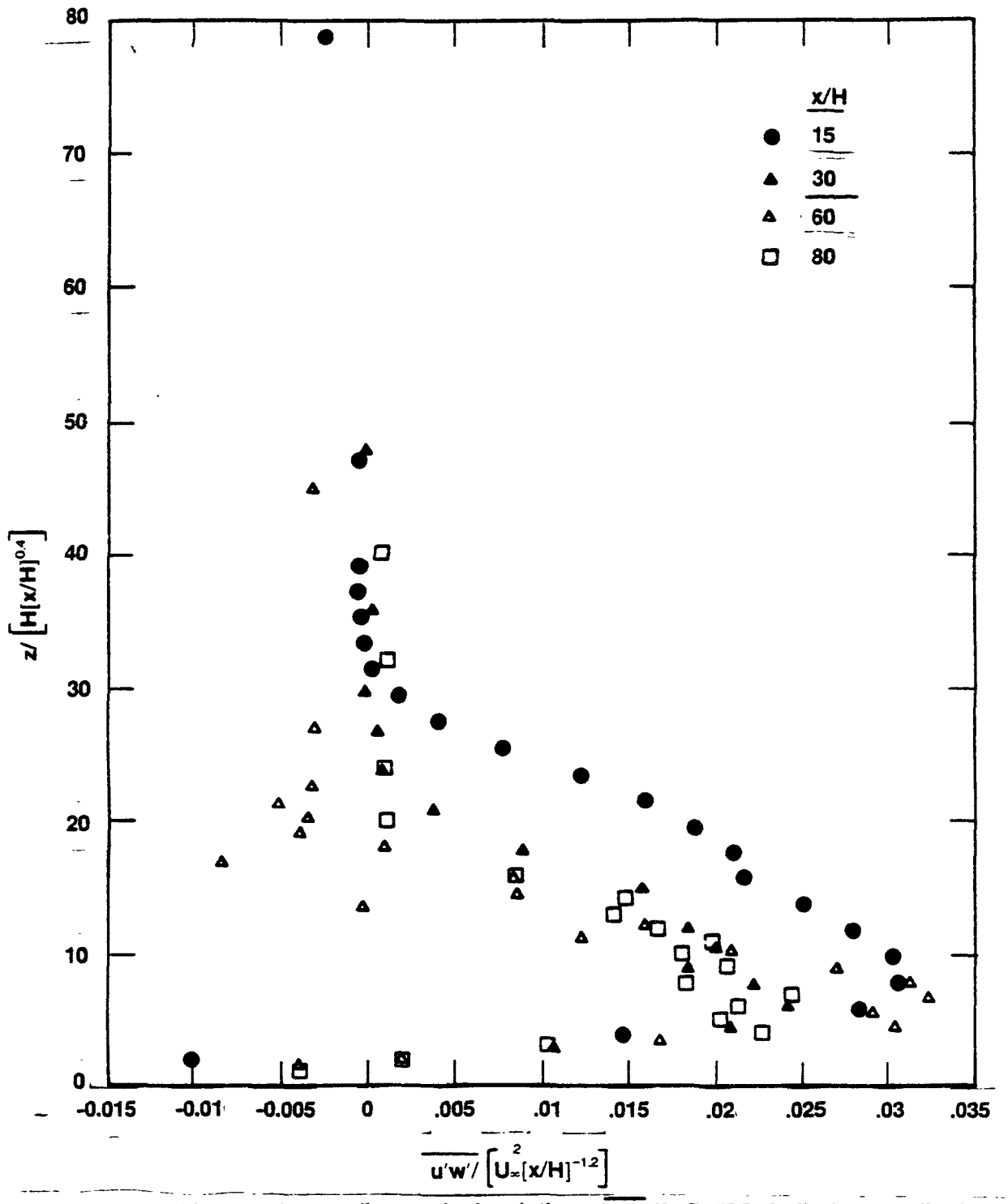

Figure 4.25c. Measured centerline vertical variation of u'w' in TKEC similarity coordinates.

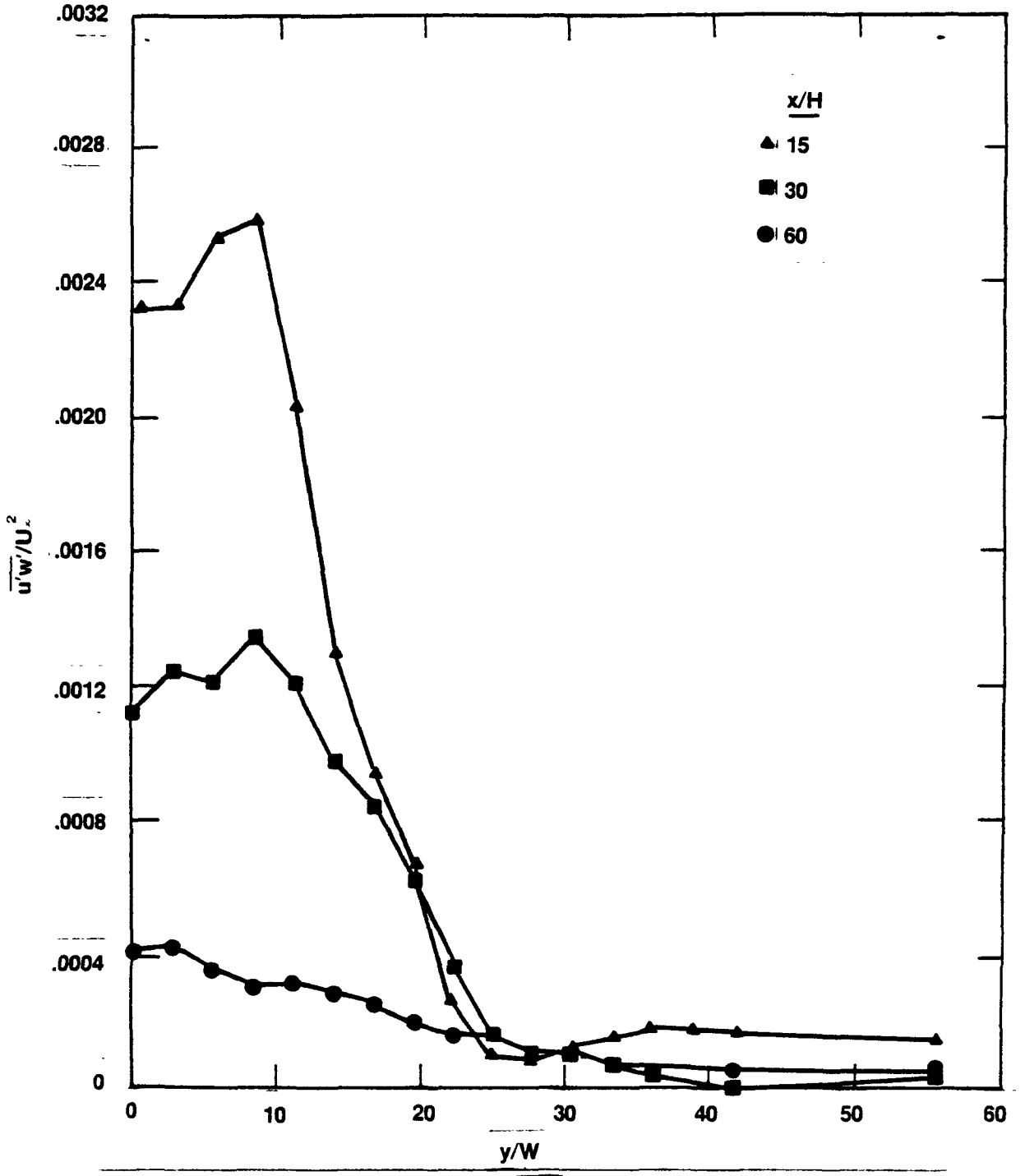

Figure 4.26a. Lateral variation of $\overline{u'w'}$ at various downwind distances.

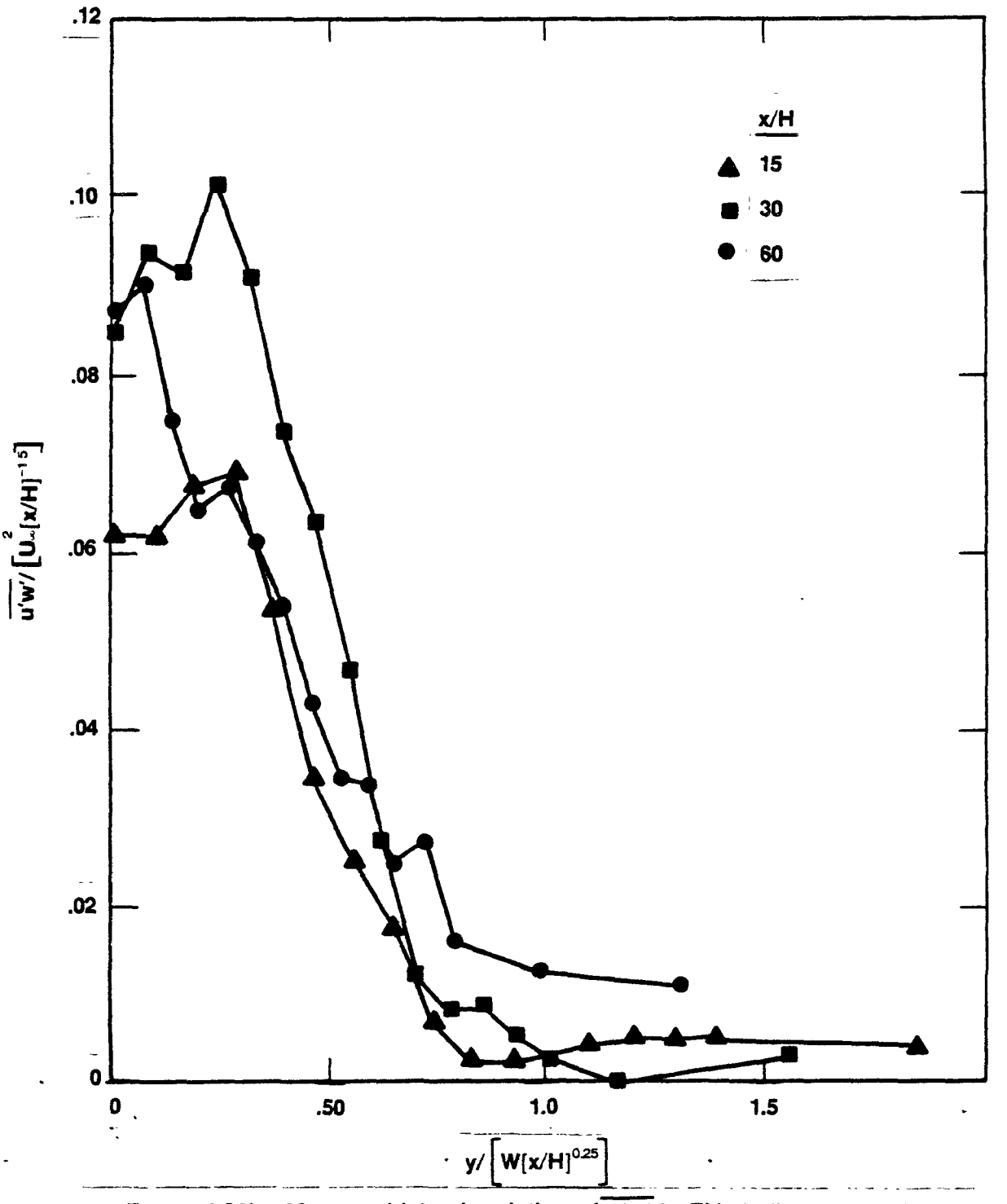

Figure 4.26b. Measured lateral variation of $\overline{u'w'}$ in EH similarity coordinates.

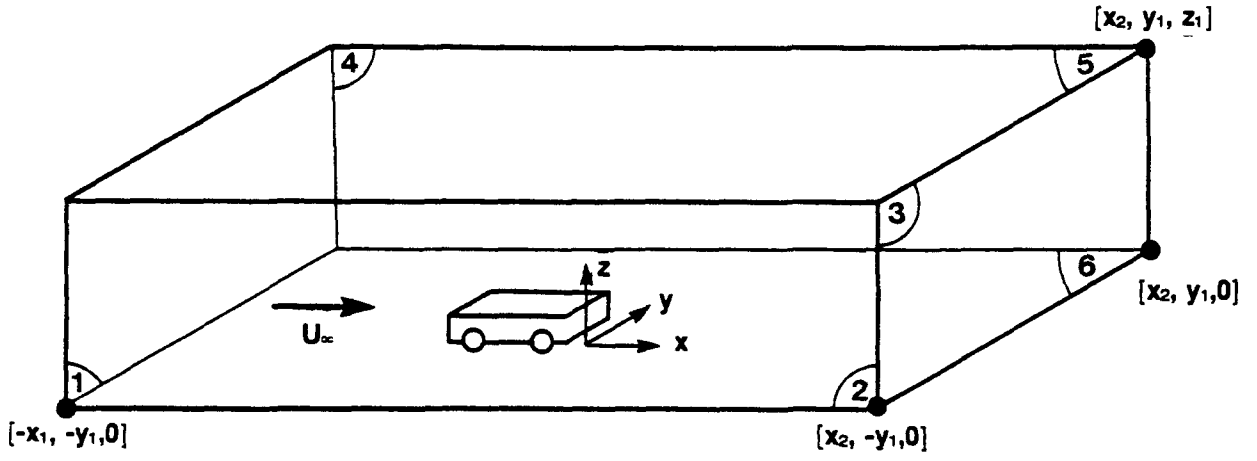

Figure A-1. Control volume for determining the couple.

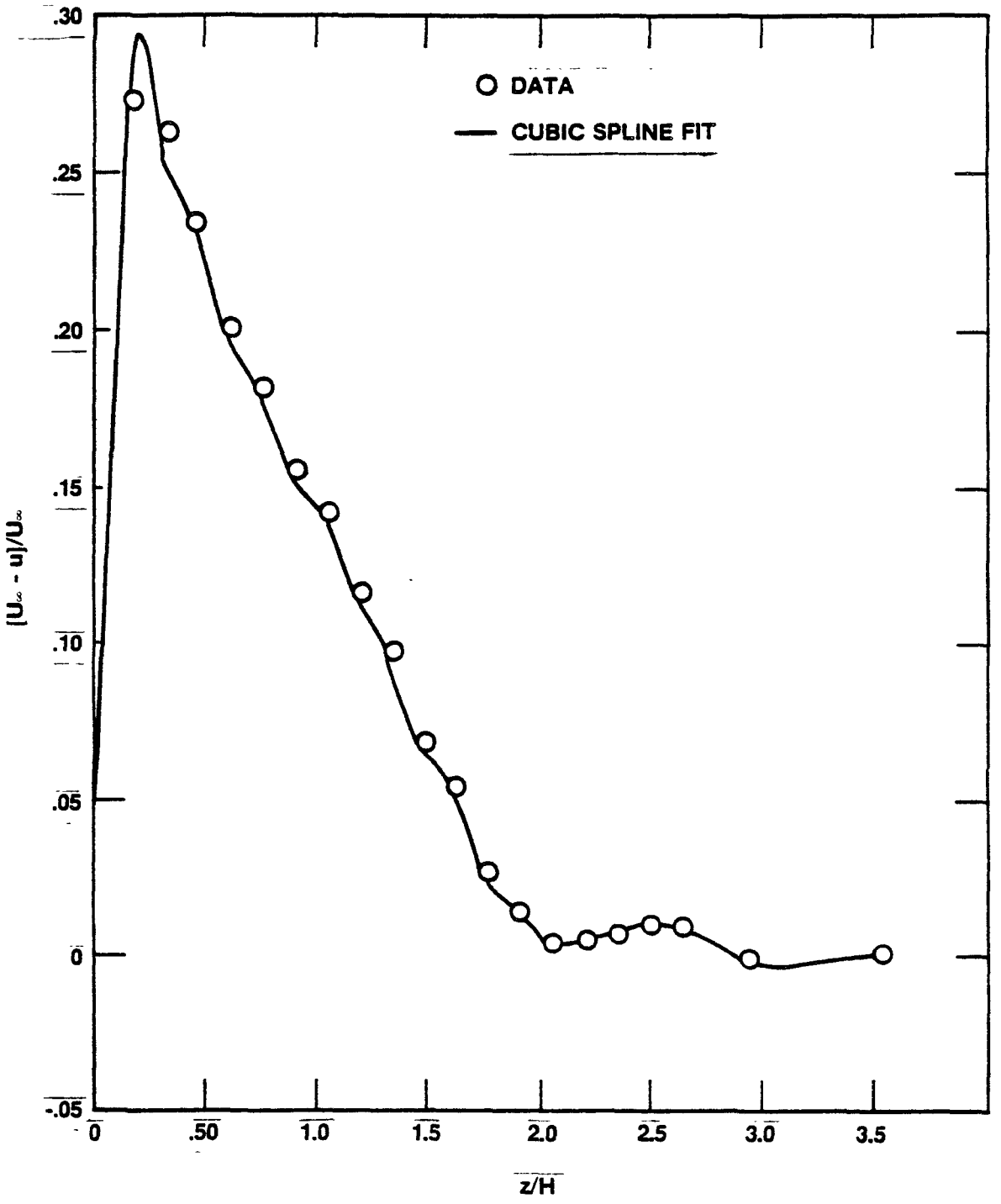

Figure B-1. Example of cubic spline fit to velocity profile at x/H = 10, y = 0.

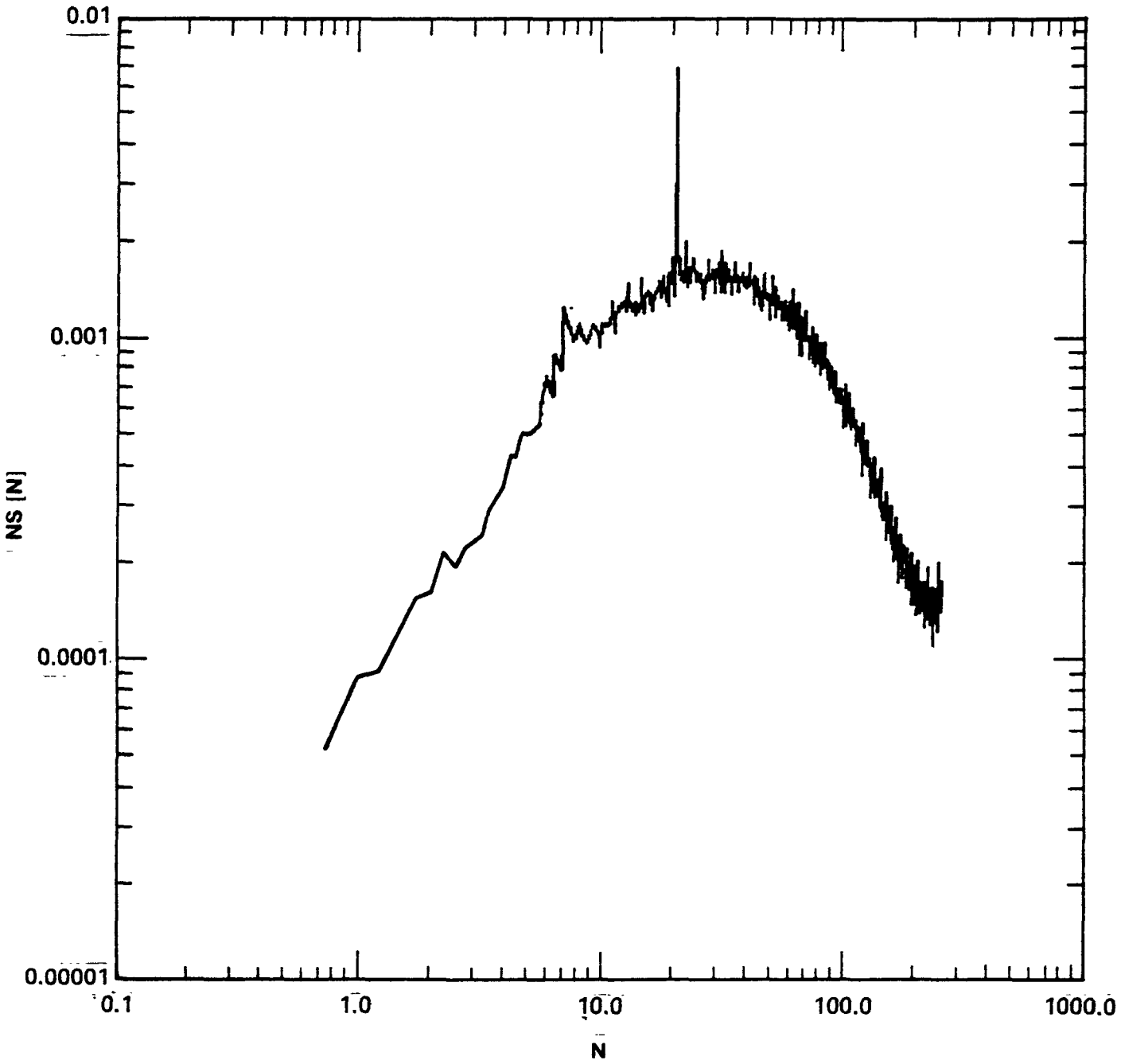

Figure C-1. Example of velocity spectra at x/H = 15. Spike near 20 Hz is due to a vibration from the moving belt.

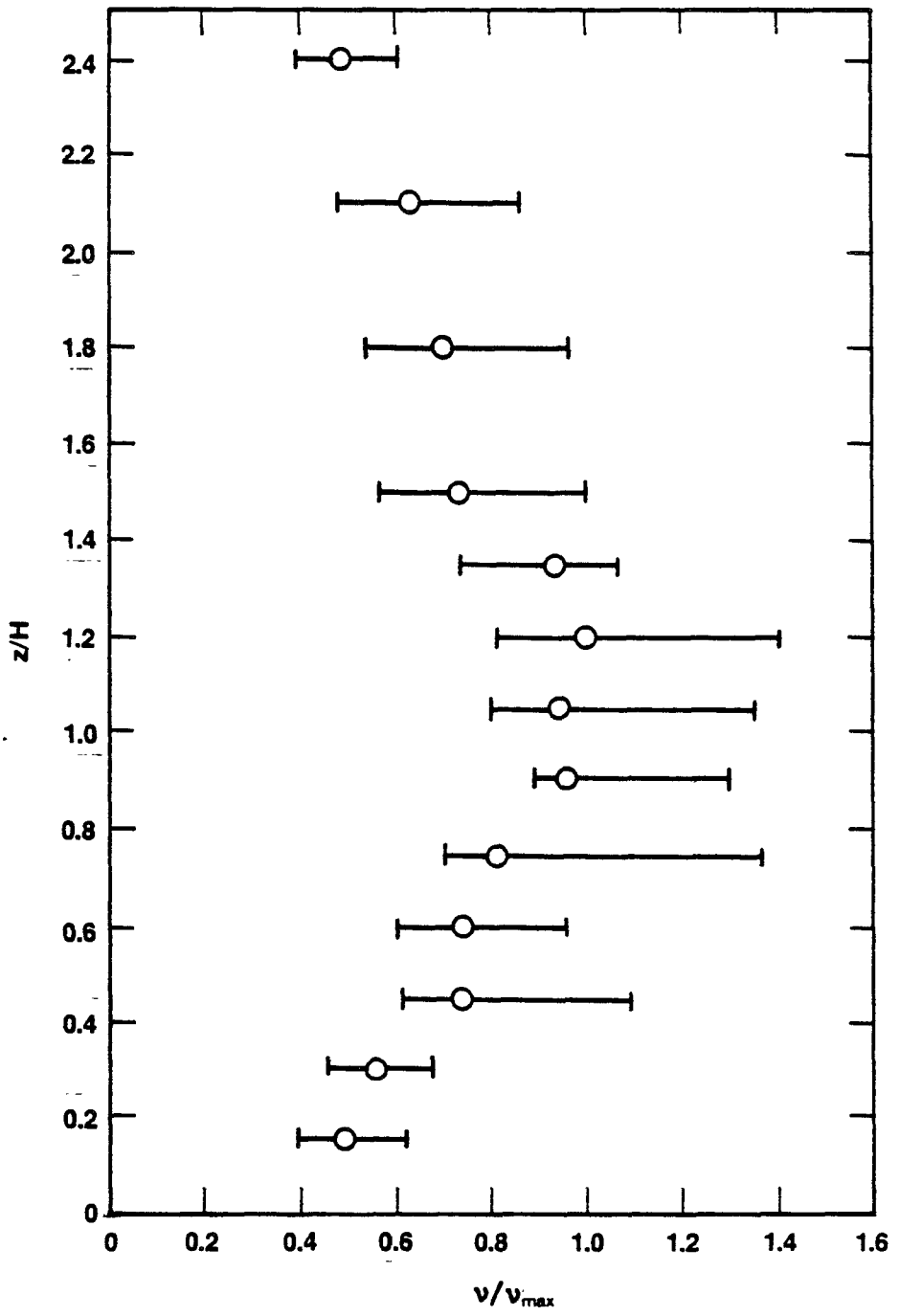

Figure C-2. Vertical variation of the eddy viscosity determined from the spectral data.

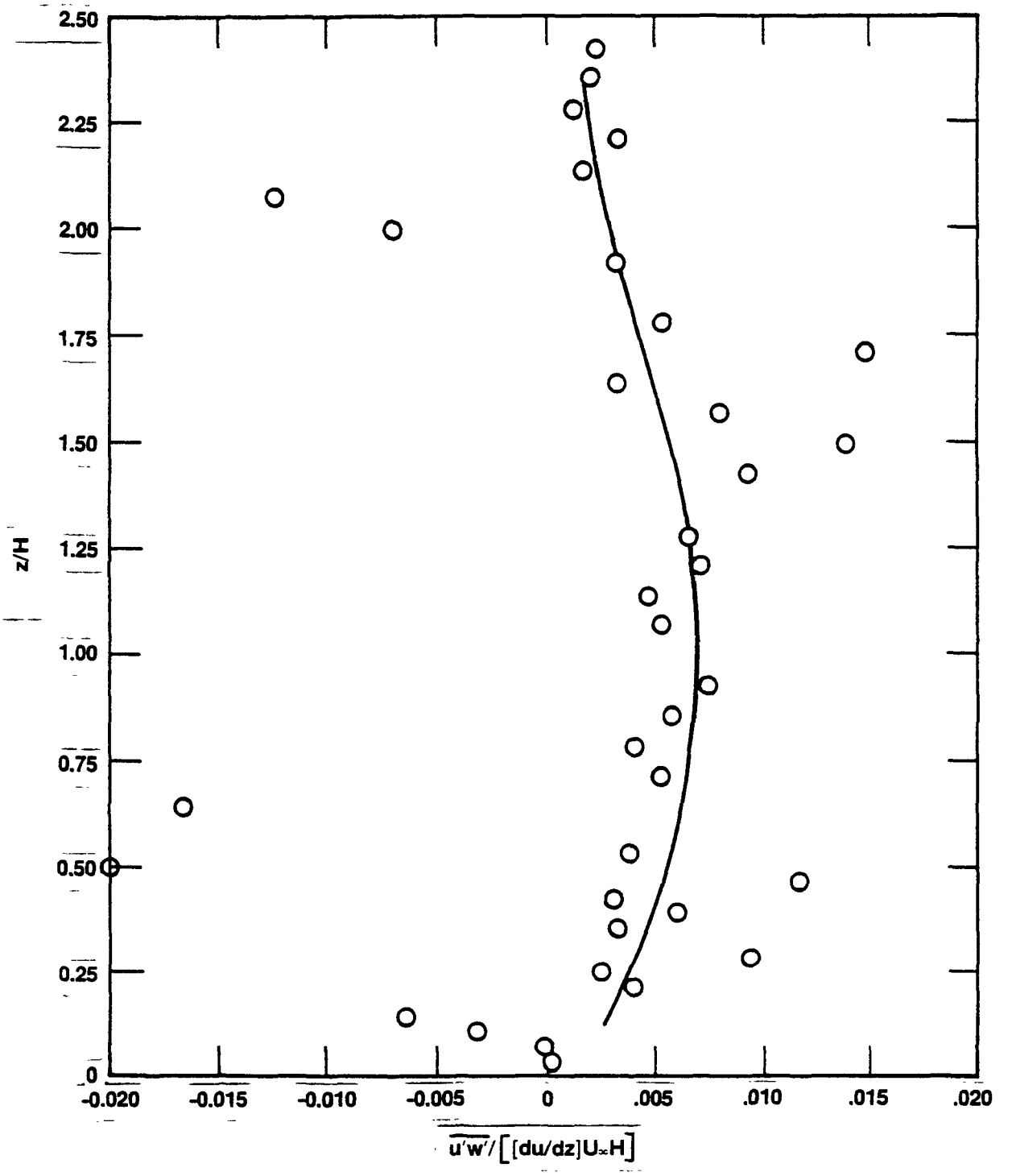

Figure C-3. Vertical variation of the eddy viscosity determined from the Reynolds stress $\overline{u'w'}$.

TECHNICAL REPORT DATA
(Please read Instructions on the reverse before completing)

1. REPORT NO.	2.	3. RECIPIENT'S ACCESSION NO.
4. TITLE AND SUBTITLE WAKE OF A BLOCK VEHICLE IN A SHEAR-FREE BOUNDARY FLOW An Experimental and Theoretical Study		5. REPORT DATE
		6. PERFORMING ORGANIZATION CODE
7. AUTHOR(S) R.E. Eskridge and R.S. Thompson		8. PERFORMING ORGANIZATION REPORT NO. Fluid Modeling Report No. 13
9. PERFORMING ORGANIZATION NAME AND ADDRESS Environmental Sciences Research Laboratory--RTP, NC Office of Research and Development U.S. Environmental Protection Agency Research Triangle Park, NC 27711		10. PROGRAM ELEMENT NO. ADTA1D/02-1313 (FY-82)
		11. CONTRACT/GRANT NO.
12. SPONSORING AGENCY NAME AND ADDRESS Environmental Sciences Research Laboratory--RTP, NC Office of Research and Development U.S. Environmental Protection Agency Research Triangle Park, NC 27711		13. TYPE OF REPORT AND PERIOD COVERED In-house 1/1/79 to 10/1/81
		14. SPONSORING AGENCY CODE EPA/600/03-82-007
15. SUPPLEMENTARY NOTES		

16. ABSTRACT

The wake of a moving vehicle was simulated using a specially-constructed wind tunnel with a moving floor. A "block-shaped" model vehicle was fixed in position over the test-section floor while the floor moved at the freestream air speed to produce a uniform, shear-free, approach flow. This simulates an automobile traveling along a straight highway under calm atmospheric conditions.

Vertical and lateral profiles of mean and fluctuating velocities and Reynolds stresses in the wake of the vehicle were obtained using a hot-film anemometer with an X-probe. Profiles were taken at distances of 10 to 80 model heights downwind.

A momentum type wake was observed behind the block-shaped vehicle. The wake does not have a simple self-preserving form. However, it is possible to collapse the velocity deficit with one length and one velocity scale.

Two new theories for the velocity deficit are compared to the theory of Eskridge and Hunt (1979). A theory which considered a height-dependent eddy viscosity was found to fit the data best.

Length and velocity scales were found for the longitudinal variation of the turbulent kinetic energy. The lateral variation is described by a two-dimensional numerical fit of the crosswind variation of the data.

17. KEY WORDS AND DOCUMENT ANALYSIS

a. DESCRIPTORS	b. IDENTIFIERS/OPEN ENDED TERMS	c. COSATI Field/Group

18. DISTRIBUTION STATEMENT RELEASE TO PUBLIC	19. SECURITY CLASS (This Report) UNCLASSIFIED	21. NO. OF PAGES 116
	20. SECURITY CLASS (This page) UNCLASSIFIED	22. PRICE

EPA Form 2220-1 (9-73)